University of West Bohemia in Pilsen

Faculty of applied science

Department of Mechanics

Diploma thesis

ELECTRO-MECHANICAL COUPLING IN POROUS BONE STRUCTURE - HOMOGENIZATION METHOD APPLICATION

Pilsen, 2013 **Jana Turjanicová**

Statement

I hereby declare that this diploma thesis is completely my own work and that I used only the cited sources.

June 11, 2013 in Pilsen

Jana Turjanicová

Acknowledgements

I would like to thank the head of my thesis Prof. Dr. Ing. Eduard Rohan, DSc. for his guidance during my work on this diploma thesis.

My thanks belong also to Prof. Salah Naili and Dr. Thibauld Lemaire for their patience and guidance during my internship in the Laboratoir modélisation et simulation multi échelle at Université Paris-est.

For the huge help with problem implementation in software *SfePy* I would like to thank Ing. Vladimír Lukeš, Ph.D. and Ing. Robert Cimrman, Ph.D.

Last but not least, thanks belong to my family, my relatives and all my friends, who have helped me during my studies.

Abstract

This diploma thesis focuses on the electro-mechanical coupling in the porous structure of the bone. The cortical bone tissue is modeled as a double-porous medium decomposed into the solid matrix and the fluid saturated canals. In the first part, the study of purely mechanical behavior is performed on the poroelastic model. The method of unfolding homogenization is applied to upscale the microscopic model of the fluid-solid interaction under a static loading. Obtained homogenized coefficients describe material properties of the poroelastic matrix containing fluid-filled pores whose geometry is described at the mesoscopic level. The second-level upscaling provides homogenized poroelastic coefficients relevant to the macroscopic scale. Furthermore, we study the dependence of these coefficients on geometrical parameters which relate to the microscopic and macroscopic scales. In the second part of this thesis, the electro-mechanical coupling in a porous structure with only one level of porosity is discussed, resulting into the model of electro-osmosis in the porous structure. On this model, the unfolding method is applied and the parameter study of dependency of effective coefficients on porosity change is performed. The macroscopic problem is solved on a test body.

Key words: Electro-osmosis, porous medium, poroelasticity, homogenization, unfolding method

This work has been elaborated with the support of project SGS-2013-026 and IGA, NT-13326.

Abstrakt

Diplomová práce se zabývá elektro-mechanickou vazbou v porézní struktuře kosti. Tkáň kortikální kosti je modelována jako medium s dvojí porozitou skládající se z pevné matrice a tekutinou prosycených kanálů. V první části této práce se zabýváme čistě mechanickým chováním modelu poroelasticity. Pro stanovení homogenizovaných koeficientů popisujících mesoskopickou úroveň aplikujeme homogenizační metodu unfoldingu na staticky zatíženou mikroskopickou úroveň. Opětovným aplikováním stejné homogenizační metody na mezoskopickou úroveň popsanou efektivními koeficienty z předešlého kroku je možno získat koeficienty popisující vlastnosti homogenizovaného materiálu na makroskopické úrovni. Dále je provedena parametrická studie závislosti efektivních koeficientů na změně geometrie popisující mikroscopickou strukturu kortikální kosti. Ve druhé části je diskutován vliv elektro-mechanické vazby v porézní struktuře s jedním stupněm porozity. Je zaveden mikroskopický model popisující elektro-osmotické jevy v porézním materiálu. Aplikací metody unfoldingu na tento model lze získat efektivní koeficienty odpovídající homogenizovanému materiálu na makroskopické úrovni. Je provedena parametrická studie vlivu změn v porozitě na hodnoty efektivních koeficientů. V závěru práce je řešena testovací makroskopická úloha.

Klíčová slova: Electro-osmóza, porézní medium, poroelasticita, homogenizace, metoda unfoldingu

Tato práce byla podpořena projektem SGS-2013-026 a z části také projektem IGA, NT-13326.

Contents

1 Introduction

Motivation

In the modern society we daily come in touch with a whole scale of various porous materials. The knowledge about porous structures is widely used in geoscience, industry, material sciences and last but not least in medicine. In recent years, this type of structure is used especially in medicine and biology, because there is no biological material, which is not a porous medium. The same applies for the cortical bone, where the pores filled with bone fluid can be found on multiple scales. The pores can be found on such small scales, that their characteristic size is close to the molecular level and thus not only pressure gradients and concentration gradients, but electrical gradients as well are closely linked to the fluid flow, ion flow and deformations. Thus, all of those phenomena have a part in the determination of material properties of the bone. The knowledge of these properties can serve as a base for the development of new biomaterials, for better understanding of the processes in the bone tissue such as remodeling, or as a material for further research not only in bioscience and medicine but also in other fields of interest.

Related works

This diploma thesis is focused on electro-mechanical coupling in a porous structure. The first model of poroelastic medium was introduced by Biot in a series of papers published between 1935 and 1957. The poroelasticity in a porous medium is the main objective of recent works [25], [26], [27], [20]. The authors of articles [4], [18] and [5] focus on the mathematical method of homogenization. Articles [15], [16], [14] refer to the electro-mechanical coupling in porous structure.

Objective

The aim of this diploma thesis is to learn about a material with a hierarchical porous structure, such as the cortical bone tissue, and introduce an approximative model of its poroelastic behavior. We explain the method of unfolding homogenization on two scale levels resulting into material coefficients relevant to the homogenized material. Further, we discus the electro-mechanical coupling in the porous structure and the phenomena of electro-osmosis. On this basis we introduce the homogenization of electro-osmosis in the structure with one porosity level. We implement both models of homogenization in the *SfePy* software and perform a study of the dependence of material properties on the change of geometric parameters.

Structure of the thesis

This diploma thesis is composed of six sections. The first section is this introduction itself. In the second section named *Biological description*, we introduce the bone functions and structure on various scale levels, from the structure of the whole bone to its microscopic level. The work than

continues with a brief description of a porous material and a bone porosity on different levels in section *Bone porosity*.

The fourth section, *Homogenization of cortical bone poroelasticity*, is one of two more comprehensive sections. On its beginning, we introduce some assumptions, which are necessary for the derivation of the mathematical model introduced further. Then we explain the main principles and tools of homogenization methods and finally derive the homogenized mathematical model of a double-porous medium poroelasticity. Further we describe the mechanical and geometry parameters of the model obtained on the basis of the literature survey. In the end of this section we perform a numerical simulation and a parameter study of elastic parameters porosity dependence.

The section named *Electro diffusion in porous structure of the cortical bone tissue* begins with an explanation of the electro-osmosis phenomena and a discussion about the electro-mechanical coupling in a porous structure. Then we focus on the derivation of the mathematical model of electro-osmosis. Further, we introduce mathematical properties and a geometry describing our model. In the final part of this section we introduce the numerical solution of the macroscopic model and recovery on the local model. In the *Conclusion*, we summarize the results of this thesis and the directions where it is possible to extend this theme.

2 Biological description

This study is focused on a biomechanical problem description. Because of the complexity of our problem, we find it more suitable to describe the biology of the body parts connected to it before presenting the mathematical system.

2.1 Bone

About 206 bones can be found in the human body, but some authors mention even 233 bones. The individual bones are mutually connected by joints and joint capsules, which provide mobility of the whole bone system known as the skeleton. This section is focused on the main functions, types, macroscopic and microscopic structures of the bone tissue.

2.1.1 Function

The bone system has very important functions in the human body, which can be divided into the following three categories.

- Mechanical
  - Protection of internal organs, such as brain, lungs or heart
  - Providing the support of the human body against the gravitation force, thus allowing the upright posture
  - Together with skeletal muscles, tendons, ligaments and joints providing the movement of individual body parts or the whole body in a three dimensional space
- Synthetic
  - Production of blood cells is provided by bone marrow, located in the medullary cavity of long bones and interstices of the trabecular bone.
- Metabolic
  - Storing important minerals such as calcium or phosphor
  - Storing the body fat
  - Removing foreign elements from the blood and storing them in order to detoxicate the organism

2.1.2 Determination of the morphological types of bones

Considering the variety of bone sizes and shapes, we can determine the following morphological types of bones

- Long bones - Femur, Fibula, Tibia, Ulna, ...
- Short bones - Bones of Carpus, bones of Talus, ...
- Flat bones -Scapula, Sternum, ...
- Sesamoid bones - Patella, ...

The long bones are composed of two epiphyses at each end of the bone, and of the diaphysis in the middle. The surface of the long bone body is made of a thick shell of cortical bone, which is getting thiner at the epiphyses. Behind the cortical bone the epiphysis is filled with the trabecular bone which contains the red bone marrow. The interior part of diaphysis is called the medullary cavity and contains yellow or gray bone marrow in the adulthood.

In comparison with the long bones, the short, flat and sesamoid bones cannot be decomposed into the epiphysis and diaphysis. The body of the short bones consists of a cortical bone shell, which is thicker than the long bone shell, and the trabecular bone with higher density of trabeculae.

The cortical bone shell of the flat bones has a characteristically variable thickness. Behind the shell is a low density trabecular bone filled with red bone marrow which produces blood cells even in the old age.

The morphology of bones depends on the genetic predispositions but also changes during life by the mechanical loading.

2.1.3 Inner bone structure

From the terminological point of view, the bone is not a tissue but an organ. The bone tissue is made of bone cells and extracellular matrix and we distinguish its two forms: trabecular (or cancellous) bone and cortical bone.

Trabecular bone is located in the epiphysis of the long bone and in the inner parts of short and flat bones. The structure is made of trabaculae creating a network which usually contains the bone marrow. The density, number and direction of the trabeculae differ highly according to location, genetic predisposition, and loading. It is commonly known that the architecture of the trabeculae changes during life in order to adapt to mechanical loading.

In comparison with the trabecular bone, the cortical bone is lacking trabecular architecture. Higher density provides stronger structure which is necessary for preserving the shape of the bone shell. The microstructure of the cortical bone is explained in more detail in the section below.

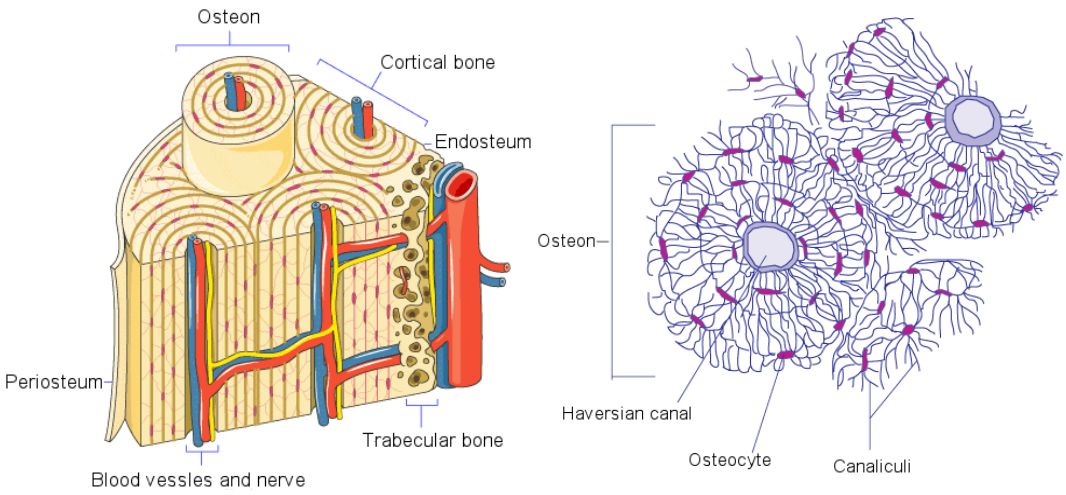

(a) Haversian system

(b) Canalicular-lacunar network

Figure 1: Cortical bone structure , source *http://en.wikipedia.org/wiki/Osteon*

2.1.4 Cortical bone structure

The cortical bone is a strictly hierarchical system with complicated structure on different scale levels. From the macroscopic point of view, the cortical bone tissue is made of a system of approximately cylindrical structures, each with a radius of roughly $100 - 150\mu m$, [32]. These structures are known as osteons and are hollow; in the center of each osteon is the so-called Haversian canal, which contains blood vessels or nerves and some space is occupied by bone fluid. The walls of the Haversian canal are covered with bone cells and behind this bone cell layer, there are entrances to multiple small tunnels [32]. These tunnels are called canaliculi and they connect the Haversian canal to lacunae and lacunae to other lacunae.

The lacunae are approximately of ellipsoidal shape and each of them contains one bone-creating cell, osteocyte. Canaliculi and lacunae create one system of mutually connected network filled with bone fluid.

2.2 Bone fluid

The small cavities in the bone structure are not void. Instead they are filled with the so-called bone fluid. By this name we label two types of fluid. The first is so-called serum, which is the fluid in the space outside the blood vessels filling osteonal canals. The second type is extracellular fluid filling the space in lacunae and canaliculi, [6]. We refer to both of these fluids as a bone fluid here.

The bone fluid has some important roles in the bone structure. The fluid in the lacunar-canalicular system is the coupling medium through which the mechanical forces are translated into mechanobiological, biochemical, mechanochemical and electromechanical phenomena at the cellular level.

3 Bone porosity

From the biological description in the section above is clear, that there is a high number of cavities, pores and canals on various scales of the bone structure. This gives us an option to think about the bone tissue as a porous material.

3.1 Porous material

In general, a porous material is a heterogeneous material whose heterogeneity is caused by the existence of cavities or pores in its solid phase matrix. The main parameter of a porous material is called porosity, with its value in interval $< 0, 1 >$ and is defined as volume fraction of pores in volume V of the whole body of porous material in the space,

$$\frac{V_{pore}}{V} = \phi. \tag{1}$$

The space of pores is usually not empty, instead it is fully or partially saturated by a fluid (gas or liquid). In this fluid phase, the numerous mechanical or electro-chemical processes, such as fluid flow or diffusion, can take effect. This is the reason why we cannot see the porous material as homogeneous or even continuous material. Instead, in order to effectively work with the porous medium, homogenization procedures are widely used.

3.2 Cortical bone tissue as a material with two levels of porosity

In the previous chapter, we introduced the porous material and the reason why we can use this type of material for the modeling of a cortical bone tissue. In most cases, the porous materials have just one level of porosity, but there are some materials with more porosity levels.

If we look closer on the structure of the cortical bone tissue, we can see the different types of porosity. There are pores which are visible just by a naked eye but for other pores we have to look through a microscope. We say that the porosity is on different scale levels, see Fig.2.

In literature, [1], [21], [32], there can be found three porosity levels which are the most important in the bone structure:

- **Vascular porosity** - the space in the Haversian canal is included
- **Lacunar-canalicular porosity** - all the space in the lacunae and canaliculi is included
- **Collagen-apatite porosity** - porosity associated with the space between collagen and the crystallites of the mineral apatite

In this thesis, we want to study the material properties of a single bone osteon. Thus, we neglect the vascular porosity (or osteonal porosity), because the diameter of the Haversian canal is

too large to consider it as a pore. We neglect the collagen-apatite porosity but we focus only on the lacunar-canalicular porosity considering the bone matrix to be homogeneous on the lower level.

Unlike in other studies, [1], [21], we split the lacunar-canalicular porosity into two levels:

- Microscopic level - the porosity caused by canaliculi only
- Mesoscopic level - the porosity caused by lacunae only

Further in the text, the microscopic level will be denoted as $\alpha-$level and mesoscopic as $\beta-$*level*. The porosities are denoted by ϕ_α and ϕ_β with the subscript corresponding to the level.

For the material with two porosity scales, the resulting porosity ϕ_γ is influenced by both level porosities ϕ_α and ϕ_β as follows

$$\phi_\gamma = \phi_\alpha + \phi_\beta - \phi_\alpha\phi_\beta. \tag{2}$$

We work with these three porosities later. Finally, we introduce the macroscopic level, which represents the level of a single bone osteon and whose properties are in the center of our attention.

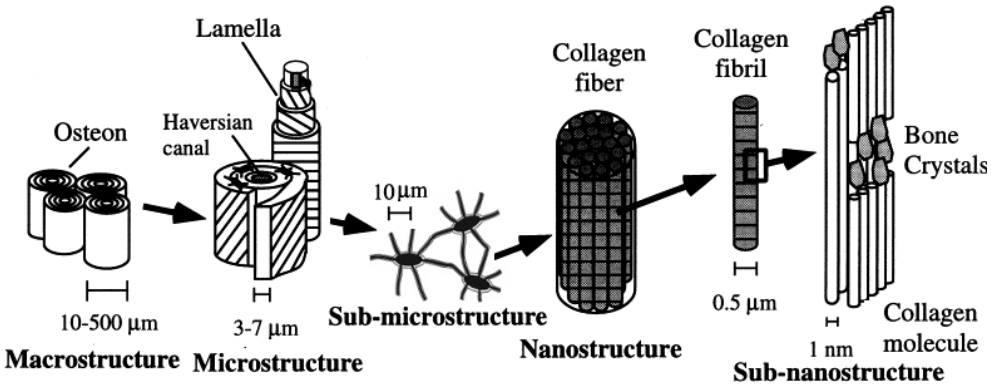

Figure 2: Different scale levels of the cortical bone structure

4 Homogenization of cortical bone poroelasticity

4.1 Assumptions

First of all, before even talking about homogenization method we have to state a set of assumptions which will be used for simplifying the problem and derivation of the mathematical model.

4.1.1 Periodic material

Biological materials, such as a cortical bone tissue, are known to be highly heterogeneous with aperiodical structure and can not be precisely described. Although, we assume that there is some periodically repeated substructure, by which the whole material can be described. For better imagination see Fig.3. Note, that this assumption is very simplifying, but it is necessary for further modeling.

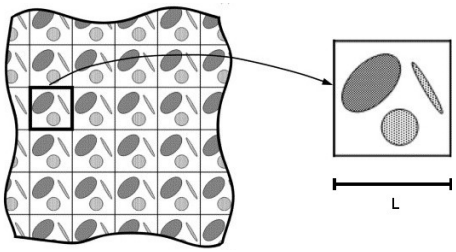

Figure 3: Illustration of a periodic structure, source: *http://www.sciencedirect.com/science/article/pii/S0266353806000844*

We assume that on the microstructure, the cortical bone tissue consists of cubic cells, each with the same structure and length of side L. The parameter L will be called the characteristic dimension (or length) further in the text.

4.1.2 Matrix as a linear elastic material

As was mentioned in the section above, the biomaterials are known for their non-linear behavior. Thus, when modeling such a material, the non-linear (mainly viscoelastic) models with the assumption of large deformations are widely used. Although, in our study, we assume only small deformations of the cortical bone matrix and thus we can describe this material by a constitutive relation of linear elasticity.

Considering the assumption above, the strain in the matrix is described by the Cauchy's strain tensor

$$e_{ij} = \frac{1}{2}\left(\frac{\partial u_i}{\partial x_j} + \frac{\partial u_j}{\partial x_i}\right), \tag{3}$$

where $\mathbf{u}(\mathbf{x})$ is a displacement. Further we assume the stress to be a linear function of the strain, in other words the Hook's law in the form

$$\sigma_{ij} = D_{ijkl} e_{ij}, \tag{4}$$

where σ_{ij} are components of the stress tensor $\boldsymbol{\sigma}$ and D_{ijkl} are components of the fourth-order stiff-

ness tensor defined by

$$D_{ijkl} = \mu(\delta_{ik}\delta_{jl} + \delta_{il}\delta_{jk}) + \lambda\delta_{ij}\delta_{kl}. \tag{5}$$

In the previous formula, the symbols μ, λ stand for Lamme's coefficients and δ_{ij} is the Kronecker's symbol. The stiffness tensor $\mathbb{D}$ can also be described by the Young's modulus E and the Poisson's ratio ν, when the relations between the couple E, ν and the Lamme's coefficients μ, λ are as follows

$$\lambda = \frac{E\nu}{(1+\nu)(1-2\nu)}, \quad \mu = \frac{E}{2(1+\nu)}. \tag{6}$$

Note that the stiffness tensor $\mathbb{D}$ has the following symmetry

$$D_{ijkl} = D_{jikl} = D_{klij}. \tag{7}$$

The inverse tensor to the stiffness tensor is called the compliance tensor $\mathbb{C}$

$$\mathbb{C} = \mathbb{D}^{-1}. \tag{8}$$

4.1.3 Assumption of the cortical bone tissue as an orthotropic material

We have already stated, that the cortical bone tissue is a heterogeneous anisothropic material. However, for simplicity, we can assume the material to be orthotropic. Let us bring back to mind that orthothropic materials have three orthogonal planes of symmetry. Thus, it can be shown that a void notation of the stiffness tensor is

$$\mathbb{D} = \begin{bmatrix} D_{11} & D_{12} & D_{13} & 0 & 0 & 0 \\ D_{12} & D_{22} & D_{23} & 0 & 0 & 0 \\ D_{13} & D_{23} & D_{33} & 0 & 0 & 0 \\ 0 & 0 & 0 & D_{44} & 0 & 0 \\ 0 & 0 & 0 & 0 & D_{55} & 0 \\ 0 & 0 & 0 & 0 & 0 & D_{66} \end{bmatrix} \tag{9}$$

and the void notation of the $\mathbb{C}$

$$\mathbb{C} = \begin{bmatrix} \frac{1}{E_1} & -\frac{\nu_{21}}{E_2} & -\frac{\nu_{31}}{E_3} & 0 & 0 & 0 \\ -\frac{\nu_{12}}{E_1} & \frac{1}{E_2} & -\frac{\nu_{32}}{E_3} & 0 & 0 & 0 \\ -\frac{\nu_{13}}{E_1} & -\frac{\nu_{23}}{E_2} & \frac{1}{E_3} & 0 & 0 & 0 \\ 0 & 0 & 0 & \frac{1}{G_{12}} & 0 & 0 \\ 0 & 0 & 0 & 0 & \frac{1}{G_{23}} & 0 \\ 0 & 0 & 0 & 0 & 0 & \frac{1}{G_{31}} \end{bmatrix} \tag{10}$$

, where E_1, E_2, E_3 are Young's moduli in directions 1, 2, 3. ν_{ij} represents the Poisson's ratio for the strain in direction j while loaded in direction i. G_{12}, G_{23}, G_{31} are shear moduli in 1-2, 2-3 a 3-1.

The void notation of both $\mathbb{C}$ and $\mathbb{D}$ tensors is symmetric, thus from $\mathbb{C}$ can be seen that

$$\frac{\nu_{ij}}{E_i} = \frac{\nu_{ji}}{E_j}. \tag{11}$$

Thus, the orthotropic material can be described by 12 material constants, which are E_1, E_2, E_3, $\nu_{ij}, G_{12}, G_{23}, G_{31}$.

4.1.4 Bone fluid as a Newtonian compressible fluid

In [25], the bone fluid is considered as a compressible Newtonian fluid. In this section, we explain what is the main difference between compressible and incompressible fluids.

The compressible fluid is the one in which the fluid density changes when subjected to high-pressure. The change of density in gases is additionally complicated by changes in temperature, [13], but in our case those are not considered. This is different from the incompressible fluid, but the main difference is in the way the forces are transmitted through the fluid.

The force applied to the incompressible fluid leads to its immediate flow. On the contrary, the same force applied to the compressible fluid does not cause the flow immediately. First, it leads to compression of the fluid near the place where the force was applied and this effect is gradually spread onto the whole fluid medium. When the fluid cannot be compressed anymore, the pressure finally causes it to flow.

The characteristic of the compressible fluid is called compressibility γ and it is defined as a measure of the relative volume change in response to the change of pressure,

$$\gamma = -\frac{1}{V}\frac{dV}{dp}. \tag{12}$$

In our study, the fluid serves mainly as a medium for the pressure transfer, thus we don't have to define any equations describing the fluid flow.

4.1.5 Assumptions summary

Considering the previous assumptions, we model the cortical bone tissue as a deformable porous medium saturated by a fluid. The matrix is considered as an orthotropic linear elastic material with a periodic structure. Such materials are often called linearly poroelastic. The fluid is approximated as a compressible Newtonian.

Further we assume the steady state only with time independent loading induced for example by a deformation of other part of the tissue. Thus we can imagine that as a simple case of loading the bone while carrying some weight.

4.2 General principles of homogenization method

In this section, we present a mathematical model for cortical bone tissue poroelasticity by applying the method of homogenization. Note that all assumptions from the previous section will be considered. First we introduce some general principles, which come to use further in the creation of the mathematical model.

4.2.1 Definition of geometrical configuration of the problem

Let us consider a poroelastic body, which is represented by the domain Ω in $N-$dimensional space. We consider the domain $\Omega \in \mathbb{R}^N$ open bounded with boundary $\partial\Omega$, [20], [25], [26]. The domain Ω is described by the coordinate system $0, x_1, x_2, ..., x_N$, where N is the dimension of the problem.

In the domain Ω, two conjunctive subdomains are distinguishable; The domain Ω_m^ε represents the space occupied by the solid matrix and the domain Ω_c^ε represents the canals. The interface between those two subdomains will be referred to as Γ_{mc}^ε.

In what follows, we use two subscripts that refer to different material components of the bone tissue: matrix (m) and canal (c). Th superscript ε refers to the scale and is explained in the following section.

4.2.2 Scale parameter ε

We consider a body with characteristic dimension L_{macro}. The material of the body can be described by a periodically repeated structure with characteristic dimension L_{micro}. Let us define small dimensionless parameter $\varepsilon, 0 < \varepsilon(l)1$ as a ratio

$$\varepsilon = \frac{L_{micro}}{L_{macro}}. \tag{13}$$

The parameter ε is called the scale parameter and represents the smallest zoom, by which the microstructure becomes visible from the macroscopic point of view.

4.2.3 Types of porosity

Let us consider a poroelastic body with pores saturated by a fluid, which is in our case the compressible Newtonian. We consider the steady state of this body, neglecting all inertial forces, even the effect of gravitation acceleration. We apply the static loading on the body; This causes the rise of pressure p in the fluid, which has effect also on the interior of the matrix. In this place it is necessary to distinguish two types of porosity, which affect the pressure distribution in the fluid. Note that in both cases the continual open bounded matrix subdomain $\Omega_m^\varepsilon \subset \Omega$ is considered.

- The pores, or in our case canals, are mutually connected creating one network, so that the subdomain of canals, $\Omega_m^\varepsilon \subset \Omega$, is a continual open bounded domain, such that

$$\Omega = \Omega_m^\varepsilon \cup \Omega_c^\varepsilon \cup \Gamma_{mc}^\varepsilon, \quad \Omega_c^\varepsilon = \Omega^\varepsilon \setminus \bar{\Omega}_m^\varepsilon, \quad \Gamma_{mc}^\varepsilon = \bar{\Omega}_m^\varepsilon \cap \bar{\Omega}_c^\varepsilon, \tag{14}$$

  where by $\bar{}$ we denote the set closure. In this case, the pressure p in the fluid is evenly distributed and is characterized only by one scalar value, [20], [25], [26].

- The second case is, when there are some pores which are separated from the connected ones. The fluid is trapped in these pores and thus the pressure cannot be distributed in all fluid parts evenly like in the previous case. Instead, the pressure can have a different value in each point $\mathbf{x}$ and so it is characterized by a scalar field $p(\mathbf{x})$.

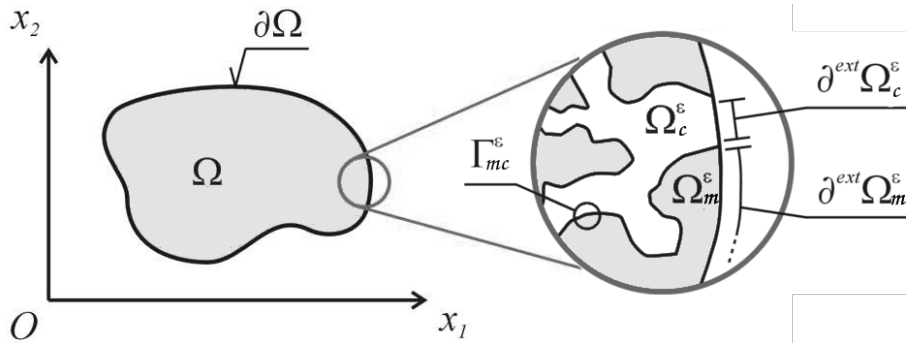

Figure 4: Decomposition of domain Ω, source [20]

In our study, only the first case with connected porosity is considered. Because of the assumption of double-porous medium, the similar behavior is observed also between the different scale levels. The pores on different scale levels can be also mutually connected or disconnected. We consider the connected porosities, thus, the fluid pressure in the whole fluid is represented just by one scalar value.

Further, we need to define the outer boundary, $\partial_{ext}\Omega_c^\varepsilon \subset \partial\Omega$ and $\partial_{ext}\Omega_m^\varepsilon \subset \partial\Omega$, [20], [25], [26], such that

$$\partial_{ext}\Omega_m^\varepsilon = \partial\Omega_m^\varepsilon \setminus \Gamma_{mc} = \partial\Omega_m^\varepsilon \cap \partial\Omega, \tag{15}$$

$$\partial_{ext}\Omega_c^\varepsilon = \partial\Omega_c^\varepsilon \setminus \Gamma_{mc} = \partial\Omega_c^\varepsilon \cap \partial\Omega. \tag{16}$$

By the symbol $\partial_{ext}\Omega_m^\varepsilon$ we denote the inner boundary of the matrix and $\partial_{ext}\Omega_m^\varepsilon$ the inner boundary of canals. In other words, the $\partial_{ext}\Omega_m^\varepsilon$ represents the exit of the canal into the outer surface of the porous body Ω, [20].

Illustration of Ω decomposition can be seen on the Fig.4.

4.2.4 Representative periodic cell

We consider the body Ω on the macroscopic scale with coordinate system in the N-dimensional space $0, x_1, x_2, ..., x_N$. Thanks to the assumption of the periodic material, the body Ω is on the microscale represented by periodically repeated cell Y with coordinate system $\hat{0}, y_1, y_2, ..., y_N$ and

$$Y = \prod_{i=1}^{N} (0, \hat{y}_i) \tag{17}$$

The cell Y is called the representative periodic cell (RPC) and has the shape of an N-dimensional block with the length of side $\hat{y}_i$, [20].

Similarly to the domain Ω, the RPC Y can be divided into two subdomains Y_m and Y_c with interface Γ_{mc}, such that

$$Y = Y_m \cup Y_c \cup \Gamma_{mc}, \quad Y_c = Y \setminus \bar{Y}_m, \quad \Gamma_{mc} = \bar{Y}_m \cap \bar{Y}_c. \tag{18}$$

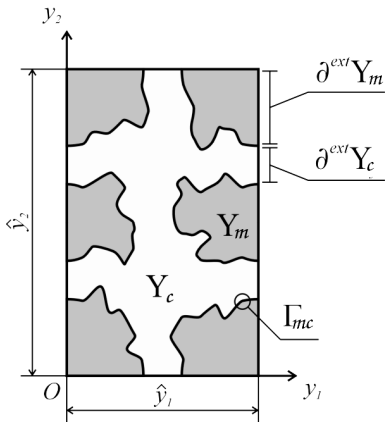

Table 1: Decomposition of RPC Y, source [20]

The outer boundary of RPC Y is also defined similarly to the domain Ω,

$$\partial_{ext} Y_m = \partial Y_m \setminus \Gamma_{mc} = \partial Y_m \cap \partial Y, \tag{19}$$

$$\partial_{ext} Y_c = \partial Y_c \setminus \Gamma_{mc} = \partial Y_c \cap \partial Y. \tag{20}$$

As was mentioned above, the RPC Y creates a characteristic sub-unit. By periodical repeating of Y we can obtain the whole domain Ω.

The shape and dimension of the RPC Y is naturally subjected to the microstructure of the porous medium. But at this moment we don't know the particular microstructure, so just for simplicity, we can assume the Y with a unit side length, i.e. $\hat{y}_i = 1, i = 1, 2, 3$, and so

$$Y = \{\mathbf{y}; \mathbf{y} \in (0, 1)^N\}. \tag{21}$$

This represents RPC Y as the unit square in $\mathbb{R}^2$ or the cubic cell in $\mathbb{R}^3$. Such imagination of Y has a measure (in $\mathbb{R}^3$ volume of Y) $|Y| = 1$.

Finally, the definition of Y_m and Y_c allows us to introduce the porosity ϕ in the form

$$\phi = \frac{|Y_c|}{|Y|}. \tag{22}$$

4.2.5 Relation between the macroscopic and the microscopic level

The relation between the macroscopic domain Ω and the microscopic domain represented by Y is, according to [20] and [4], as follows

$$\Omega = \text{int} \bigcup_{\text{k}\in\mathbb{K}_\Omega} \bar{\text{Y}}^\varepsilon(\boldsymbol{\xi}), \tag{23}$$

where by $\bar{Y}^\varepsilon(\boldsymbol{\xi})$ we denote the closure of the domain Y^ε, which is defined as projection of Y diminished by scale ε. The domain $\mathbb{K}_\Omega \subset \mathbb{Z}$ is defined as set of integer multi-indices satisfying the following

$$Y^\varepsilon(\boldsymbol{\xi}) = \boldsymbol{\xi} + \varepsilon Y, \quad \xi_i = k_(i)\varepsilon\hat{y}_i \tag{24}$$

where ξ_i is the macroscopic coordination of the bottom left corner of RPC Y_i with position k_i in the periodical grid, $[k_1, k_2, ..., k_i, ..., k_N]$, [20].

The coordinates can be split into "coarse" and "fine" parts of the position, for illustration see Fig. 5. For a finite $\varepsilon > 0$:

$$\mathbf{x} = \varepsilon\left[\frac{x}{\varepsilon}\right]_y + \varepsilon\left\{\frac{x}{\varepsilon}\right\}_y = \xi + \varepsilon\mathbf{y}, \tag{25}$$

where

$$\mathbf{y} = \left\{\frac{x}{\varepsilon}\right\}_y \in Y, \quad \xi = \varepsilon\left[\frac{x}{\varepsilon}\right]_y, \tag{26}$$

[18], [20], [26].

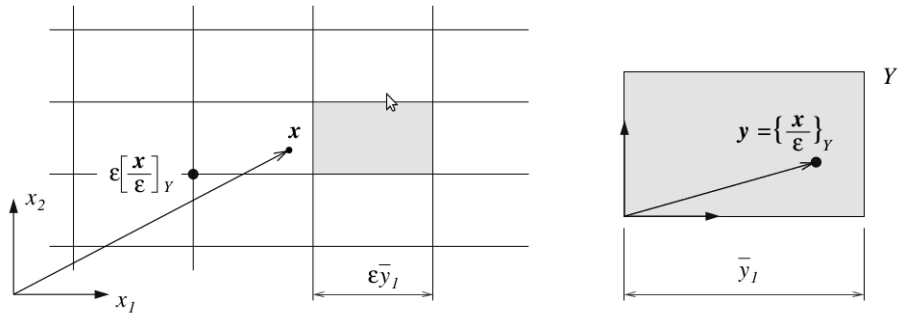

Figure 5: Lattice periodic structure of body Ω. Coordinates split into "coarse" and "fine", source [23]

4.2.6 Asymptotic analysis in homogenization

Let us put the poroelastic problem aside for the moment and consider the problem on the heterogeneous domain with a periodic structure in general. Such problem can be multi-scale but in the following text we consider just a two-scale model with microscopic and macroscopic level structure. The behavior of this model is influenced by the scale parameter ε. We search for a way to simplify this two-scale model and also to project its microscopic structure onto its behavior on the macroscopic scale.

A suitable method is an asymptotic analysis of the system. The main principle of this method is that we let the parameter ε "vanish" from the system of the partial differential equations describing the problem, in limit $\varepsilon \to 0$. This results into a new limit PDE system describing the homogenized macroscopic model with homogenized coefficients, which describe the influence of heterogeneities in micro-scale onto macroscopic behavior.

The following example is used for a better imagination of the homogenization method, see Fig. 6. We have the porous microstructure with a simple geometry of the pores. The parameter ε defines the ratio between the diameters of macro- and microstructure. When we diminish the ε, the heterogeneities are getting less and less visible and then for $\varepsilon \to 0$ the material appears to be without heterogeneities. We obtain the homogenized or quasi-homogeneous material, but its mechanical properties differ from the ones of the heterogeneous scelet of the porous medium. The material coefficients of the heterogeneous scelet are components of fourth-order stiffness tensor $\mathbb{D}$ while the homogenized material is described by a symmetric tensor of effective stiffness denoted by $\mathbb{A}$.

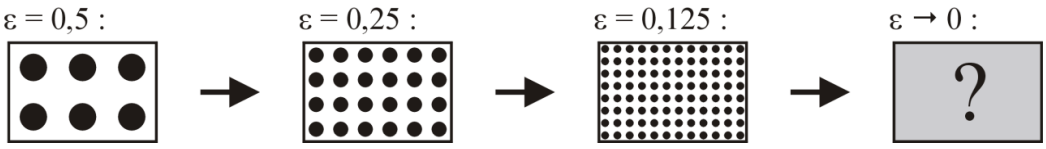

Figure 6: Main principle of homogenization method, source [20]

It may seem that the homogenized model cannot refer to any real material, because the relations obtained by asymptotic analysis are for $\varepsilon \to 0$ while the real models are for structures with finite size of period $\varepsilon Y, \varepsilon \to \varepsilon_0 > 0$. But note that the more heterogeneous material the smaller is the parameter ε_0 and the better the limit relations for $\varepsilon \to 0$ describe the real model. With this in mind, we can introduce a homogenization method used for the derivation of the homogenized model.

This section was written according to the information in [20].

4.2.7 Unfolding operator

In order to obtain the homogenized coefficients of cortical bone tissue, a couple of methods are widely used. For example in [7], the method Mori-Tanaka was used, while [9] uses the Eshelby's

homogenization method. But those methods do not work with the system of PDE but only with direct addition and averaging of stiffness tensors. Our aim is to follow the homogenization procedure published in [25], where the unfolding method was used. In what follows, we define the unfolding operator and its basic properties.

We consider that the domain Ω is obtained from periodic microstructure generated by RPC Y, which is defined in sections 4.2.4 and 4.2.5, with relations between coordinates Eq.(25),(26). By virtue of the coordinate decomposition into "coarse" and "fine" parts, any function $\psi = \psi(\boldsymbol{x})$ can be unfolded into a function of $\boldsymbol{x}$ and $\boldsymbol{y}$, [26]. The unfolding operator can be defined (because of specific domain restriction Eq.(25)) as follows

$$\mathcal{T}_\varepsilon(\psi(\boldsymbol{x})) = \tilde{\psi}(\boldsymbol{\xi}(\boldsymbol{x}), \boldsymbol{y}(\boldsymbol{x})) = \psi(\boldsymbol{\xi}(\boldsymbol{x}) + \varepsilon \boldsymbol{y}), \tag{27}$$

where $\boldsymbol{\xi}(\boldsymbol{x})$ and $\boldsymbol{y}(\boldsymbol{x})$ are associated with the position $\boldsymbol{x} \in \Omega$.

The unfolding operator $\mathcal{T}_\varepsilon(\psi)$ has the following three important properties: For all functions ψ and χ:

$$(i) \qquad \mathcal{T}_\varepsilon(\psi(\boldsymbol{x})\chi(\boldsymbol{x})) = \mathcal{T}_\varepsilon(\psi(\boldsymbol{x}))\mathcal{T}_\varepsilon(\chi(\boldsymbol{x})), \tag{28}$$

$$(ii) \qquad \int_\Omega \psi(\boldsymbol{x}) dx = \int_\Omega \frac{1}{|Y|} \int_Y \mathcal{T}_\varepsilon(\psi)(\boldsymbol{x}, \boldsymbol{y}) dx dy = \fint_{\Omega \times Y} \mathcal{T}_\varepsilon(\psi)(\boldsymbol{x}, \boldsymbol{y}), \tag{29}$$

$$(iii) \qquad \mathcal{T}_\varepsilon(\nabla_x \psi(\boldsymbol{x})) = \frac{1}{\varepsilon} \nabla_y (\mathcal{T}_\varepsilon(\psi)(\boldsymbol{x}, \boldsymbol{y})), \tag{30}$$

where the symbols ∇_x and ∇_y denote gradient operators with respect to $\boldsymbol{x}$ and $\boldsymbol{y}$, respectively. In order to simplify the following relations, we introduce the abbreviation

$$\frac{1}{|Y|} \int_{Y_a} = \fint \quad \text{and} \quad \frac{1}{|\mathrm{Y}|} \int_{\Omega \times \mathrm{Y}} = \fint_{\Omega \times \mathrm{Y}}. \tag{31}$$

The unfolding operator also transforms the integration domain Ω to the $\Omega \times Y$ allowing us to use weak convergence in a functional Sobolev space $W(\Omega, Y)$ that possesses enough regularity for the functions defined in $\Omega \times Y$. The unfolding operator represents the main tool of unfolding homogenization method (UFM).

4.3 Homogenization of poroelasticity

The homogenization of poroelasticity of the cortical bone tissue is presented in this section. Note that we repeat the homogenization procedure in order to obtain the homogenized model proposed in [25]. The general principles from the previous section are used, but because of the assumption of two level poroelasticity, we have to lightly modify them. In the following text, we use two superscripts: α for microscopic (or $\alpha-$) level and β for mesoscopic ($\beta-$) level. First, we focus on

the microscopic scale problem. Thus, the $\alpha-$ level is described by coordination of the micro- and $\beta-$ level of the macroscopic level in the previous section.

4.4 Mathematical model on the microscopic level

Let us consider the domain $\Omega^\alpha \subset \mathbb{R}^3$, which represents the microscopic scale. Similarly to the section above, the domain $\Omega^\alpha \subset \mathbb{R}$ is decomposed into the (solid) matrix $\Omega_m^{\alpha,\varepsilon}$ and canals $\Omega_c^{\alpha,\varepsilon}$ as follows:

$$\Omega^\alpha = \Omega_m^{\alpha,\varepsilon} \cup \Omega_c^{\alpha,\varepsilon} \cup \Gamma^{\alpha,\varepsilon}, \quad \Omega_c^{\alpha,\varepsilon} = \Omega^{\alpha,\varepsilon} \setminus \bar{\Omega}_m^{\alpha,\varepsilon}, \quad \Gamma^{\alpha,\varepsilon} = \bar{\Omega}_m^{\alpha,\varepsilon} \cap \bar{\Omega}_c^{\alpha,\varepsilon} \ . \tag{32}$$

and with the outer boundaries $\partial_{ext}\Omega_c^{\alpha,\varepsilon} \subset \partial\Omega^\alpha$ and $\partial_{ext}\Omega_m^{\alpha,\varepsilon} \subset \partial\Omega^\alpha$, such that

$$\partial_{ext}\Omega_m^{\alpha,\varepsilon} = \partial\Omega_m^{\alpha,\varepsilon} \setminus \Gamma_{mc} = \partial\Omega_m^{\alpha,\varepsilon} \cap \partial\Omega^\alpha, , \tag{33}$$

$$\partial_{ext}\Omega_c^{\alpha,\varepsilon} = \partial\Omega_c^{\alpha,\varepsilon} \setminus \Gamma_{mc} = \partial\Omega_c^{\alpha,\varepsilon} \cap \partial\Omega^\alpha. \tag{34}$$

In what follows, we will use the same notation as in [25] to prevent confusion. By symbols ∇ and $\nabla\cdot$ the gradient and divergence operators, respectively. The scalar product is denoted by "." and the symbol ":" between tensors of any order denotes their double contraction. The superscript s in the gradient operator ∇^s denotes its symmetric part. Above and throughout the text, the superscript $^\varepsilon$ refers to the scale-dependence, where the scale parameter ε describes the ration of the characteristic sizes of the micro- and mesoscopic level,

$$\varepsilon = \frac{L_\alpha}{L_\beta}. \tag{35}$$

We find it appropriate to discus the functional dependency of the elastic tensor $\mathbf{D}$ on the scale parameter ε in this place. According to the assumption of the material periodicity, the functional dependence on $\mathbf{y}$ is periodical in Y. To this property we usually refer as Y-periodicity. In heterogeneous RPC Y, the elastic tensor $\mathbf{D}$ is a function of $\mathbf{y}$ and thus it is also Y-periodic. But in contrast, we want to obtain the homogeneous material on the mesoscopic scale, thus the elasticity tensor components are independent on the mesoscopic system of coordinates $\mathbf{x}$. Therefore, the components of the elasticity tensor are

$$D_{ijkl} = D_{ijkl}(\mathbf{y}). \tag{36}$$

However, according to the Eq.26, $\mathbf{y}(\mathbf{x}) = \{\frac{\mathbf{x}}{\varepsilon}\}_y$, thus,

$$D^\varepsilon_{ijkl}(\mathbf{x}) = D_{ijkl}(\frac{\mathbf{x}}{\varepsilon}). \tag{37}$$

The superscript ε stands for ε Y-periodicity of $\mathbb{D}$ in the system of coordinates x, thus depending indirectly on $\mathbf{x}$, [18].

Now let us introduce the microscopic scale problem of poroelasticity considering all assumptions given in the section above. The linear poroelastic body in three dimensional space, represented

by the domain $\Omega^\alpha \subset \mathbb{R}^3$, is statically loaded by volume-force field $\mathbf{f}^{\alpha,\varepsilon}$ in $\Omega_m^{\alpha,\varepsilon}$ and surface-force field $\mathbf{g}^{\alpha,\varepsilon}$ on $\partial_{ext}\Omega_m^{\alpha,\varepsilon}$. The loading of the body causes deformation of the matrix, which results to the extension of pores. The fluid in the pores is a compressible Newtonian, thus the pore extension is a little compressed while creating the pressure on the canal-matrix interface Γ_{mc} and some fluid leaks from $\Omega_c^{\alpha,\varepsilon}$ into the outer space through $\partial_{ext}\Omega_c^{\alpha,\varepsilon}$.

Using the tensor notation of Eq.(3) and (4), the linear poroelasticity problem is described by the following equilibrium equation

$$-\nabla(\mathbb{D}^{\alpha,\varepsilon}\nabla^S\mathbf{u}^{\alpha,\varepsilon}) = \mathbf{f}^{\alpha,\varepsilon}, \quad \text{in} \quad \Omega_m^{\alpha,\varepsilon}, \tag{38}$$

with boundary conditions

$$\mathbf{n}^m.\mathbb{D}^{\alpha,\varepsilon}\nabla^S\mathbf{u}^{\alpha,\varepsilon} = \mathbf{g}^{\alpha,\varepsilon}, \quad \text{on} \quad \partial_{ext}\Omega_m^{\alpha,\varepsilon}, \tag{39}$$

$$\mathbf{n}^m.\mathbb{D}^{\alpha,\varepsilon}\nabla^S\mathbf{u}^{\alpha,\varepsilon} = -\bar{p}^{\alpha,\varepsilon}, \quad \text{on} \quad \Gamma^{\alpha,\varepsilon} \tag{40}$$

,where $\mathbf{u}^{\alpha,\varepsilon}$ is the displacement of the solid matrix and $\bar{p}^{\alpha,\varepsilon}$ is the fluid pressure. This system of equations is completed by the balance of the fluid mass defined as follows

$$\int\limits_{\partial\Omega_c^{\alpha,\varepsilon}} \tilde{\mathbf{u}}^{\alpha,\varepsilon}.\mathbf{n}^c dS_x + \gamma^\alpha \bar{p}^{\alpha,\varepsilon}|\Omega_c^{\alpha,\varepsilon}| = -J^{\alpha,\varepsilon}, \tag{41}$$

which means that the fluid volume $-J^{\alpha,\varepsilon}$ injected from outside through $\partial_{ext}\Omega_c^{\alpha,\varepsilon}$ into $\Omega_c^{\alpha,\varepsilon}$ is balanced by the increase of the pore volume and by the fluid compression resulting in an increased pressure $-\bar{p}^{\alpha,\varepsilon}$, [25]. By˜we denote a matrix-to-canal extension. The symbols $\mathbf{n}^m$ and $\mathbf{n}^c$ denote the outer unit normal vectors of the boundaries $\partial\Omega_m^{\alpha,\varepsilon}$ and $\partial\Omega_c^{\alpha,\varepsilon}$, respectively.

Note that the solvability condition yields

$$\int\limits_{\partial_{ext}\Omega_m^{\alpha,\varepsilon}} \mathbf{g}^{\alpha,\varepsilon} dS_x + \int\limits_{\Omega_m^{\alpha,\varepsilon}} \mathbf{f}^{\alpha,\varepsilon} dV_x = \mathbf{0}, \tag{42}$$

where dS_x and dV_x stand for the differential elements of the surface and volume respectively.

The weak formulation of the problem given by the system Eq.(38)-(41) is more suitable for further application. First, we have to define the space of the test variables, which comply to the boundary conditions of the problem Eq.(38)-(41). We denote the Sobolev space of vector function as $\mathbf{H}^1$. Now we can introduce the test variable $\boldsymbol{v} \in \mathbf{H}^1$

Now we rewrite the system Eq.(38)-(41) in the terms of weak formulation by "multiplicating" by the testing function $\boldsymbol{v}$ and applying per-partes integration. Through this, we obtain the following

weak formulation problem: find $(\boldsymbol{u}^{\alpha,\varepsilon}, \bar{p}^{\alpha,\varepsilon}) \in \mathbf{H}^1(\Omega_m^{\alpha,\varepsilon}) \times \mathbb{R}$ such that

$$\int_{\Omega_m^{\alpha,\varepsilon}} (\mathbb{D}^{\alpha,\varepsilon} \nabla^s \boldsymbol{u}^{\alpha,\varepsilon}) : \nabla^s \boldsymbol{v} \, \mathrm{dV}_x + \bar{p}^{\alpha,\varepsilon} \int_{\Gamma_m^{\alpha,\varepsilon}} \boldsymbol{n}^m . \boldsymbol{v} \, \mathrm{dS}_x =$$

$$= \int_{\partial_{ext}\Omega_m^{\alpha,\varepsilon}} \boldsymbol{g}^{\alpha,\varepsilon} - \boldsymbol{v} \, \mathrm{dS}_x + \int \boldsymbol{f}^{\alpha,\varepsilon} . \boldsymbol{v} \, \mathrm{dV}_x, \quad \forall \boldsymbol{v} \in \mathbf{H}^1(\Omega_m^{\alpha,\varepsilon}), \tag{43}$$

$$\int_{\partial\Omega_c^{\alpha,\varepsilon}} \tilde{\mathbf{u}}^{\alpha,\varepsilon} . \mathbf{n}^c dS_x + \gamma^\alpha \bar{p}^{\alpha,\varepsilon} |\Omega_c^{\alpha,\varepsilon}| = -J^{\alpha,\varepsilon}. \tag{44}$$

4.4.1 Limit problem

Let us consider the problem on Ω^α defined by the system of PDE Eq.(38)-Eq.(41). The domain Ω^α is obtained from a periodic microstructure generated by RPC Y^α with the decomposition similar to 4.2.4

$$Y^\alpha = Y_m^\alpha \cup Y_c^\alpha \cup \Gamma_{mc}^\alpha, \quad Y_c^\alpha = Y^\alpha \setminus \bar{Y}_m^\alpha, \quad \Gamma_{mc}^\alpha = \bar{Y}_m^\alpha \cap \bar{Y}_c^\alpha. \tag{45}$$

and with the outer boundary,

$$\partial_{ext} Y_m^\alpha = \partial Y_m^\alpha \setminus \Gamma_{mc}^\alpha = \partial Y_m^\alpha \cap \partial Y^\alpha, \tag{46}$$

$$\partial_{ext} Y_c^\alpha = \partial Y_c^\alpha \setminus \Gamma_{mc}^\alpha = \partial Y_c^\alpha \cap \partial Y^\alpha. \tag{47}$$

.

The canal part Y_c^α generates a set obtained by the ε-periodicity as

$$\Omega_c^{\alpha,\varepsilon} = \varepsilon(\overline{Y}_c^\alpha + k_i \hat{yb}_i) \cap \Omega^\alpha, \quad k \in \mathbb{Z}^3 \tag{48}$$

where $\mathbb{Z}$ is a set of integers. Thus, the matrix part can be expressed as $\Omega_m^{\alpha,\varepsilon} = \Omega^\alpha \setminus \overline{\Omega}_c^{\alpha,\varepsilon}$.

We consider the material coefficients piecewise-continuous in the domain Ω^α, with incontinuities on $\Gamma_{mc}\alpha$, thus we may introduce its following decomposition

$$D_{ijkl}^{\alpha,\varepsilon}(\boldsymbol{x}) = \chi_m^{\alpha,\varepsilon}(\boldsymbol{x}) D_{ijkl}^{m,\alpha,\varepsilon}(\boldsymbol{x}) + \chi_c^{\alpha,\varepsilon}(\boldsymbol{x}) D_{ijkl}^{c,\alpha,\varepsilon}(\boldsymbol{x}), \tag{49}$$

where the symbol $\chi_d^{\alpha,\varepsilon}$ for $d = m, c$ denotes the characteristic function of the domain $\Omega_d^{\alpha,\varepsilon}$. The values of parameters $D_{ijkl}^{d,\alpha,\varepsilon}$ are defined with respect to material points in microstructure, thus they are independent on the parameter ε.

Now we apply the unfolding operation Eq.(25), which associates uniquely any $\boldsymbol{x} \in \Omega^\alpha$ to any

$\boldsymbol{y} \in Y^\alpha$, on the Eq.(49), thus we obtain

$$D^{\alpha,\varepsilon}_{ijkl}(\boldsymbol{x}) = \begin{cases} D^{m,\alpha,\varepsilon}_{ijkl}(\boldsymbol{y}) & \text{iff } \boldsymbol{y} \in Y^\alpha_m \\ D^{c,\alpha,\varepsilon}_{ijkl}(\boldsymbol{y}) & \text{iff } \boldsymbol{y} \in Y^\alpha_c \end{cases} \tag{50}$$

In what follows, we use a weak formulation of the problem given by Eq.(43) and (44).

When using the UFM, we first compute the *a priory* estimate of solution, which is uniform and depends on ε. Then we use standard theorem, see [4], which gives the limit equations. These equations represent the macroscopic, unoscillation part and the fluctuation part, which provide the gradient correction of the limit "macroscopic" solution, [26]. In other words, we decompose any function into its "macroscopic" and "microscopic parts", which should capture the fluctuations. Note, that in this context the term "microscopic" refers to the scale that we want to upscale, while "macroscopic" is the scale one level higher. According to [26], we shall consider the following recovery sequences associated with $\boldsymbol{u}^{\alpha,\varepsilon}$

$$\boldsymbol{u}^{R,\varepsilon}(\boldsymbol{x}) = \boldsymbol{u}^\varepsilon_0(\boldsymbol{x}, \frac{\boldsymbol{x}}{\varepsilon}) + \varepsilon \boldsymbol{u}^\varepsilon_1(\boldsymbol{x}, \frac{\boldsymbol{x}}{\varepsilon}) \tag{51}$$

where $\boldsymbol{u}^\varepsilon_0(\boldsymbol{x}, .)$ and $\boldsymbol{u}^\varepsilon_1(\boldsymbol{x}, .) \in W_\#(Y^\alpha)$, which is a space of Y-periodic functions.

Now, we apply the unfolding operator $\mathcal{T}_\varepsilon(\psi)$ on $\boldsymbol{u}^{R,\varepsilon}(\boldsymbol{x})$ which gives us

$$\mathcal{T}_\varepsilon\Big(\boldsymbol{u}^{R,\varepsilon}(\boldsymbol{x})\Big) = \boldsymbol{u}^\varepsilon_0(\boldsymbol{\xi} + \varepsilon \boldsymbol{y}, \boldsymbol{y}) + \varepsilon \boldsymbol{u}^\varepsilon_1(\boldsymbol{\xi} + \varepsilon \boldsymbol{y}, \boldsymbol{y}). \tag{52}$$

Moreover, the unfolding operator allows us to use weak convergence, thus the following convergences are taken in account

$$\boldsymbol{u}^\varepsilon_0 \rightharpoonup \bar{\boldsymbol{u}}^\varepsilon_0(\boldsymbol{x}) \ \text{ weakly in } \mathbf{W}(Y^\alpha, \Omega^\alpha), \tag{53}$$

$$\mathcal{T}_\varepsilon(\boldsymbol{u}^\varepsilon_0) \rightharpoonup \boldsymbol{u}^\varepsilon_0(\boldsymbol{x}, \boldsymbol{y}) \ \text{ weakly in } \mathbf{W}(Y^\alpha, \Omega^\alpha), \tag{54}$$

$$\mathcal{T}_\varepsilon(\boldsymbol{u}^\varepsilon_1) \rightharpoonup \boldsymbol{u}^\varepsilon_1(\boldsymbol{x}, \boldsymbol{y}) \ \text{ weakly in } \mathbf{W}(Y^\alpha, \Omega^\alpha). \tag{55}$$

The $\bar{\boldsymbol{u}}^\varepsilon_0(\boldsymbol{x})$ is the mean value of $\boldsymbol{u}^\varepsilon_0(\boldsymbol{x})$ given by

$$\frac{1}{|Y^\alpha|} \int\limits_{Y^\alpha} \boldsymbol{u}^\varepsilon_0(\boldsymbol{x}, \boldsymbol{y}) d\boldsymbol{x} d\boldsymbol{y}. \tag{56}$$

Very important point in the homogenization is the match between "micro-" and "macroscale". The direct link is inherited from gradients of the fluctuating functions. We introduce the unfolding of the gradient of $\boldsymbol{u}^{R,\varepsilon}$ using Eq.(30) and (52)

$$\mathcal{T}_\varepsilon\Big(\nabla \boldsymbol{u}^{R,\varepsilon}\Big) = \frac{1}{\varepsilon}\nabla_y\left[\boldsymbol{u}_0^\varepsilon(\boldsymbol{\xi}+\varepsilon\boldsymbol{y},\boldsymbol{y}) + \varepsilon \boldsymbol{u}_1^\varepsilon(\boldsymbol{\xi}+\varepsilon\boldsymbol{y},\boldsymbol{y})\right] =$$
$$= \nabla_x \boldsymbol{u}_0^\varepsilon(\boldsymbol{x},\boldsymbol{y}) + \frac{1}{\varepsilon}\nabla_y \boldsymbol{u}_0^\varepsilon(\boldsymbol{x},\boldsymbol{y}) + \varepsilon\nabla_x \boldsymbol{u}_1^\varepsilon(\boldsymbol{x},\boldsymbol{y}) + \nabla_y \boldsymbol{u}_1^\varepsilon(\boldsymbol{x},\boldsymbol{y}). \tag{57}$$

Further, we may evaluate the limits of the following integral forms, for any suitable test function $\boldsymbol{\psi}$ we consider the case of minor fluctuation—gradient correction:

$$\int_{\Omega^\alpha} \nabla \boldsymbol{u}^{R,\varepsilon}(\boldsymbol{x})\boldsymbol{\psi}(\boldsymbol{x},\frac{\boldsymbol{x}}{\varepsilon}) = \fint_{\Omega^\alpha\times Y^\alpha} \mathcal{T}_\varepsilon\Big(\nabla \boldsymbol{u}^{R,\varepsilon}\Big)(\boldsymbol{x},\boldsymbol{y})\boldsymbol{\psi}(\boldsymbol{x},\boldsymbol{y}) \to \fint_{\Omega^\alpha\times Y^\alpha} (\nabla_x \boldsymbol{u}_0 + \nabla_y \boldsymbol{u}_1)\boldsymbol{\psi}, \tag{58}$$

and $\nabla_y \boldsymbol{u}_0 = 0$, i.e.$\bar{\boldsymbol{u}}_0(\boldsymbol{x}) = \boldsymbol{u}_0(\boldsymbol{x})$. This condition is necessary to prevent blow up due $1/\varepsilon \to \infty$.

This case will characterize the displacement and related deformations. The test function $\boldsymbol{\psi}$ can be chosen quite general but with respect to ε in a suitable norm. This can be the most simply accomplished by considering the test function $\boldsymbol{v}^\varepsilon$ with the same decomposition as $\boldsymbol{u}^{R,\varepsilon}$, Eq.(51):

$$\boldsymbol{v}^\varepsilon(\boldsymbol{x}) = \boldsymbol{v}_0^\varepsilon(\boldsymbol{x}) + \varepsilon \boldsymbol{v}_1^\varepsilon(\boldsymbol{y}), \tag{59}$$

Now we can substitute the displacement and the test function in the system Eq.(43)-(44) by their previously introduced decomposition given by Eq.(51) and (59) and then we apply the unfolding operator on it, thus we obtain

$$\int_{\Omega^\alpha} (\mathbb{D}^{\alpha,\varepsilon}(\boldsymbol{y})\nabla^s \boldsymbol{u}^{R,\varepsilon}) : \nabla^s \boldsymbol{v}^\varepsilon = \fint_{\Omega^\alpha\times Y_m^\alpha} (\mathbb{D}^{\alpha,\varepsilon}(\boldsymbol{y})\mathcal{T}_\varepsilon\Big(\nabla^s \boldsymbol{u}^{R,\varepsilon}\Big)) : \mathcal{T}_\varepsilon(\nabla^s \boldsymbol{v}^\varepsilon) =$$
$$= \fint_{\Omega^\alpha\times Y_m^\alpha} (\mathbb{D}^{\alpha,\varepsilon}(\boldsymbol{y})\nabla_x \boldsymbol{u}_0^\varepsilon + \nabla_y \boldsymbol{u}_1^\varepsilon + \varepsilon\nabla_x \boldsymbol{u}_1^\varepsilon) : (\nabla_x \boldsymbol{v}_0^\varepsilon + \nabla_y \boldsymbol{v}_1^\varepsilon + \varepsilon\nabla_x \boldsymbol{v}_1^\varepsilon), \tag{60}$$

With the use of relation (58) we can evaluate the limit of unfolded bilinear form from weak formulation of equilibrium Eq.(43) as follows

$$\fint_{\Omega^\alpha\times Y_m^\alpha} (\mathbb{D}^\alpha\nabla_x \boldsymbol{u}_0 + \nabla_y \boldsymbol{u}_1) : (\nabla_x \boldsymbol{v}_0 + \nabla_y \boldsymbol{v}_1) \tag{61}$$

Now we have to deal with the second term in the Eq.(43). Because this term is interface integral, we cannot just simply use the same approach like for integrals over the domain. Instead we introduce the lemmas taken from [27] which deal with interface integral convergence as follows:
Lemma 1. Let ϕ_s^α and ϕ^α be the surface and the volume fractions of the fluid phase, respectively,

then

$$\int_{\Gamma^\varepsilon} \boldsymbol{v}.\boldsymbol{n}^m \, \mathrm{dS}_x \to \int_{\partial\Omega} \phi_s^\alpha \boldsymbol{v}^0.\boldsymbol{n} \, \mathrm{dS}_x - \int_\Omega \phi^\alpha \mathrm{div}_x \boldsymbol{v}^0 + \int_\Omega \fint_{\Gamma_Y} \boldsymbol{v}^1.\boldsymbol{n}^m \, \mathrm{dS}_y. \tag{62}$$

If $\phi^\alpha = \phi_s^\alpha$ on $\partial\Omega$ (and in sense oh ϕ_s^α extended into Ω)

$$\int_{\Gamma^\varepsilon} \boldsymbol{v}^\varepsilon.\boldsymbol{n}^m \, \mathrm{dS}_x \to \int_\Omega \boldsymbol{v}^0.\partial_x \phi^\alpha + \int_\Omega \fint_{\Gamma_Y} \boldsymbol{v}^1.\boldsymbol{n}^m \, \mathrm{dS}_y. \tag{63}$$

The proof of this Lemma can be found in [27].

Further, let us assume the weak convergence of pressure $\bar{p}^{\alpha,\varepsilon}$ and flow $J^{\alpha,\varepsilon}$ as

$$\bar{p}^{\alpha,\varepsilon} \to \bar{p}^\alpha, \tag{64}$$

$$J^{\alpha,\varepsilon} \to J^\alpha. \tag{65}$$

and the convergence of external forces as

$$\chi_m^\varepsilon \boldsymbol{f}^{\alpha,\varepsilon} \rightharpoonup (1 - \phi_s^\alpha)\boldsymbol{f}^\alpha = \hat{\boldsymbol{f}}^\alpha, \tag{66}$$

where by the symbol ϕ^α we denote the porosity on microscopic level as volume fraction $\frac{|Y_c^\alpha|}{|Y^\alpha|}$ and $\boldsymbol{f}^\alpha \in H^1(\Omega^\alpha)$ is a local averaged volume force applied on the matrix. Further, we assume the existence of a surface force $\boldsymbol{g}^\alpha$ with convergence

$$\int_{\partial_{ext}\Omega_m^{\alpha,\varepsilon}} \boldsymbol{g}^{\alpha,\varepsilon}.\boldsymbol{v} \, \mathrm{dS}_x \to \int_{\partial\Omega^\alpha} (1 - \phi_s^\alpha)\boldsymbol{g}^\alpha.\boldsymbol{v} \, \mathrm{dS}_x = \int_{\partial\Omega^\alpha} \hat{\boldsymbol{g}}^\alpha.\boldsymbol{v} \, \mathrm{dS}_x, \tag{67}$$

for any test function $\boldsymbol{v} \in H^1$. By ϕ_s^α we denote the exterior surface porosity, which we can choose $\phi_s^\alpha = \phi^\alpha$ for statistically distributed pores, [25].

Finally, by applying the Lemma.1 on the interface integrals in the weak formulation of the problem Eq.(43) and (44) and using the unfolded bilinear form Eq.(61) and the convergences above Eq.(64)-(67), we can introduce the following limit weak two-scale formulation: Find $(\boldsymbol{u}^\alpha, \boldsymbol{u}_1^\alpha) \in \mathbf{H}^1(\Omega^\alpha) \times L^2(\Omega^\alpha; \mathbf{H}^1_\#(Y^\alpha))$ and $\bar{p}^\alpha \in \mathbb{R}$ satisfying

$$\fint_{\Omega^\alpha \times Y_m^\alpha} (\mathbb{D}^\alpha \nabla_x \boldsymbol{u}_0 + \nabla_y \boldsymbol{u}_1) : (\nabla_x \boldsymbol{v}_0 + \nabla_y \boldsymbol{v}_1) - \bar{p}^\alpha \int_{\Omega^\alpha} \left(\phi^\alpha \mathrm{div} \boldsymbol{v}^0 - \fint_{\gamma_Y^\alpha} \boldsymbol{v}^1 . n^m \, \mathrm{dS}_y \right) =$$

$$= \int_{\Omega^\alpha} \hat{\boldsymbol{f}}^\alpha . \boldsymbol{v}^0 + \int_{\partial\Omega^\alpha} \overline{\boldsymbol{g}^\alpha}(\bar{p}^\alpha) . \boldsymbol{v}^0 \, \mathrm{dS}_x,$$

$$\int_{\Omega^\alpha} \left(\phi^\alpha \mathrm{div} \boldsymbol{u}^\alpha - \fint_{\gamma_Y^\alpha} \boldsymbol{u}^1 . n^m \, \mathrm{dS}_y \right) + \bar{p}^\alpha \gamma^\alpha \phi^\alpha |\Omega^\alpha| = -J^\alpha. \tag{68}$$

4.4.2 Local problem

The local problem is relevant to the micro-scale and describes the deformation of the matrix in the entire Y^α, where the only effect of the fluid compartment is expressed by pressure $\bar{p}$. We choose the test function such that $\boldsymbol{v}_1(\boldsymbol{x}, \boldsymbol{y}) = \boldsymbol{w}(\boldsymbol{y})\theta(\boldsymbol{x}) \not\equiv 0$, all other test function components vanish. With the use of the limit of the weak two-scale formulation Eq.(68), we obtain the following equation, which is satisfied by $\boldsymbol{u}_1 \in \mathbf{H}^1_\#(Y)$

$$\fint_{Y^\alpha} \mathbb{D}^\alpha \nabla_y (\boldsymbol{u}_1 + \boldsymbol{\Pi}^{ij} \partial_j^x u_i) : (\nabla_y \boldsymbol{w}) - \bar{p}^\alpha \fint_{\Gamma_Y^\alpha} \boldsymbol{n}^m . \boldsymbol{w} = 0, \tag{69}$$

where $\boldsymbol{\Pi}^{ij}$ are the so-called transformation vectors $\boldsymbol{\Pi}^{ij} = (\Pi_k^{ij})$, $i, j, k = 1, 2, 3$, which can transform the macroscopic deformation $\boldsymbol{u}_0(\boldsymbol{x})$ from Ω^α into the coordinate system of RPC Y^α, as follows

$$\Pi_k^{ij} = y_j \delta_{ik}. \tag{70}$$

4.4.3 Homogenized coefficients

The effective coefficients, which we need to introduce the homogenized model, depend on some non-stationary effects induced by the deformation in the microstructure. They can be obtained by using a set of corrector basis functions. These functions can express the local displacement $\boldsymbol{u}_1(\boldsymbol{x}, \boldsymbol{y})$ using the linear combination of all the macroscopic quantities involved in the local problem. Thus, we introduce the corrector basis functions $\boldsymbol{\omega}^{ij}(\boldsymbol{y})$ and $\boldsymbol{\omega}^P(\boldsymbol{y})$ such that the local displacement $\boldsymbol{u}_1(\boldsymbol{x}, \boldsymbol{y})$ can be expressed as

$$\boldsymbol{u}_1(\boldsymbol{x}, \boldsymbol{y}) = \boldsymbol{\omega}^{ij}(\boldsymbol{y}) \partial_j u_i(\boldsymbol{x}) - \boldsymbol{\omega}^P(\boldsymbol{y}) \bar{p}, \tag{71}$$

where $\bar{p}$ is the constant fluid pressure in Ω^α,[20],[25].

Now, we can evaluate the corrector basis functions as a solution of the following problems,

[20],[25]: Find $\boldsymbol{\omega}^{ij} \in \mathbf{H}^1_{\#}(Y^\alpha)$ and $\boldsymbol{\omega}^P \in \mathbf{H}^1_{\#}(Y^\alpha)$ satisfying

$$a_y^m(\boldsymbol{\omega}^{ij} + \boldsymbol{\Pi}^{ij}, \mathbf{v}) = 0, \quad i, j = 1, , 3 \ , \tag{72}$$

$$a_y^m(\boldsymbol{\omega}^P, \mathbf{v}) = \fint_{\Gamma_m} \mathbf{v}.\mathbf{n}^m dS_y, \tag{73}$$

where a_y^m is the abbreviation of the bilinear form defined as follows:

$$a_y^m(\mathbf{w}, \mathbf{v}) = \fint_{Y_m} (\mathbb{D}\nabla_y^S \mathbf{w}) : \nabla_y^S \mathbf{v} \ . \tag{74}$$

4.4.4 Homogenized model

With the knowledge of the corrector basis functions $\boldsymbol{\omega}^{ij}$ and $\boldsymbol{\omega}^P$, we can introduce the set of homogenized coefficients, which describe the material properties on the mesoscopic level, as follows

$$A_{ijkl} = a_y^m(\boldsymbol{\omega}^{ij} + \boldsymbol{\Pi}^{ij}, \boldsymbol{\omega}^{kl} + \boldsymbol{\Pi}^{kl}), \tag{75}$$

$$B_{ij} = -\fint_{Y_m} \mathrm{div}_y \boldsymbol{\omega}^{ij}, \tag{76}$$

$$M = a_y^m(\boldsymbol{\omega}^P, \boldsymbol{\omega}^P), \tag{77}$$

where both the tensors $\mathbb{A}$ and $\mathbf{B}$ are symmetric, i.e. $\mathbb{A} = (A_{ijkl})$ satisfies $A_{ijkl} = A_{klij} = A_{jikl}$ and $\mathbb{B} = (B_{ij})$ satisfies $B_{ij} = B_{ji}$. It can be shown, [25], that $M > 0$. The tensor $\mathbb{A}$ is the effective tensor of the drained scelet. Further we introduce

$$\hat{\boldsymbol{B}} = \boldsymbol{B} + \phi \boldsymbol{I}, \quad \hat{M} = M + \phi\gamma, \tag{78}$$

where $\hat{\mathbf{B}}$ is the tensor of the Biot coefficients and $\hat{M}$ is the effective Biot modulus of compressibility, which expresses the complete compressibility of the fluid and the matrix deformed by the fluid pressure, [20], [25], [5].

4.4.5 Model of poroelasticity on the mesoscopic level

Using the assumption above, the mesoscopic problem can be obtained from the system Eq.(43) and (44) by homogenization in the form: find the displacement $\mathbf{u} \in V(\Omega)$ and the fluid pressure $\bar{p} \in \mathbb{R}$ which satisfy the following equations:

$$\int_\Omega (\mathbb{A}\nabla_x^S \mathbf{u} - \bar{p}\hat{\mathbf{B}}) : \nabla_x^S \mathbf{v} = \int_\Omega (1-\phi)\mathbf{f}.\mathbf{v} + \int_{\partial\Omega} \bar{\mathbf{g}}.\mathbf{v} dS_x \quad \forall \mathbf{v} \in V(\Omega) \tag{79}$$

$$\int_\Omega \hat{\mathbf{B}}\nabla_x^S \mathbf{u} + \bar{p}(M + \bar{\phi}\gamma)|\Omega| = -J, \quad \hat{\mathbf{B}} := \mathbf{B} + \phi\mathbf{I} \tag{80}$$

where $V(\Omega)$ is the space of kinematically admissible displacements. The J is the limit of the total flux $J^{\alpha,\varepsilon}$, $\bar{\boldsymbol{g}} := (1-\phi_s)\boldsymbol{g} + \phi_s(-\bar{p})\boldsymbol{n}$ is the mean surface traction and $\bar{\phi}$ is the mean porosity given by $\bar{\phi} = |\Omega|^{-1}\int_\Omega \phi$.

4.5 Homogenization on the mesoscopic level

In the previous text we introduced the unfolding method for obtaining the effective coefficients which refer to the mesoscopic porosity level. Because of the assumption of double porous material, we are just halfway to evaluate the effective coefficients related to macroscopic scale. In what follows, we use the homogenized coefficients $\mathbb{A}^\alpha, \hat{\mathbf{B}}^\alpha$ and M^α obtained by upscaling from microscopic to mesoscopic level and with them describe the behavior on mesoscopic scale. In other words, the mesoscopic level became "microscopic",from the homogenization method point of view, and by upscaling we want to obtain effective coefficients on the macroscopic level. But first, let us consider the domain Ω^β at the mesoscopic level decomposed similarly to $\alpha - level$ into the matrix $\Omega_m^{\beta,\varepsilon}$, which is formed by the porous medium associated with the upscaled microstructure if the $\alpha-$level, and "canals" $\Omega_c^{\beta,\varepsilon}$, which are filled with fluid and connected with pores of the $\alpha-$level. The decomposition is as follows

$$\Omega^\beta = \Omega_m^{\beta,\varepsilon} \cup \Omega_c^{\beta,\varepsilon} \cup \Gamma^{\beta,\varepsilon}, \quad \Omega_c^{\beta,\varepsilon} = \Omega^{\beta,\varepsilon} \setminus \bar{\Omega}_m^{\beta,\varepsilon}, \quad \Gamma^{\beta,\varepsilon} = \bar{\Omega}_m^{\beta,\varepsilon} \cap \bar{\Omega}_c^{\beta,\varepsilon}\ . \tag{81}$$

where, $\Gamma^{\beta,\varepsilon}$ refers to the interface between the subdomains. The outer boundaries of Ω^β are split into $\partial_{ext}\Omega_c^{\beta,\varepsilon} \subset \partial\Omega^\beta$ and $\partial_{ext}\Omega_m^{\beta,\varepsilon} \subset \partial\Omega^\beta$, such that

$$\partial_{ext}\Omega_m^{\beta,\varepsilon} = \partial\Omega_m^{\beta,\varepsilon} \setminus \Gamma_{mc}^{\beta,\varepsilon} = \partial\Omega_m^{\beta,\varepsilon} \cap \partial\Omega^\beta, \tag{82}$$

$$\partial_{ext}\Omega_c^{\beta,\varepsilon} = \partial\Omega_c^{\beta,\varepsilon} \setminus \Gamma_{mc}^{\beta,\varepsilon} = \partial\Omega_c^{\beta,\varepsilon} \cap \partial\Omega^\beta. \tag{83}$$

It should be noted that in our case the "canal" is represented by ellipsoidal lacuna so the name "canal" remains just for preserving the subscript c.

As was previously mentioned, we consider the pores between $\alpha-$ and $\beta-$ level mutually connected. In this case, the pressure $\bar{p}$ is evenly distributed through the fluid on both levels and can be characterized only by one scalar value.

In what follows, the coefficients related to upscaling from $\alpha-$level are labeled by superscript α. We consider loading by the volume-force field $\hat{\boldsymbol{f}}^\alpha = (1-\phi^\alpha)\boldsymbol{f}^\alpha$ acting on the matrix and mean surface traction $\bar{\boldsymbol{g}}$ on $\partial_{ext}\Omega_m^{\beta,\varepsilon}$. The pores $\Omega_c^{\beta,\varepsilon}$ are drained out through $\partial_{ext}\Omega_c^{\beta,\varepsilon}$. The total outflow from Ω^β is denoted as $J^{\beta,\varepsilon}$ and it incorporates also the flux from $\alpha-$level pores and from the $\beta-$level pores, [25]. Thus, we may introduce the problem description on the mesoscopic level using Eq.(79) and Eq.(79) with the addition of the flux from $\beta-$ level pores. The displacement $\boldsymbol{u}^{\beta,\varepsilon} \in \mathbf{H}^1(\Omega_m^{\beta,\varepsilon})$

and the pressure $\bar{p}^{\varepsilon} \in$ satisfy the equation

$$\int_{\Omega_m^{\beta,\varepsilon}} (\mathbb{A}^{\alpha} \nabla^S \mathbf{u}^{\beta,\varepsilon} - \bar{p}^{\varepsilon} \hat{\mathbf{B}}^{\alpha}) : \nabla^S \mathbf{v} + \bar{p}^{\varepsilon} \int_{\Gamma^{\beta,\varepsilon}} \mathbf{v}.\mathbf{n}^m dS_x = \int_{\partial_{ext}\Omega_m^{\beta,\varepsilon}} \bar{\mathbf{g}}^{\alpha}.\mathbf{v} dS_x + \int_{\Omega_m^{\beta,\varepsilon}} \hat{\mathbf{f}}^{\alpha}.\mathbf{v}, \quad \forall \mathbf{v} \in V(\Omega_m^{\beta,\varepsilon}) \tag{84}$$

and the volume conservation

$$\int_{\Omega_m^{\beta,\varepsilon}} (\hat{\mathbf{B}}^{\alpha} : \nabla^S \mathbf{u}^{\beta,\varepsilon} + \int_{\partial\Omega_c^{\beta,\varepsilon}} \tilde{\mathbf{u}}^{\beta,\varepsilon}.\mathbf{n}^c dS_x + \bar{p}^{\varepsilon}[(M^{\alpha}) + \gamma\bar{\phi}^{\alpha}|\Omega_m^{\beta,\varepsilon}| + \gamma|\Omega_c^{\beta,\varepsilon}|] = -J^{\beta,\varepsilon}, \tag{85}$$

where $\tilde{\boldsymbol{u}}^{\beta,\varepsilon}$ is the displacement extension to canals $\Omega_c^{\beta,\varepsilon}$.

4.5.1 Limit problem

In what follows, we pass from the problem described on Ω^{β} to the limit problem by the unfolding method. The approach is analogical to the $\alpha - level$.

The heterogeneities at the mesoscopic *beta*-level are represented by the RPC with an analogous decomposition as in the previous level

$$Y^{\beta} = Y_m^{\beta} \cup Y_c^{\beta} \cup \Gamma_{mc}^{\beta}, \quad Y_c^{\beta} = Y^{\beta} \setminus \bar{Y}_m^{\beta}, \quad \Gamma_{mc}^{\beta} = \bar{Y}_m^{\beta} \cap \bar{Y}_c^{\beta}. \tag{86}$$

and with the outer boundary,

$$\partial_{ext} Y_m^{\beta} = \partial Y_m^{\beta} \setminus \Gamma_{mc}^{\beta} = \partial Y_m^{\beta} \cap \partial Y^{\beta}, \tag{87}$$

$$\partial_{ext} Y_c^{\beta} = \partial Y_c^{\beta} \setminus \Gamma_{mc}^{\beta} = \partial Y_c^{\beta} \cap \partial Y^{\beta}. \tag{88}$$

.

In analogy to the problem on $\alpha-$level, we introduce the recovery sequences $\boldsymbol{u}^{R,\varepsilon}$ in the form given by the equation 51 and the testing functions $\boldsymbol{v}^{\varepsilon}$ with similar decomposition but both now associated with displacement the on $\beta-$level $\boldsymbol{u}^{\beta,\varepsilon}$. We consider the same convergences of $\boldsymbol{u}^{R,\varepsilon}$, $\boldsymbol{v}^{\varepsilon}$ and their gradient when applying the unfolding operator like for the $\alpha-$level homogenization. By substituting $\boldsymbol{u}^{R,\varepsilon}$, $\boldsymbol{v}^{\varepsilon}$ in the Eq.(84) and (85) and applying the unfolding operator, we can pass to the the limit model on the $\beta-$level by $\varepsilon \to 0$. Note that we deal with the interface integral with the help of Lemma 1. Now, we can introduce the limit two-scale problem in the form

$$\fint_{\Omega^\beta\times Y_m^\beta} (\nabla_x^S \boldsymbol{v}^0 + \nabla_y^S \boldsymbol{v}^1) : \left(\mathbb{A}^\alpha(\nabla_x^S \boldsymbol{u}^\beta + \nabla_y^S \boldsymbol{u}^{1,\beta}) - \bar{p}\hat{\boldsymbol{B}}^\alpha\right) - \bar{p}\int_{\Omega^\beta}\left(\phi^\beta \mathrm{div}_x \boldsymbol{v}^0 - \fint_{\Gamma_Y^\beta} \boldsymbol{v}^1\cdot\boldsymbol{n}^m \,\mathrm{dS}_y\right) =$$
$$= \int_{\partial\Omega^\beta} \overline{\boldsymbol{g}^\alpha}^\beta \bar{p}\cdot\boldsymbol{v}^0 \,\mathrm{dS}_x + \int_{\Omega^\beta}(1-\phi^\beta)\hat{\boldsymbol{f}}^\alpha\cdot\boldsymbol{v}^0 \,, \tag{89}$$
$$\fint_{\Omega^\beta\times Y_m^\beta} \hat{\boldsymbol{B}}^\alpha : (\nabla_x^S \boldsymbol{u}^\beta + \nabla_y^S \boldsymbol{u}^{1,\beta}) + \int_{\Omega^\beta}\left(\phi^\beta \mathrm{div}_x \boldsymbol{u}^\beta - \fint_{\Gamma_Y^\beta} \boldsymbol{u}^{1,\beta}\cdot\boldsymbol{n}^m \,\mathrm{dS}_y\right) + \bar{p}|\Omega^\beta|[\hat{M}^\alpha(1-\phi^\beta) + \gamma\phi^\beta] =$$
$$= -\boldsymbol{J}^\beta \,,$$

for all $\boldsymbol{v}^0 \in \mathbf{H}^1(\Omega^\beta), \boldsymbol{v}^1 \in L^2(\Omega^\beta; \mathbf{H}^1_\#(Y_m^\beta))$, where ($\boldsymbol{n}$ is the unit outward normal on $\partial\Omega^\beta$)

$$\overline{\boldsymbol{g}}^\beta(p) = (1-\phi_S^\beta)\boldsymbol{g} - p\boldsymbol{n}\phi_S^\beta \,. \tag{90}$$

4.5.2 Local problem

The local problem is relevant on the domain Y^β and can be derived by a similar procedure as was used on the $\alpha-$level. We chose test function $\boldsymbol{v}^1(\boldsymbol{x},\boldsymbol{y}) = \boldsymbol{w}(\boldsymbol{y})\theta(\boldsymbol{x})$, all other components vanish. By using the transform vector $\boldsymbol{\Pi}^{ij}$,the local problem is written as follows: Find $\boldsymbol{u}^{1,\beta} \in \mathbf{H}^1_\#(Y^\beta)$ satisfying

$$\fint_{Y_m^\beta}\left[\nabla_y^S \boldsymbol{w} : \left(\mathbb{A}^\alpha \nabla_y^s(\boldsymbol{\Pi}^{ij}\partial_j^x u_i + \boldsymbol{u}^{1,\beta}) - \bar{p}\hat{\boldsymbol{B}}^\alpha\right)\right]$$
$$+\bar{p}\fint_{\Gamma_Y^\beta} \boldsymbol{w}\cdot\boldsymbol{n}^m \,\mathrm{dS}_y = 0 \tag{91}$$

4.5.3 Homogenized problem

The "vanishing" of ε leads to equations involving effective poroelastic properties of the $\beta-$level, which can be evaluated using the characteristic responses (or corrector functions) $\boldsymbol{\omega}_\beta^{ij}$ and $\boldsymbol{\omega}_\beta^P$. The corrector functions of the $\beta-$level can be found as a solution of the following problem: Find $\boldsymbol{\omega}_\beta^{ij} \in \mathbf{H}^1_\#(Y_m^\beta)$ and $\boldsymbol{\omega}_\beta^P \in \mathbf{H}^1_\#(Y_m^\beta)$ satisfying

$$\int_{Y_m^\beta}[\mathbb{A}^\alpha \nabla_y^S(\boldsymbol{\omega}_\beta^{ij} + \boldsymbol{\Pi}^{ij})] : \nabla_y^S \mathbf{v} \;=\; 0, \tag{92}$$

$$\int_{Y_m^\beta} [\mathbb{A}^\alpha \nabla_y^S \boldsymbol{\omega}_\beta^P] : \nabla_y^S \mathbf{v} \;=\; -\int_{Y_m^\beta} \hat{\mathbf{B}}^\alpha : \nabla_y^S \mathbf{v} + \int_{\Gamma_Y^\beta} \mathbf{v}.\mathbf{n}^m dS_y, \tag{93}$$

for all $\boldsymbol{v} \in \mathbf{H}^1_{\#}(Y_m^\beta)$.

While the solutions $\boldsymbol{\omega}_\beta^{ij}$ express fluctuations with respect to the unit strain of the macroscopic scale, the $\boldsymbol{\omega}_\beta^P$ interpret the local response with respect to the unit pressure, [25].

Using the corrector functions, we can evaluate the effective poroelasticity properties given by the following coefficients

$$A^\beta_{ijkl} = \fint_{Y_m^\beta} [\mathbb{A}^\alpha \nabla_y^S (\boldsymbol{\omega}_\beta^{kl} + \boldsymbol{\Pi}^{kl})] : \nabla_y^S \mathbf{v}(\boldsymbol{\omega}_\beta^{ij} + \boldsymbol{\Pi}^{ij}) \tag{94}$$

$$B^\beta_{ij} = \fint_{Y_m^\beta} \hat{\mathbf{B}}^\alpha : \nabla_y^S \mathbf{v}(\boldsymbol{\omega}_\beta^{ij} + \boldsymbol{\Pi}^{ij}) - \fint_{Y_m^\beta} \mathrm{div}_y \boldsymbol{\omega}_\beta^{ij} \tag{95}$$

$$M^\beta = \fint_{Y_m^\beta} [\mathbb{A}^\alpha \nabla_y^S (\boldsymbol{\omega}_\beta^p)] : \nabla_y^S \mathbf{v}(\boldsymbol{\omega}_\beta^p) \tag{96}$$

The response of the homogenized medium at the macroscopic scale is described by the displacement $\mathbf{u}$ and by the pressure $\bar{p}$ satisfying

$$\int_{\Omega^\beta} (\mathbb{A}^\beta \nabla_x^S \mathbf{u} - \bar{p}\hat{\mathbf{B}}^\beta) : \nabla_x^S \mathbf{v} \;=\; \int_{\Omega^\beta} (1-\phi^\beta)\mathbf{f}^\alpha.\mathbf{v} + \int_{\partial\Omega^\beta} \bar{\mathbf{g}}^\beta.\mathbf{v} dS_x \quad \forall V(\Omega) \tag{97}$$

$$\int_{\Omega^\beta} \hat{\mathbf{B}}^\beta \nabla_x^S \mathbf{u} + \bar{p}\hat{M}^\beta |\Omega^\beta| \;=\; -J^\beta, \tag{98}$$

for all $\boldsymbol{v} \in \mathbf{H}^1(\Omega^\beta)$, where $\bar{\boldsymbol{g}}^\beta := (1-\phi^\beta)\bar{\boldsymbol{g}}^\alpha + \phi^\beta(-\bar{p})\boldsymbol{n}$ is the mean surface stress and $\bar{\phi}^\beta$ is the mean $\beta-$level porosity. Further, we introduce

$$\hat{\mathbf{B}}^\beta := \mathbf{B}^\beta + \phi^\beta \mathbf{I}, \quad \hat{M}^\beta := M^\beta + \gamma\bar{\phi}^\beta + (M^\alpha + \gamma\bar{\phi}^\alpha)(1-\bar{\phi}^\beta)\,. \tag{99}$$

With this, we have a complete set of equations for obtaining the poroelastic properties of one single osteon in cortical bone tissue. The effective coefficients can be used for further applications and can be also associated with the Biot poroelasticity model, from which the increase of fluid content J^β can be computed.

4.6 Relevance to the Biot poroelasticity model

The model describing behavior of the poroelastic material was firstly introduced by Belgian-American physicist Maurice Anthony Biot (1905 - 1985). His name was used for the effective poroelastic coefficients derived in the previous text, because those are relevant to his poroelastic model. In this place, we would like to discuss the relationship between our model and the Biot model. Biot formulated the poroelastic model in the following form

$$\boldsymbol{\sigma} = \mathbb{D}^{eff}\boldsymbol{e} - \boldsymbol{\alpha}p, \tag{100}$$

$$\zeta = \boldsymbol{\alpha} : \boldsymbol{e} + \frac{1}{\mu}(p - p_0), \tag{101}$$

where $\boldsymbol{\sigma} = (\sigma_{ij})$ is the total stress, p is the fluid pressure, $p_0 = 0$ is the reference pressure, $\boldsymbol{e} = (e_{ij})$ is the strain tensor and ζ is the fluid content per unit volume increase, which is in our model represented by J. After comparing the macroscopic problem formulation Eq.(97) and (98) with the Biot model Eq.(100) and (101), we noticed the following relationships between coefficients (note that we no more use the superscript β)

$$\mathbb{D}^{eff} = \mathbb{A}, \qquad \boldsymbol{\alpha} = \hat{\mathbf{B}}, \qquad \frac{1}{\mu} = \hat{M}. \tag{102}$$

Thus, the Biot model with our effective coefficients transform into notation

$$\boldsymbol{\sigma} = \mathbb{A}\boldsymbol{e} - \hat{\mathbf{B}}p, \tag{103}$$

$$\zeta = \hat{\mathbf{B}} : \boldsymbol{e} + \hat{M}(p - p_0). \tag{104}$$

It is evident, that instead of the weak formulation of the macroscopic problem Eq.(97) and (98), it can be convenient to use the analogical Biot model for the computation of the matrix deformation $\boldsymbol{e}$ and the fluid pressure p. Those two can be found as the solution of the inverse relationship to the Eq.(103) and (104)

$$\boldsymbol{e} = \mathbb{C}\boldsymbol{\sigma} + \mathbf{S}\zeta, \tag{105}$$

$$p = -\mathbf{S} : \boldsymbol{\sigma} + K\zeta, \tag{106}$$

where $\mathbb{C}$ is the fourth-order compliance tensor of the bulk material observed in an undrained loading, $\mathbf{S}$ is the Skempton tensor and $K^{-1}\mathbf{S} : \boldsymbol{\sigma}$ expresses the fluid content increase for drained loading. Between the coefficients of Eq.(103), (104) and Eq.(105),(106) there are the following relations

$$\mathbb{C} = \hat{M}\mathbb{D}\mathbb{A}^{-1}, \tag{107}$$

$$\mathbf{S} = \mathbb{D}\mathbb{A}^{-1} : \hat{\mathbf{B}}, \tag{108}$$

$$K = \frac{1}{\hat{M}}(1 - \hat{\mathbf{B}} : \mathbb{D}\mathbb{A}^{-1} : \hat{\mathbf{B}}), \tag{109}$$

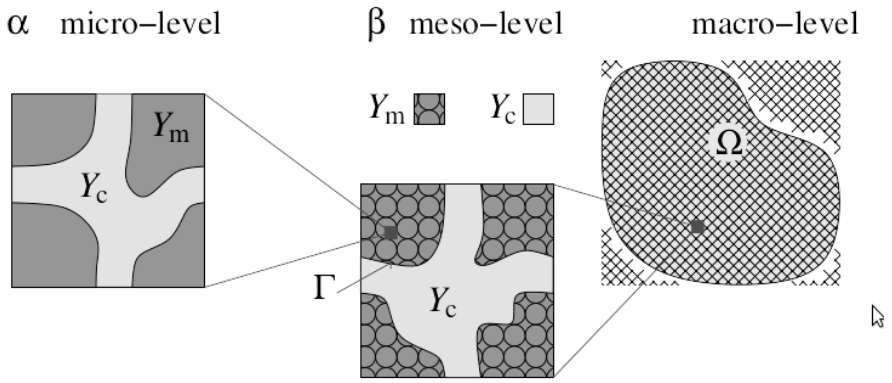

Figure 7: The two-level heterogeneous structure: α-level is formed by a single connected porosity Y_c^α ; the α matrix Y_m is formed by the solid. At the β-level, the homogenized structure of the α-level forms the β material situated in the matrix Y_m, source [5]

where $\mathbb{D} = \left[\hat{M}\mathbb{I} + \mathbb{A}^{-1}(\hat{\mathbf{B}} \otimes \hat{\mathbf{B}})\right]^{-1}$ is symmetric tensor, thus the compliance tensor $\mathbb{C}$ is also symmetric.

In this section, the information stated in [25] was used.

4.7 Homogenization process summary

In the previous text a model based on two-level homogenization with a periodic structure ansatz applied at each level was proposed, to obtain the material properties of the bone osteon matrix. Let us summarize the homogenization process on two levels.

- $\alpha-$level - upscaling from the canalicular porosity level to obtain the material model describing effective behavior relevant at the β-level of heterogeneity. The bone matrix is constituted by a solid perforated by canaliculi.
- $\beta-$level - upscaling from the lacunar-canalicular porosity level to obtain the material model describing the effective behavior at the level of osteons. The heterogeneous structure is formed by the poroelastic matrix with connected porosity (the canaliculi) drained in the ellipsoidal fractures representing lacunae.

The decomposition of the whole material is illustrated by Fig. 7.

4.8 Model parameters

In following sections we focus on determination of the main parameters which are necessary for evaluating the model of two-scale homogenization defined in the previous section. We also introduce the literature research of relevant geometric and material parameters and in the end we

introduce the geometry suitable to the cortical bone modeling. In what follows we preserve the manuscripts α and β referring to the microscopic and mesoscopic structure, respectively.

4.8.1 Mechanical properties

In our study, the cortical bone tissue is considered to be a poroelastic medium with two porosity scales. In the previous section we explained the upscaling process from micro- to mesoscale and from mesoscale to macroscale, in order to obtain the effective coefficients which describe the material on the macroscale. However, for this upscaling process, we have to know the material properties on the lowest scale represented by the $\alpha-$level. When we look at the problem formulated on the microscopic scale level given by Eq.(43) and (44), we see that the material of the $\alpha-$level matrix represented by domain $\Omega_m^{\alpha,\varepsilon}$ is characterized by the stiffness tensor $\mathbb{D}^{\alpha,\varepsilon}$. We assume the isotropic material on the $\alpha-$level, thus the stiffness tensor is given by the Young's modulus E and the Poisson's ration ν, see Eq.(5) and (6). On the other hand, the fluid is considered a compressible Newtonian, thus it is characterized by $\alpha-$level fluid compression γ^α defined by Eq.(12). Thus, we may say that the material properties for the matrix and for the fluid, which we need to prescribe to the poroelasticity model,are E, ν and γ.

In the following text we search through the literature for the material properties suitable to our model.

4.8.2 Literature survey of cortical bone material parameters

For further use, we need to specify the elastic material constants of the matrix on micro-level, i.e. the level of canalicular porosity. Thus, we introduce a short literature research of papers focused on the cortical bone and the material coefficients determination.

The material parameters of the cortical bone tissue are the objective of many studies with a wide range of methods used for their determination. First we have to look into the [21], where a similar literature research was made. According to [21], through literature can be found Young's moduli of the cortical bone material in range from 1 to 20 GPa depending on the method or specimen size and orientation, but there is not clearly stated the estimate of the Poisson's ratio. The results of the survey from [21] are summarized in Tab.2, where the secondary references are listed.

Reference	type of loading	E (GPa)
Ascenzi et al.(1967)	tension	12
Ascenzi et al.(1968)	Compression	6
Ascenzi et al.(1990)	bending	2
Ascenzi et al.(1994)	torsion	20

Table 2: Summarization of literature survey of single osteon material properties, [21]

In [30] is used nanoindentation and acoustic measurement for the estimation of elastic properties of the cortical bone tissue. For the acoustic measurement were used the following values of the Poisson's ratio, $\nu_{12} = 0.376, \nu_{21} = 0.422, \nu_{13} = 0.222, \nu_{31} = 0.371, \nu_{23} = 0.235, \nu_{32} = 0.35$. For the nanoindentation was estimated the Poisson's ration $\nu = 0.3$. Results of both methods are shown in Tab.3.

Direction	E (GPa) (acoustic)	E (GPa) (nanoindentation)
transverse	14.91 ± 0.52	16.58 ± 0.32
longitudinal	20.55 ± 0.21	23.45 ± 0.21
average	17.73 ± 0.22	20.02 ± 0.27

Table 3: Estimation of Young's moduli using acoustic method and nanoindentation, [30]

	Drained elastic constant (GPa,-)	Drained elastic constant (GPa,-) for isotropic matrix
E_1^d	15.7	18.2
E_2^d	18.0	18.0
E_3^d	21.7	18.2
ν_{12}^d	0.330	0.306
ν_{13}^d	0.239	0.300
ν_{21}^d	0.379	0.301
ν_{23}^d	0.348	0.302
ν_{31}^d	0.330	0.300
ν_{32}^d	0.298	0.306

Table 4: Drained elastic constant at the canaliculi porosity level, [32]

In [32] the elastic constants (drained and undrained) were calculated for the canalicular porosity level, when canaliculi are aligned in longitudinal, radial and circumferential direction. In Tab.4 are shown the average values from those three directions.

4.9 Geometric parameters

For our model, the most crucial geometric parameters are the dimensions and directions of canaliculi and lacunae, which influence the $\alpha-$ and $\beta-$ level porosity, respectively. But there are other parameters such as the number of canaliculi in each direction or the distance between lacunae, which are also important for describing the geometry representing the microstructure of our model. In this section we introduce the main geometric parameters of our model and focus on the literature survey for estimating their values.

4.9.1 Lacunae

First, we focus on the lacunae, which are relevant to the $\beta-$level structure of our model. The lacunae are approximately ellipsoids containing one osteocyte, [32]. We can define the shape of lacunae as a triaxial ellipsoid with the Cartesian equation for a general ellipsoid

$$\left(\frac{x}{a_0}\right)^2 + \left(\frac{y}{b_0}\right)^2 + \left(\frac{z}{c_0}\right)^2 = 1, \tag{110}$$

where the lacunar semi-axes a_0, b_0, c_0 determine the size of lacunae.

In [1] are the semi-axes determined approximately $a_0 = 10\mu m, b_0 = 25\mu m, c_0 = 5\mu m$.

In [8] over 10.000 osteocyte lacunae were measured by micro-CT. By this method was determined the mean long axis length as $8.96\mu m$ and the mean volume $290\mu m$. If we consider the two shortest axes having the same length, we can calculate all semi-axes from the equation of ellipsoidal volume.

One of the most recent work, [3], presents a micro-CT study of lacunar morphology and density in human femur. In this study were measured and determined the values for lacunar volume, canal diameter, and also the parameters defining shape of lacunar ellipsoid, eigenvalue (EV) of axis of ellipsoid, elongation, equancy and flatness. Note that the lengths of semi-axes equal to the square root of the corresponding eigenvalues. The measured values are shown in Tab.5.

Region	average lacunar volume (μm^3)	EV1	EV2	EV3
AP	389 ± 40	16.75 ± 1.21	3.87 ± 0.26	1.70 ± 0.14
ML	408 ± 53	14.13 ± 1.37	4.46 ± 0.59	1.78 ± 0.14

Table 5: Morphological parameters of osteocyte lacuna, AP - combined anterior + posterior, ML - combined medial + lateral

In [31] are measured the parameters of a single osteocyte in adult mouse fibulae and calvarie, which are shown in Tab.6. Note, that morphological parameters of lacunae can be approximated by parameters of osteocyte.

	Length(μm)	Width(μm)	Height(μm)	Ratio l:w:h
Fibula	28.74 ± 4.67	7.60 ± 1.15	5.03 ± 0.90	5.9:1.5:1
Calvaria	13.22 ± 1.47	8.07 ± 0.51	6.56 ± 0.64	2.1:1.3:1

Table 6: Morphological parameters of a single osteocyte in adult mouse fibulae and calvaria,[31]

For our purpose, the most relevant and proper seems to be the semi-axes length estimation from [1].

The size of lacunae is a crucial parameter for the determination of the $\beta-$level porosity, but so is the density of lacunae in the cortical bone tissue. The density of lacunae can be characterized

by the distance from one lacunae to another. In [1], the center-to-center length L between lacunae was determined for the human cortical bone as $43\mu m$.

Measuring the length from lacunae to the nearest lacunae by micro-CT presented in [8] gave the result $21.8\mu m$.

4.9.2 Canaliculi

Let us focus on the geometric parameters determining the size and direction of canaliculi. As was previously stated, canaliculi are small tunnels that connect the osteonal canal to lacunae a lacunae to other lacunae. Thus, we imagine them as cylindrical cavities in a matrix. According to [32] the diameter of the canaliculi can differ from $200nm$ to $400nm$. In [1] was specified the radius of canaliculi in the range of $80 - 710nm$ with an average radius of $129.5nm$ using experimental measurement, while in [33] the radius was estimated in range of $40 - 355nm$ with average value of $259 \pm 129nm$. The diameter of the canaliculi of the cortical bone in lamellar region was in [29] stated as $553 \pm 33nm$.

Now we have the information about the diameter of one canaliculi, but we do not know anything about their number. One lacunae is connected with others and with the osteonal canal by a high number of canaliculi, which differs in each direction. To determine this number, we followed the approach from [1]. This approach used the surface area method, where from the number of canaliculi per lacunae $N.Ca$ and the planar projection of lacunae the number of canaliculi in each direction is computed. This approach will be mentioned later. Note, that the number of canaliculi in each direction depends through the lacunar planar projection on the size of lacunae, i.e. on the semi-axes a_0, b_0, c_0. For this approach, it is also vital to determine the number of canaliculi per lacunae $N.Ca$. This number was also computed in [1] for six species using two different approaches, the slicing method and the surface method. For the human bone, the low estimate was determined using the slicing method as 18 and high estimate as 116 canaliculi per lacunae. With the surface method, the number of canaliculi was estimated as 41.

4.10 Geometry for the model

With the knowledge of the cortical bone microstructure and from the literature survey made in the previous section, we have all tools we need to introduce the geometries representing the RPC on both levels. First, we introduce the geometry on $\beta-$level, which proves to be more effective to describe the geometry on the lower level. For both geometry creation and meshing was used the software *GMSH*. In the case of our model, when the periodic structure is considered, the generated mesh must also be periodic.

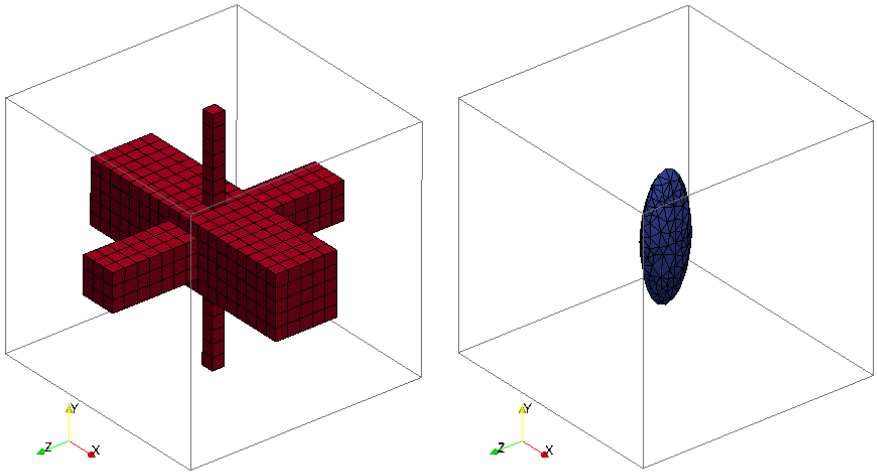

(a) $\alpha-$level geometry (b) $\beta-$level geometry

Figure 8: Geometry used for two-scale homogenization

4.10.1 Geometry representing the $\beta-$level

The $\beta-$level geometry should represent lacunae in a matrix characterized by elastic properties obtained by the homogenization on the lower level. The periodicity of the structure is described by representative cubic cell Y^{β}. For the length of the cubic side we use the characteristic length $L_{\beta}\mu m$ as stated in [1]. The lacunae is represented by an ellipsoid, placed in the center of the cube, given by Eq.(110) with semi-axes a_0, b_0, c_0, which determine the size of the lacunae. We choose the length of semi-axes from [1]. Our choice of values for all the parameters is based on the literature survey and can be found in Tab.7. The resulting geometry can be seen on Fig.8b. Now we can focus on the lower level.

4.10.2 Geometry representing the $\alpha-$level

The periodicity on this level is also represented by a cubic cell Y^{α} with a characteristic length $L_{\alpha} = 43\mu m$. The porosity is caused by canaliculi whose number differs in X, Y and Z directions. Instead modeling each small canaliculi, we approximate them by three bigger canals with square cross-sectional area corresponding to sum of cross-sectional areas of all the canaliculi in the given direction. For this approximation we need to determine the number of canaliculi in each direction. As was mentioned in text above, we followed the approach from [1]. Using the number of canaliculi per lacuna $N.Ca$, projected surface areas for the osteocyte lacunar ellipsoid in the X-Z, X-Y and Y-Z planes $PSA_{xz}, PSA_{xy}, PSA_{yz}$ and their sum T_{PSA}, we can determine the number of canaliculi in X, Y and Z direction n_x, n_y, n_z,. On the alpha level we have to calculate the number of canaliculi in

each direction from Eq.(111).

$$n_i = \frac{PSA_{jk}}{2T_{PSA}} N.Ca, \quad i, j, k = x, y, z. \tag{111}$$

From the Eq.(111) it is clear, that the size of lacunae determined by semi-axes a_0, b_0, c_0 is necessary for the determination of the number of canaliculi in each direction. The chosen values of all of the introduced geometry parameters are listed in Tab.7. The resulting geometry can bee seen on Fig.8a.

Symbol	Parameter	Unit	Value for $\alpha-$level	Value for $\beta-$level
L	characteristic length of RPC	μm	4.3	43
r_x	diameter of canaliculi in x-direction	μm	0.6	-
r_y	diameter of canaliculi in y-direction	μm	0.6	-
r_z	diameter of canaliculi in z-direction	μm	0.6	-
a_0	semi-axis of ellipsoid in x-direction	μm	-	2.5
b_0	semi-axis of ellipsoid in y-direction	μm	-	12.5
c_0	semi-axis of ellipsoid in z-direction	μm	-	5.0
$N.Ca$	number of canaliculi per lacunae	-	106	-

Table 7: Geometry parameters for $\alpha-$level and $\beta-$level

4.10.3 Geometry representing macroscopic level

The macroscopic level should represent one single bone osteon. As was stated in section 2.1.4, the osteon is approximately cylindrical structure with a hollow canal in its center. The radius of its cylindrical body is roughly $100 - 150\mu m$, [32]. The radius of the osteonal canal is approximately $20\mu m$, [6]. Note that these values are highly approximate because of large differences between the dimensions of each osteon. The resulting geometry used for the macroscopic model is pictured on the Fig. 9.

4.11 Numerical results

In this section we introduce the numerical results of effective poroelastic properties obtained by the two-scale homogenization. The mathematical model introduced in the previous chapter was implemented in the software *SfePy*. For the better understanding of influence of porosity, we performed the parameter study of the implemented model.

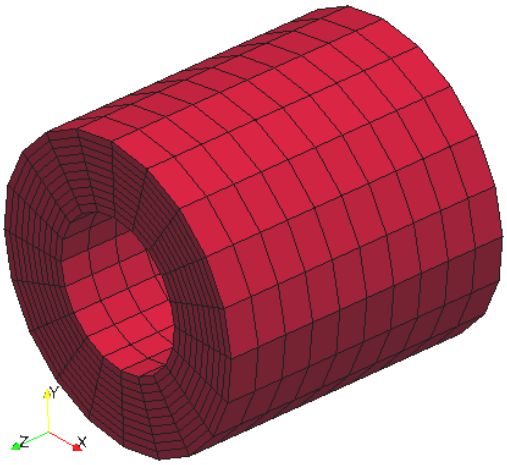

Figure 9: Geometry on the macroscopic level, diameter 2 cm, height 2 cm

4.11.1 Problem implementation

We implemented the two-scale homogenization problem in the software *SfePy* developed on the Department of Mechanics, Faculty of applied sciences, University of West Bohemia. *SfePy* is based on the finite elements method and represents a strong tool for solving the systems of PDE and also for homogenization. Thus, it is ideal software for solving the previously defined mathematical model. For more detailed informations about this software development and documentation we recommend visiting the site *http://sfepy.org*.

4.11.2 Problem on the $\alpha-$level

In this section we focus on the microscopic scale homogenization in order to obtain the effective coefficients relevant to the mesoscopic scale. Thus, we solve the following homogenization problem in three dimensional space.

The microstructure is represented by RPC Y^α with geometry defined in the previous section, see Fig.8a. On this level, we consider the matrix as an isotropic material. Let us remind, that by periodically repeating the RPC Y^α, the matrix of the mesoscopic level should be generated. Each face of cell should touch the side of its neighbor without a gap and each cell should be exactly the same as the other. Thus, the values of the corrector functions $\boldsymbol{\omega}^p$ and $\boldsymbol{\omega}^{ij}$ are the same in the opposite faces of the cube; we need to prescribe them the periodical boundary conditions. Further, we consider the case, where the correctors are zero in the RPC Y^α corners. By this, we completed the boundary condition.

First, in order to obtain the effective coefficient, we have to compute the corrector functions

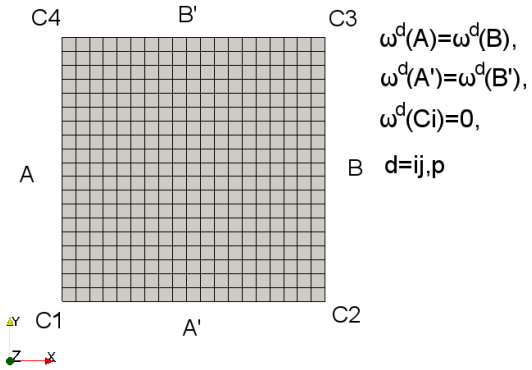

Figure 10: Boundary conditions for the homogenization problems on microscopic and mesoscopic level

$\boldsymbol{\omega}^p$ and $\boldsymbol{\omega}^{ij}$ satisfying the Eq.(72), with the boundary conditions

$$\boldsymbol{\omega}^d(A) = \boldsymbol{\omega}^d(B), \tag{112}$$

$$\boldsymbol{\omega}^d(C) = \bar{0}, \quad d = p, ij \tag{113}$$

where A and B represent the opposing faces and C the corners of the cubic RPC Y^α, see Fig.10. The transformation vector is obtained from the dimension of Y^α geometry.

With the knowledge of the corrector functions, the homogenized coefficient are obtained by solving Eq.(75)-(78). Those coefficients refer to the mesoscopic level properties and are used for upscaling to the macroscopic level.

4.11.3 Problem on the $\beta-$level

We use the $\beta-$level geometry for describing the RPC Y^β; the geometry can be seen on Fig.8b. For this level we need to compute new corrector functions from Eq.(92),(93). Note, that the symbols $\boldsymbol{\omega}^p$ and $\boldsymbol{\omega}^{ij}$ now refer to the correctors on $\beta-$level. These equations should be completed by boundary conditions.

Similarly to the previous level, we consider the matrix of the macroscopic level to be generated by periodically repeated Y^β. Thus, the boundary conditions are also similar, given by Eq.(112) and (112), with the same reasoning as in the previous level. For this level, we use the effective coefficient obtained by $\alpha-$level upscaling. After we solve the corrector functions problem, we can evaluate the effective coefficients from Eq.(94)-(96).

4.11.4 Identification of material parameters

In this section we introduce the homogenized coefficients obtained by two-level homogenization. We solve the problem described in the text above. The input arguments of our model are Young's

modulus E^α, Poisson's ration ν^α and fluid compressibility γ^α, which represent the material (matrix and fluid) properties on $\alpha-$level. Our choice of their value is based on the literature survey and can be found in Tab.8.

Parameter	Symbol	Value	Unit
Young's modulus	E^α	18.0	GPa
Poisson's ratio	ν^α	0.3	-
Fluid compressibility	γ^α	0.9	GPa^{-1}

Table 8: Input parameters of model

With the assumption of an isotropic matrix on $\alpha-$level we can obtain the stiffness tensor from Young's modulus and Poisson's ratio. This tensor is necessary for the bilinear form defined by Eq.(74) and thus also for effective coefficients evaluation.

4.11.5 Effective coefficients

When performing the homogenization of the previously introduced problem, we obtain the effective stiffness tensor, Biot coefficient and Biot modulus relevant to macroscopic scale

$$\mathbb{D} = \begin{bmatrix} 1.676 \cdot 10^{1} & 6.312 \cdot 10^{0} & 5.602 \cdot 10^{0} & 1.929 \cdot 10^{-4} & -1.119 \cdot 10^{-4} & -1.641 \cdot 10^{-4} \\ 6.312 \cdot 10^{0} & 1.680 \cdot 10^{1} & 5.600 \cdot 10^{0} & 1.792 \cdot 10^{-4} & -1.543 \cdot 10^{-4} & 1.077 \cdot 10^{-5} \\ 5.602 \cdot 10^{0} & 5.600 \cdot 10^{0} & 1.545 \cdot 10^{1} & 1.929 \cdot 10^{-5} & -4.613 \cdot 10^{-4} & 1.944 \cdot 10^{-5} \\ 1.929 \cdot 10^{-4} & 1.790 \cdot 10^{-4} & 1.915 \cdot 10^{-5} & 5.291 \cdot 10^{0} & 2.169 \cdot 10^{-6} & -7.841 \cdot 10^{-5} \\ -1.122 \cdot 10^{-4} & -1.748 \cdot 10^{-4} & -4.799 \cdot 10^{-4} & 2.307 \cdot 10^{-6} & 4.463 \cdot 10^{0} & 1.825 \cdot 10^{-4} \\ -1.641 \cdot 10^{-4} & 9.343 \cdot 10^{-6} & 1.816 \cdot 10^{-5} & -7.839 \cdot 10^{-5} & 1.839 \cdot 10^{-4} & 4.463 \cdot 10^{0} \end{bmatrix}$$

$$\begin{aligned} \mathbf{B} &= \left[1.0904 \cdot 10^{0}, 1.0907 \cdot 10^{0}, 1.1301 \cdot 10^{0}, -1.3408 \cdot 10^{-5}, -5.2842 \cdot 10^{-6}, 1.0126 \cdot 10^{-7}\right] \\ M &= 1.5382 \cdot 10^{-4} \end{aligned}$$

From the form of the stiffness tensor, we can tell that the cortical bone tissue can be really describe by the orthotropic material. From the orthotropic material assumption we know, that from such stiffness tensor, the effective Young's modulus E_i^{macro}, Poisson's ration ν_{ij}^{macro} and shear modulus $G_i^{macro}, i, j = 1, 2, 3$, can be evaluated. In Tab.9, the computed effective material constant relevant to mesoscopic and macroscopic level can be found together with porosity on both, $\alpha-$ and $\beta-$level.

ϕ_α	ϕ_β	Parameter	Value on α	Value on β	Unit
0.127572	0.00563524	E_1	15.1464	13.4926	GPa
		E_2	12.9624	13.5258	GPa
		E_3	12.9624	12.7349	GPa
		ν_{12}	0.292738	0.289905	-
		ν_{13}	0.292738	0.257480	-
		ν_{21}	0.250527	0.290617	-
		ν_{23}	0.239264	0.257090	-
		ν_{31}	0.250527	0.243021	-
		ν_{32}	0.239264	0.242058	-
		G_1	5.10269	5.29164	GPa
		G_2	5.10269	4.46326	GPa
		G_3	4.01636	4.46301	GPa

Table 9: Effective material constant relevant to mesoscopic and macroscopic level

4.11.6 Parameter study

From the numerical results of effective material constant, we can see, that the isotropic material of the $\alpha-$level matrix changes by upscaling to an orthotropic material. The main parameter, which has influence on the upscaling is the porosity of the medium, which is computed as a volume fraction of pores in the whole geometry volume. Thus, the porosity can rise or decrease depending on the change of parameters defining pores geometry.

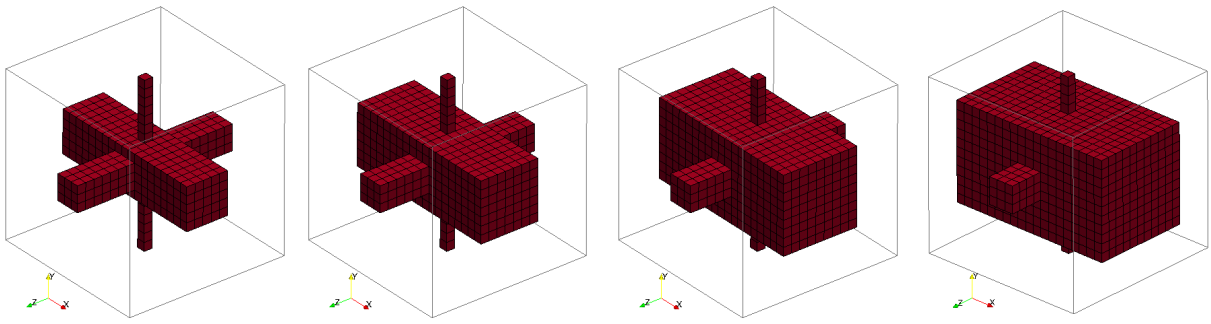

(a) rx=600nm (b) rx=800nm (c) rx=1000nm (d) rx=1200nm

Figure 11: Illustration of structure orientation

In what follows, we perform a parameter study; the porosity on $\alpha-$level is changed by increasing the x-direction canaliculi diameter r_x. The y-direction and z-direction are kept constant, thus the structure on the $alpha-$level is getting oriented in x-axis direction. Logically, this causes a change of the poroelastic properties on the macroscopic level. We study the dependency of Young's

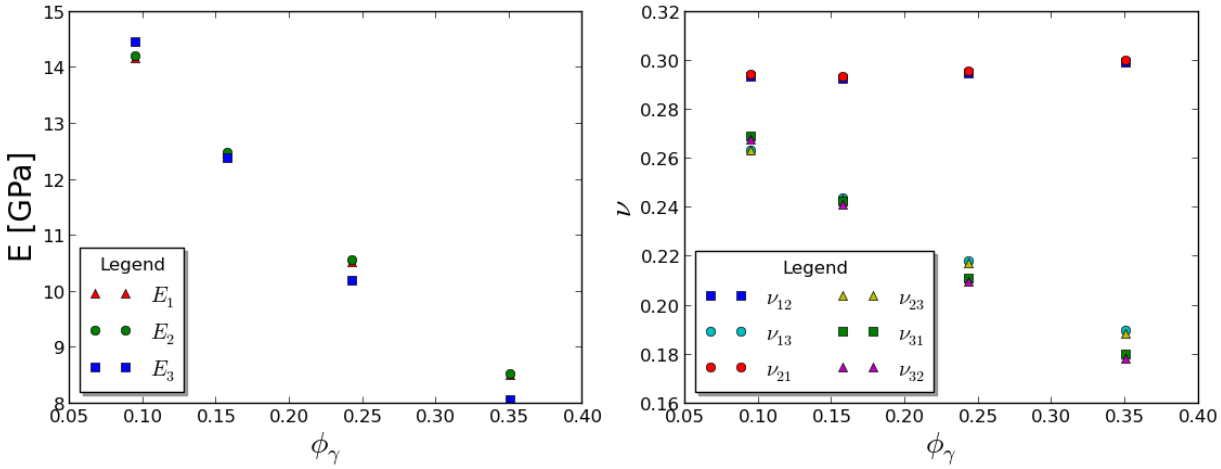

Figure 12: Dependency of Young's modulus and Poisson's ratio on the porosity ϕ_γ

modulus and Poisson ration on ϕ_γ porosity, where ϕ_γ depends on both level porosities see Eq.(2). It can bee seen that using the isotropic material considered at the microscopic level, an orthotropic material has been obtained on the macroscopic level, whose anisotropy increases with the change of porosity. The results of effective Young's modulus and Poisson's ration dependency on change of ϕ_γ porosity caused by varying r_x between $600 - 1200$ *nm* are shown in Fig.12.

Looking on the Fig.12, we notice that for the first geometry with the smallest value of porosity ϕ_γ the E_3 value is higher than E_1, E_2 but as porosity rises, E_3 is becoming smaller than the other two. This can be the effect of changing the cross-section area of the x-direction canal, which also changes the porosity in the other two directions. While the other canals have much smaller cross-section area, the change of porosity caused by the x-direction canal influences them highly. As the measure of anisotropy, we choose the ratio between the components of stiffness tensor C_{33}/C_{11}, see Fig.13.

4.11.7 Macroscopic problem solution

In this section, the effective coefficients computed by the two-level homogenization are used for solving the macroscopic problem defined by Eqs.(97) and (98). The macroscopic problem was also implemented in FE software *SfePy*. The macroscopic geometry is represented by a single osteon with z coordinate $z \in < 0, l >, l = 0.02$, see Fig. 9. For the macroscopic solution we apply zero force and add boundary conditions in

$$\begin{aligned} \boldsymbol{u}(x, y, 0) &= 0, \\ u_z(x, y, l) &= 10^{-4} \end{aligned} \tag{114}$$

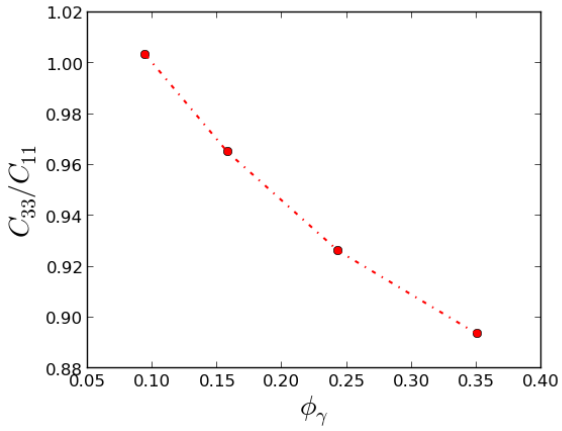

Figure 13: The change of material anisotropy due to the rise of the porosity ϕ_γ

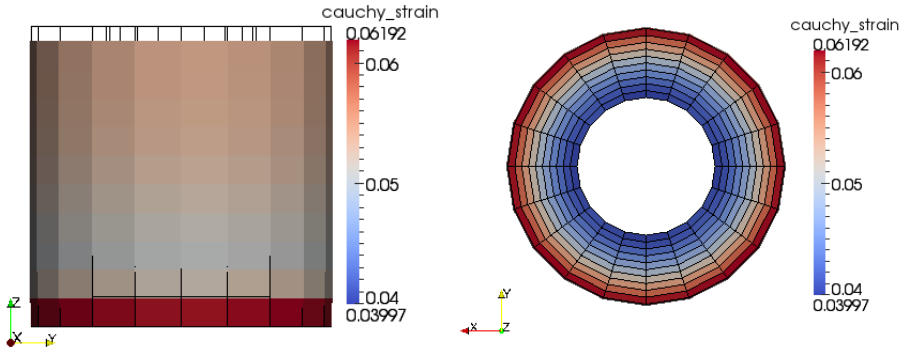

(a) (b)

Figure 14: Distribution of Cauchy's strain on deformed body

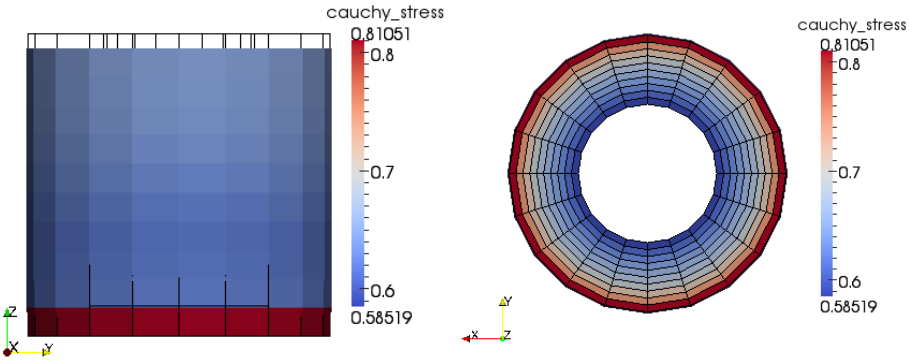

(a) (b)

Figure 15: Distribution of Cauchy's stress on deformed body

The distribution of Cauchy's strain on the deformed body is visualized in Fig.14, where the undeformed body is represented by the black wireframe. The distribution of Cauchy's stress can be found on the Fig.14. Let us say that the maximum values of Cauchy's stress and strain are placed on the expected parts of the deformed body. The scalar value of the pressure for this problem is computed as $p = 291.9880792071Pa$.

Further, we compare the effect of porosity on the deformation of the macroscopic body. We showed that with the rise of porosity the stiffness of the material decreases. while taking effective coefficient computed for the x-oriented $\alpha-$level geometries, Fig.12, we solve the macroscopic body deformation, while considering the boundary condition

$$\boldsymbol{u}(x, y, 0) = 0$$

Under applying the traction force $\boldsymbol{g} = [0, 0, -5]GPa$ on the plane $z = l$ we can compute the deformation of the macroscopic body with result shown in Fig.16. As was expected, the material with smaller porosity is stiffer and deforms much less then the one with larger pores.

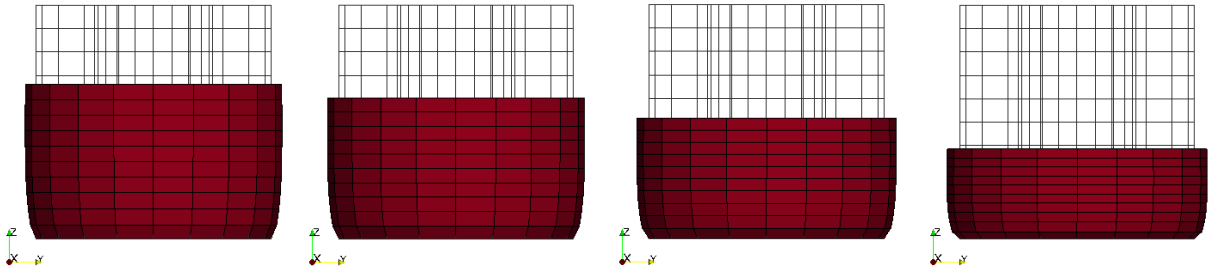

(a) $\phi_\gamma = 0.10$ (b) $\phi_\gamma = 0.15$ (c) $\phi_\gamma = 0.25$ (d) $\phi_\gamma = 0.35$

Figure 16: Deformation of the bodies with effective coefficients computed using α-level geometries with different cross-sections area. Note that the result i was computed with α-level geometry i visualized on the Fig.12, where $i = a, b, c, d$

5 Electro diffusion in porous structure of the cortical bone tissue

In the previous chapter, we focused mainly on the solid part of the cortical bone tissue structure and its mechanical properties. The response of the poroelastic body on loading was displacement and pressure in the fluid, while we neglected the electrochemical interaction in the two phases: solid and fluid. Thus, in this text we discuss the role of the fluid part in the bone tissue and the process of electro diffusion between the fluid and the solid matrix and explain the coupling with mechanical variables such as displacement. First, we introduce the main principles, which are necessary for understanding the problem. Later, the mathematical model of electro-diffusion in the porous structure of the cortical bone tissue will be introduced and then, by upscaling, the effective coefficients relevant to the macro-scale will be computed. Note that the notations in this chapter can differ from the previous text, thus in order to prevent confusion we recommend to look into the list of used variables.

5.1 Ionized fluid

In this section, we pay more attention to the fluid part. For the purpose of our model we imagine the bone fluid as a salt-water suspense. In the fluid part there are two types of ions with opposite polarization: the cations Na^+ and anions Cl^-.

We consider the fluid to be incompressible Newtonian, which seems to be in conflict with the assumption of compressibility from the poroelastic model where the compressible fluid assumption was reasonable because it allowed us to focus on the poroelastic problem as a steady state without the need of solving the fluid transport. On the other hand, while focusing on the fluid part, the assumption of the incompressibility leads to $\mathrm{div}\boldsymbol{w}_f = 0$, where $\boldsymbol{W}_f$ is fluid velocity. This assumption proves to be useful for derivation of the relation for convection-diffusion.

5.2 Material with one level of porosity

We consider the matrix to be a porous material with one level of porosity in contrary to the assumption of double-porous medium from the previous text. We focus on the porosity caused by canalicular network. Further, we consider that the matrix and also the solid-fluid interface present the negative charge, because of fatty acids and adsorbed species, [15], [14]. Under loading the bone matrix produces a small electrical charge, thus we consider the material with piezo-electrical behavior. All these characteristics of the matrix and their effects on the model will be discussed later.

5.3 Electro-mechanical relationship in porous media

We already presented the macroscopic model of poroelasticity, in which the mechanical loading leads to deformation of the porous medium. We consider the negatively charged surface of the pores, which are filled with the solution with electrolytes Na^+ and Cl^-. The negative potential is compensated by the adsorption of the cations on the surface forming the inner compact layer, known as the double layer.

The deformation of the solid medium affects also the fluid phase filling pores by causing it to flow. The ions in the fluid represent small charges and their movement through the net of pores leads to macroscopically observed electrokinetic phenomena called the streaming current. Moreover, to conserve charge, the movement of the charged ions generates the streaming electric potential, see [14].

The deformation of the porous matrix can affect the ion movement and distribution also in another way. The bone matrix is known for its piezoelectric behavior. Thus, when subjected to loading resulting in deformation, the matrix produces an electric charge, [16], which of course influences the ion movement and distribution. When the ions are in the electric field, the attraction / repulsion start to take effect. Thus, the ions start to move while pulling the fluid with them causing the electro-osmotic flow opposing the pressure gradient flow, [14].

In the following text, we focus on the electro-osmosis in the porous piezoelectric medium.

5.4 Potential distribution on the surface

We consider a solid body with a flat surface with its normal vector oriented into the fluid. In this fluid, ions with both ± electrical charges are randomly distributed. The permitivity of the solid part is denoted $\epsilon_M = \infty$ and the permitivity of the fluid ϵ_F has its bulk value. It is commonly known that ions with opposite signs of electrical charge are attracted to each other. On the other hand, the ions with the same sign of electrical charge are mutually repelled. This physical phenomenon leads to the following idea of ion distribution in the fluid near the solid surface.

We consider that the electric potential $\hat{\phi}^S$ of the solid part is evenly distributed and stays constant. Near the interface between the fluid and the solid, the ionic attraction starts to take effect. The ions of the solid phase are strongly attached to its crystal lattice and cannot move as freely as ions of the fluid phase, thus the fluid ions are the ones changing places. The ions have finite size and thus cannot get closer to the solid surface than to a certain distance d, [10]. This leads to the creation of an area without charge in the fluid phase near the solid surface. According to [10], permitivity of this zone differs from the bulk value of ϵ_F in the rest of the fluid and can be a function of position.

Behind this charge-free zone, the ions with charge opposite to the solid ions start to accumulate. As the distance from the solid surface rises, the attraction between the opposing ions is getting weaker. This effect is illustrated by the Fig.17. The potential at the solid surface is $\hat{\phi}^M$ and we consider it to be the same as the potential of the solid $\hat{\phi}^S$. The distribution of the potential in the

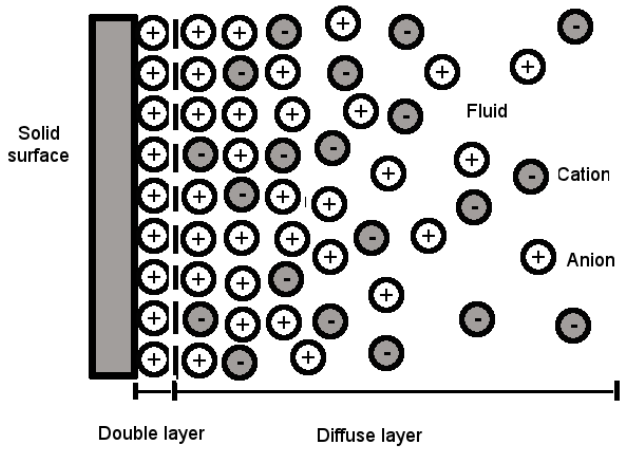

Figure 17: Illustration of double layer, source [17]

fluid can be determined by the Poisson equation

$$\mathrm{div}\epsilon \boldsymbol{E} = \pi, \tag{115}$$

where, π is the local volume density of the charge. The electric charge $\boldsymbol{E}$ can be express as

$$\boldsymbol{E} = -\mathrm{grad}\hat{\phi}, \tag{116}$$

and than the Eq.(115) is transformed into

$$\mathrm{div}(\epsilon \mathrm{grad}\hat{\phi}) = -\pi. \tag{117}$$

Now we focus on the region $x > d$. The permitivity ϵ is constant, thus Eq.(5.4) can be written as

$$\mathrm{divgrad}\hat{\phi} = \nabla^2\hat{\phi} = -\pi\frac{1}{\epsilon}. \tag{118}$$

In what follows, we focus on determining the volume charge density ρ. In the region $x > d$, the ions are influenced by the local electrostatic potential. Thus, if the solid surface is charged, the ion concentration is characterized by Boltzmann equation

$$Q_i = Q_i^0 \exp\left(-\frac{w_i}{k_B T}\right), \tag{119}$$

where Q_i is the concentration of ions of type i, the Q_i^0 is the bulk concentration of the ions of type

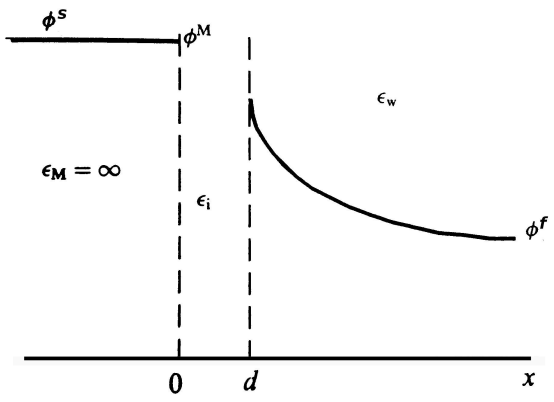

Figure 18: Potential distribution near the flat surface, source [10]

i, T is the fluid temperature, k_B is the Boltzmann constant and by w_i we denote the work done by transporting ion i from the bulk solution $\hat{\phi}^F$ into the point in the double layer, where the potential is $\hat{\phi}$, [10].

Further, let us assume that the work is done just by moving ion in response to the electrical field. Such work is called electric work and can be described by

$$w_i = z_i e(\hat{\phi} - \hat{\phi}^F) = z_i e\psi, \tag{120}$$

where z_i represents the valency of ions, which can be positive or negative ($\pm$) and e is the ion charge. By ψ we denote the potential difference $(\hat{\phi} - \hat{\phi}^F)$. The volume charge density is defined as

$$\pi = \sum_i Q_i z_i e. \tag{121}$$

Finally, using Eq.(118)-(121), while assuming $\hat{\phi}^F$ constant, we obtain the Poisson-Boltzmann equation

$$\nabla^2\psi = -\frac{1}{\epsilon}\sum_i Q_i^0 z_i e \exp\left(\frac{-z_i e\psi}{k_B T}\right). \tag{122}$$

By solving this equation (see for example [10]), it can be shown, that the potential distribution of $\hat{\phi}^F$ in the region $x > d$ is as in the Fig.18. This equation can be also used to derive the variable characterizing the electro-osmosis, which is introduced in the section below.

5.5 Debye length

In the following text we introduce the variable characterizing the electro-osmosis, the so called Debye length λ_D. We use the Poisson-Boltzmann equation defined by Eq.(122) in the previous section. We consider the case, when the electrical energy is smaller in comparison to thermal

energy, ($|z_i e\psi| < |k_B T|$). Thus, it is possible to expand the exponential while neglecting all but the first two terms in Eq.(122) and obtain

$$\nabla^2\psi = -\frac{1}{\epsilon}\left[\sum_i Q_i^0 z_i e - \sum_i \frac{Q_i^0 z_i^2 e^2 \psi}{k_B T}\right]. \tag{123}$$

The first sum must be equal to zero to preserve electro-neutrality in the bulk solution,[10], thus

$$\nabla^2\psi = \sum_i \frac{Q_i^0 z_i^2 e^2 \psi}{\epsilon k_B T} = \left(\frac{1}{\lambda_D}\right)\psi, \tag{124}$$

where λ_D is the constant with the dimension of length, so-called Debye length. By expressing the Boltzmann constant in the form $k_B = \mathrm{R}/\mathrm{N_A}$, where $\mathrm{N_A} = 6.022141179 \times 10^{23}\mathrm{mol}^{-1}$ is the Avogadro constant and $\mathrm{R} = 8.314472\ \mathrm{J\ mol^{-1}K^{-1}}$ is the constant of ideal gas, and using the relation for Faraday constant $\mathrm{F} = e\mathrm{N_A}$, the Eq.(124) for Debye length is written as

$$\lambda_D = \sqrt{\sum_i \frac{\epsilon \mathrm{R} T}{Q_i^0 z_i^2 \mathrm{F}^2}}. \tag{125}$$

The Debye length is the measurement of extent of the double layer.

5.6 Microscopic problem description

Let us consider the medium occupying the domain Ω which is decomposed, similarly to the poroelastic problem, into the solid and fluid part denoted as Ω_s and Ω_f, respectively. The interface between the fluid and the solid part is denoted by Γ and is defined as follows

$$\Gamma = \partial\Omega_s \cap \partial\Omega_f. \tag{126}$$

Further, the following abbreviations are used

$$\Gamma_s = \Gamma \cap \partial\Omega_s, \tag{127}$$

$$\Gamma_f = \Gamma \cap \partial\Omega_f. \tag{128}$$

Let us define the normal unit vector $\boldsymbol{n}$ outward with regard to the bounding domain in general. Note that $\boldsymbol{n}^s = -\boldsymbol{n}^f \mathrm{on}\Gamma$. Due to that, for any vector function $\boldsymbol{a}$ with traces $\boldsymbol{a}_s \mathrm{on}\partial\Omega_s$ and $\boldsymbol{a}_f \mathrm{on}\partial\Omega_f$, the following expressions hold

$$\boldsymbol{n}.[\boldsymbol{a}]_\Gamma = \boldsymbol{n}^f.\left[\boldsymbol{a}_f - \boldsymbol{a}_s\right]_\Gamma = \boldsymbol{n}^s.\left[\boldsymbol{a}_s - \boldsymbol{a}_f\right]_\Gamma. \tag{129}$$

5.6.1 Electrostatics

In what follows, we denote the pair of molar concentrations of cations and anions by Q^+ and Q^-, respectively. Further, let us denote the electric field and the electric potential by $\boldsymbol{E}$ and Φ. In classical electrostatics, the relation between $\boldsymbol{E}$ and Φ is defined by Poisson equation Eq.(115) and then (116) result into (117). Applying the Poisson equation on the fluid part Ω_f and the solid part Ω_s, we obtain the following relations, see [22],

$$-\nabla \cdot \epsilon_s \nabla \Phi = \hat{\pi}_s + \nabla \cdot \mathbf{G} : \boldsymbol{e}(\boldsymbol{u}) \quad \text{in } \Omega_s, \tag{130}$$

$$-\nabla \cdot \epsilon_f \nabla \Phi = \pi_f \quad \text{in } \Omega_f, \tag{131}$$

where ϵ_d and π_d, $d = f, s$ is the permitivity and the volume electric charge in the solid or the fluid. The permitivity ϵ_d, $d = f, s$ is defined as $\alpha_d \epsilon_0$, where α_d is the relative permitivity and ϵ_0 is the permitivity of the void space.

The electric charge in the solid part can be produced by the piezoelectric effect. Thus on the right side of Eq.(130) is added the piezoelectric term, where $\boldsymbol{e}(\boldsymbol{u})$ is the deformation of the solid matrix and $\mathbf{G} = G_{ijk}$ is the piezoelectric coupling. More detailed information about the piezo-electricity effect in the cortical bone structure can be found in [16]. We consider that the piezo-electric term produces charge π_G and thus the total charge of the solid is

$$\pi_s = \hat{\pi}_s + \pi_G, \tag{132}$$

Using Faraday constant F and the valence of ion particles $z^+ = 1, z^- = -1$, the volume electric charge in the fluid π_f can be expressed, by the definition, as the product between the molar charge and the difference of concentration of cations and anions,[14],[22],[15]

$$\pi_f = \mathrm{F}(z^+ Q^+ - z^- Q^-). \tag{133}$$

By substituting Eq.(132) into (130) and Eq.(133) into (131) we obtain

$$-\nabla \cdot \alpha_s \epsilon_0 \nabla \Phi = \pi_s \quad \text{in } \Omega_s, \tag{134}$$

$$-\nabla \cdot \alpha_f \epsilon_0 \nabla \Phi = \mathrm{F}(z^+ Q^+ - z^- Q^-) \quad \text{in } \Omega_f. \tag{135}$$

5.6.2 Boundary conditions for the electrostatic problem

We assume, that the medium is insulated from the outer space, thus there is zero boundary condition

$$\boldsymbol{n}.\epsilon \nabla \Phi = 0 \quad \text{in } \partial\Omega. \tag{136}$$

The reasoning for another boundary condition is presented below.

We consider that there is a surface charge ϱ on the solid-fluid interface. This charge is considered to be distributed in a thin infinite layer of thickness d. According to [22], the transmission

condition can be derived by solving the following one-dimension Dirichlet problem

$$
\begin{aligned}
-\partial_x(\bar{\epsilon}\partial_x\hat{\phi}) &= \bar{\pi} + \rho\delta(x) \quad x \in]-d/2, +d/2[, && (137)\\
\hat{\phi}(-d/2) &= \hat{\phi}^-, && (138)\\
\hat{\phi}(+d/2) &= \hat{\phi}^+, && (139)
\end{aligned}
$$

where $\bar{\epsilon}$ is the constant permitivity, $\bar{\pi}$ is the constant volume charge and $\rho\delta(x)$ is the charge distribution at $x = 0$. By integrating Eq.(137), we obtain the following expression of the so-called "jump" $\left[\hat{\phi}\right]_-^+ = \hat{\phi}^+ - \hat{\phi}^-$,

$$
\bar{\epsilon}\left[\hat{\phi}\right]_-^+ = \bar{\epsilon}\partial_x\hat{\phi}(-d/2)d + \bar{\pi}\frac{d^2}{2} + \rho\frac{d}{2}, \tag{140}
$$

see [22].

Further, we assume the continuity of electric displacements, thus the term $\bar{\epsilon}\partial_x\hat{\phi}(-d/2)$ can be rewritten as $\epsilon^-\hat{\phi}^-$ and than the Eq.(140) transforms into

$$
\bar{\epsilon}[\hat{\phi}]_-^+ = \epsilon^-\partial_x\hat{\phi}^-d + \bar{\pi}\frac{d^2}{2} + \rho\frac{d}{2}. \tag{141}
$$

In our case the thin layer surrounding the solid-fluid interface Γ determined by the transversal direction unit vector $\boldsymbol{n}^s$ is generally oriented. According to that, Eq.(141) for one-dimension problem transforms into three-dimensional space

$$
\frac{\bar{\epsilon}}{d}[\Phi]_s^f = \boldsymbol{n}^s \cdot \nabla\Phi|_s + \frac{\varrho}{2}, \tag{142}
$$

where we denote $\varrho = \bar{\pi}d + \rho$.

Taking $\boldsymbol{n}^s = -\boldsymbol{n}^f$, we can determinate two boundary conditions

$$
\boldsymbol{n}^s \cdot \epsilon\nabla\Phi|_s = -\frac{\bar{\epsilon}_\Gamma}{d_\Gamma}[\Phi]_\Gamma - \frac{\varrho}{2}, \tag{143}
$$

$$
\boldsymbol{n}^f \cdot \epsilon\nabla\Phi|_f = -\frac{\bar{\epsilon}_\Gamma}{d_\Gamma}[\Phi]_\Gamma + \frac{\varrho}{2}, \tag{144}
$$

where $[\Phi]_\Gamma = \Phi|_s - \Phi|_f$.

5.6.3 Movement of the ions

In this section, the relations for the convection-diffusion transport of ionic particles in an incompressible fluid are derived. We assume the restriction on isothermic processes only (T =const.). Further we denote the water-ions diffusion coefficients for cations and anions by $\mathbb{D}^+$ and $\mathbb{D}^-$, respectively. According to [14], two convection-diffusion equations (where superscript "+" refers to

the variables belonging to cations and "-" to anions) governing ion transport are

$$\frac{\partial Q^+}{\partial t} + \nabla \cdot (Q^+ \boldsymbol{w}_f) - \nabla \cdot \left(\frac{\mathbb{D}^+ Q^+}{\mathrm{R}T} \nabla \mu^+ \right) = 0, \tag{145}$$

$$\frac{\partial Q^-}{\partial t} + \nabla \cdot (Q^- \boldsymbol{w}_f) - \nabla \cdot \left(\frac{\mathbb{D}^- Q^-}{\mathrm{R}T} \nabla \mu^- \right) = 0. \tag{146}$$

In what follows, we use a shorter notation for the relations with the same form but referring to ions with opposite charge

$$\frac{\partial Q^\pm}{\partial t} + \nabla \cdot (Q^\pm \boldsymbol{w}_f) - \nabla \cdot \left(\frac{\mathbb{D}^\pm Q^\pm}{\mathrm{R}T} \nabla \mu^\pm \right) = 0, \tag{147}$$

where $\mu^\pm$ are the molar electrochemical potentials of cations and anions, which can be approximated as follows (see [14])

$$\mu^\pm = \pm z^\pm \mathrm{F}\Phi + \mathrm{R}T \log Q^\pm. \tag{148}$$

Now we introduce the dimensionless potential $\hat{\Phi} = z^\pm \mathrm{F}\Phi / RT$ and by applying the ∇ operator on the Eq.(148) we obtain

$$\frac{1}{\mathrm{R}T} \nabla \mu^\pm = \frac{\nabla Q^\pm}{Q^\pm} \pm \nabla \hat{\Phi}. \tag{149}$$

Further, using Eq.(149), we obtain the Nerst-Planck equation, which, for the incompressible fluid, is defined as follows

$$\partial_t Q^\pm + \boldsymbol{w}_f \cdot \nabla Q^\pm - \nabla \cdot \mathbb{D}^\pm \cdot \left(\nabla Q^\pm \pm \frac{z^\pm \mathrm{F}}{\mathrm{R}T} Q^\pm \nabla \Phi \right) = 0 \quad \text{in } \Omega_f. \tag{150}$$

5.6.4 Boundary conditions for the problem of convection-diffusion

Note, that the Nerst-Planck Eq.(150) describes the mass balance describing the movement of the ion particles in the fluid medium. Since there is no mass transfer across the interface Γ, the boundary condition is

$$\boldsymbol{n} \cdot \mathbb{D}^\pm \cdot \left(\nabla Q^\pm \pm \frac{z^\pm \mathrm{F}}{\mathrm{R}T} Q^\pm \nabla \Phi \right) = 0 \quad \text{on } \Gamma. \tag{151}$$

Further, we have to preserve the electro-neutrality. This is enabled by the assumption of existence of a fluid-impermeable membrane on the outer surface $\partial\Omega_f \setminus \Gamma$. On this membrane is $\boldsymbol{n} \cdot \boldsymbol{w}_f = 0$. Let the ion concentration on this membrane be $Q_0^\pm$ such that the electro-neutrality is preserved

$$z^+ Q_0^+ - z^- Q_0^- = 0. \tag{152}$$

Thus, the last boundary condition is

$$Q^\pm = Q_0^\pm \quad \text{on } \partial\Omega_f \setminus \Gamma \tag{153}$$

5.6.5 Dimensionless problem formulation

We shall consider the following problem: for given π_s, ϱ and $\boldsymbol{w}_f$ find solutions (Φ, Q^+, Q^-) satisfying Eq.(130), (131), (136), (143), (144), (150), (151) and (153). In what follows, we transform this problem into its dimensionless form.

Let us introduce the dimensionless quantities $\varphi = \Phi/\bar{\Phi}$, $q^\pm = Q^\pm/\bar{Q}$. Further, we choose $\bar{z}\bar{Q} = z^+Q^+$ according to the neutrality state of the solution concentrations.

Let us divide Eq.(134) by $\bar{\Phi}$

$$-\nabla \cdot \alpha_s \epsilon_0 \nabla \frac{\Phi}{\bar{\Phi}} = \frac{\pi_s}{\bar{\Phi}} \quad \text{in } \Omega_s \tag{154}$$

The permitivity ϵ_0 is constant, thus we can divide the whole equation by it. Upon introducing $\tilde{\pi}_s = \pi_s/\bar{\Phi}\epsilon_0$ we can write the dimensionless form of Eq.(134)

$$-\nabla \cdot \alpha_s \nabla \varphi = \tilde{\pi}_s \quad \text{in } \Omega_s. \tag{155}$$

Further, we substitute $Q^\pm$ in the Eq.(135) and than divide by $\epsilon_0\bar{\phi}$

$$-\nabla \alpha_f \epsilon_0 \nabla \frac{\Phi}{\bar{\Phi}} = \frac{\mathrm{F}}{\epsilon_0 \bar{\Phi}}(z^+q^+\bar{Q} - z^-q^-\bar{Q}). \tag{156}$$

We consider $\bar{z} = z^+ = z^-$ and $\bar{\phi} = \frac{\mathrm{R}T}{\mathrm{F}\bar{z}}$. The Eq.(156) transform into

$$-\nabla \alpha_f \nabla \varphi = \frac{\bar{Q}(\bar{z}\mathrm{F})^2}{\epsilon_0 \mathrm{R}T}(q^+ - q^-). \tag{157}$$

Let us return to the definition of Debye length with the definition given by Eq.(125). For the case, where there are two types of ions ($\pm$) with valence $\bar{z} = z^+ = z^-$ and both with concentration $\bar{Q}$, the Eq.(125) yields

$$\lambda_D = \sqrt{\frac{\epsilon_0 RT}{2\bar{Q}(\bar{z}F)^2}}. \tag{158}$$

Using Eq.(158) we can rewrite Eq.(157) into the dimensionless form

$$-\nabla \cdot \alpha_f \nabla \varphi - \frac{1}{2\lambda_D^2}(q^+ - q^-) = 0 \quad \text{in } \Omega_f. \tag{159}$$

We divide the boundary conditions Eqs.(136), (143) and (144) by $\bar{\Phi}\epsilon_0$ and considering $\boldsymbol{n} = \boldsymbol{n}^s = -\boldsymbol{n}^f$ we obtain their dimensionless form

$$\boldsymbol{n} \cdot \alpha \nabla \varphi \;\; = \;\; 0 \quad \text{on } \partial\Omega\,, \tag{160}$$

$$\boldsymbol{n}\cdot\alpha\nabla\varphi|_s = -\frac{\alpha_\Gamma}{d_\Gamma}[\varphi]_\Gamma - \frac{\tilde{\varrho}}{2} \quad \text{on } \Gamma_s\,, \tag{161}$$

$$-\boldsymbol{n}\cdot\alpha\nabla\varphi|_f = \frac{\alpha_\Gamma}{d_\Gamma}[\varphi]_\Gamma - \frac{\tilde{\varrho}}{2} \quad \text{on } \Gamma_f\,, \tag{162}$$

where $\tilde{\varrho} = \frac{\varrho}{\bar{\Phi}\epsilon_0}$.

Now we focus on the dimensionless formulation of the convect-diffusion of ion equation (150) with boundary conditions (151) and (153). We substitute $\Phi = \varphi\bar{\Phi}$ into Eq.(150) and (151) and then all three equations divide by $\bar{Q}$. Upon these operations, the dimensionless form of Eq.(150) and their boundary conditions (151) and (153) is

$$\partial_t q^\pm + \boldsymbol{w}_f\cdot\nabla q^\pm - \nabla\cdot\mathbb{D}^\pm\cdot(\nabla q^\pm \pm \beta q^\pm\nabla\varphi) = 0 \quad \text{in } \Omega_f, \tag{163}$$

$$\mathbb{D}^\pm\cdot(\nabla q^\pm \pm \beta q^\pm\nabla\varphi) = 0 \quad \text{on } \Gamma\,, \tag{164}$$

$$q^\pm = \bar{q}^\pm \quad \text{on } \partial\Omega\,, \tag{165}$$

where $\beta = \bar{\Phi}zF/(RT)$ and $\bar{q}^\pm = Q^\pm/\bar{Q}$, i.e. $\bar{q}^+ = \bar{q}^- = 1$ due to the electro-neutrality on $\partial\Omega_f \setminus \Gamma$, [22].

For the record, the dimensionless microscopic problem formulation is given by Eqs.(155) and (159)-(165) as

$$\begin{aligned}
-\nabla\cdot\alpha_s\nabla\varphi &= \tilde{\pi}_s \quad \text{in } \Omega_s\,,\\
-\nabla\cdot\alpha_f\nabla\varphi - \frac{1}{2\lambda_D^2}(q^+ - q^-) &= 0 \quad \text{in } \Omega_f\,,\\
\boldsymbol{n}\cdot\alpha\nabla\varphi &= 0 \quad \text{on } \partial\Omega\,,\\
\boldsymbol{n}\cdot\alpha\nabla\varphi|_s &= -\frac{\alpha_\Gamma}{d_\Gamma}[\varphi]_\Gamma - \frac{\tilde{\varrho}}{2} \quad \text{on } \Gamma_s\,,\\
-\boldsymbol{n}\cdot\alpha\nabla\varphi|_f &= \frac{\alpha_\Gamma}{d_\Gamma}[\varphi]_\Gamma - \frac{\tilde{\varrho}}{2} \quad \text{on } \Gamma_f\,,\\
\partial_t q^\pm + \boldsymbol{w}_f\cdot\nabla q^\pm - \nabla\cdot\mathbb{D}^\pm\cdot(\nabla q^\pm \pm \beta q^\pm\nabla\varphi) &= 0 \quad \text{in } \Omega_f\,,\\
\boldsymbol{n}\cdot\mathbb{D}^\pm\cdot(\nabla q^\pm \pm \beta q^\pm\nabla\varphi) &= 0 \quad \text{on } \Gamma\,,\\
q^\pm &= \bar{q}^\pm \quad \text{on } \partial\Omega\,,
\end{aligned} \tag{166}$$

5.7 Weak problem formulation

In order to perform the unfolding homogenization method, it is more suitable to work with the weak problem formulation then with the PDE system (166). The transformation of the system (166) into its weak formulation is our main goal in the following text. At first we need to define the spaces of admissible and test functions ψ, θ^+, θ^-, subjected to the boundary conditions of the problem (166),

as

$$\begin{aligned} \tilde{H}^1(\Omega_s) &= \{\psi \in H^1(\Omega)\ ,\ \int_{\Omega_s} \psi = 0\}\ , \\ \tilde{H}^1(\Omega_s, \Omega_f) &= L^2(\Omega_s \cup \Omega_f) \cap \tilde{H}^1(\Omega_s) \cap H^1(\Omega_f)\ , \\ H^1_{\pm}(\Omega_f) &= \{\theta^{\pm} = (\theta^+, \theta^-) \in [H^1(\Omega_f)]^2\ ,\ \theta^{\pm} = 0\ \text{ on } \partial\Omega_f \setminus \Gamma\}\ , \end{aligned} \tag{167}$$

where $H^1(\Omega)$ is the Sobolev space of scalar functions and $L^2(\Omega)$ is the space of square-integrable functions.

First we introduce the general relation published in [12], which can be used for the derivation of the weak formulation for one dimension problem on $x =< 0, 1 >$ and its boundary conditions. The problem is defined as

$$\begin{aligned} &-(m(x)u')' + n(x)u = f(x), \\ &\alpha_0 u(0) - \beta_0 m(0)u'(0) = g_0, \\ &\alpha_1 u(1) - \beta_1 m(1)u'(1) = g_1. \end{aligned} \tag{168}$$

The weak formulation of the general one-dimension problem can be written as

$$\begin{aligned} \int_0^1 \left[m(x)u'(x)v'(x) + n(x)u(x)v(x)\right] dx + \frac{\alpha_0}{\beta_0}u(0)v(0) + \frac{\alpha_1}{\beta_1}u(1)v(1) = \\ = \int_0^1 f(x)v(x)dx + \frac{g_0}{\beta_0}v(0) + \frac{g_1}{\beta_1}v(1). \end{aligned} \tag{169}$$

We can imagine, that for the three-dimension problem the integrals are over the three-dimension domain and the terms obtained by the boundary conditions are integrated over the boundary (or interface), where they are defined.

Due to the electro neutrality on $\partial\Omega_s \setminus \Gamma$, i.e. the boundary condition $q^{\pm} = 1$, we can introduce $\vartheta^{\pm} = q^{\pm} - 1 \in H^1{}_{\pm}(\Omega_f)$. By $\Delta_{\pm}\vartheta^{\pm} = 1/2(q^+ - q^-)$ we denote the difference of the ion concentrations. By using the formula (169) we can rewrite system Eq.(166) to a weak form: find couple $(\varphi, \vartheta^{\pm}) \in \tilde{H}^1(\Omega_s, \Omega_f) \times H^1_{\pm}(\Omega_f)$ such that

$$\begin{aligned} \int_{\Omega_s} \alpha_s \nabla\phi \cdot \nabla\psi + \int_{\Omega_f} \alpha_f \nabla\phi \cdot \nabla\psi + \int_{\Gamma} \frac{\alpha_\Gamma}{d_\Gamma}[\phi]_\Gamma[\psi]_\Gamma - \lambda_d^{-2} \int_{\Omega_f} \Delta_{\pm}\vartheta^{\pm}\psi = \\ = \int_{\Omega_s} \tilde{\pi}_s\psi + \int_{\Gamma} \tilde{\varrho}\frac{1}{2}(\psi|_s + \psi|_f) \quad \forall\psi \in \tilde{H}^1(\Omega_s, \Omega_f), \end{aligned} \tag{170}$$

$$\int_{\Omega_f} \partial_t \vartheta^{\pm}\theta^{\pm} + \int_{\Omega_f} w_f \cdot \nabla\vartheta^{+}\theta^{+} + \int_{\Omega_f} w_f \cdot \nabla\vartheta^{-}\theta^{-} + \int_{\Omega_f} (\mathbb{D}^{+} \cdot \nabla\vartheta^{+}) \cdot \nabla\theta^{+} + \int_{\Omega_f} (\mathbb{D}^{-} \cdot \nabla\vartheta^{-}) \cdot \nabla\theta^{-} +$$
$$\int_{\Omega_f} \beta\nabla\phi \cdot (\vartheta^{+}\mathbb{D}^{+} \cdot \nabla\theta^{+} - \vartheta^{-}\mathbb{D}^{-} \cdot \nabla\theta^{-}) + \int_{\Omega_f} \beta\nabla\phi \cdot (\mathbb{D}^{+} \cdot \nabla\theta^{+} - \mathbb{D}^{-} \cdot \nabla\theta^{-}) = 0 \quad \forall\theta^{\pm} \in H^1_{\pm}(\Omega_f) \quad (171)$$

The equations of the weak formulation are quite long, so in order to simplify the mathematical notations we introduce the following functional forms

$$a_{\Omega}(\phi,\psi) = \int_{\Omega_s} \alpha_s \nabla\phi \cdot \nabla\psi + \int_{\Omega_f} \alpha_f \nabla\cdot\phi\nabla\psi \quad (172)$$

$$d_{\Omega_f}(q^{\pm},\theta^{\pm}) = \int_{\Omega_f} \left[(\mathbb{D}^{+} \cdot \nabla q^{+}) \cdot \nabla\theta^{+} + (\mathbb{D}^{-} \cdot \nabla q^{-}) \cdot \nabla\theta^{-}\right] \quad (173)$$

$$c_{\Omega_f}(\mathbf{w},\nabla q^{\pm},\theta^{\pm}) = \int_{\Omega_f} (\theta^{+}\mathbf{w} \cdot \nabla q^{+} + \theta^{-}\mathbf{w} \cdot \nabla q^{-}) \quad (174)$$

$$b_{\Omega_f}(q^{\pm},\phi,\theta^{\pm}) = \int_{\Omega_f} \beta\nabla\phi \cdot (q^{+}\mathbb{D}^{+} \cdot \nabla\theta^{+} - q^{-}\mathbb{D}^{-} \cdot \nabla\theta^{-}) \quad (175)$$

$$\langle\phi,\psi\rangle_{\Omega_s} = \int_{\Omega_s} \phi\psi \quad (176)$$

$$\langle q^{\pm}\theta^{\pm}\rangle_{\Omega_f} = \int_{\Omega_f} (q^{+}\theta^{+} + q^{-}\theta^{-}). \quad (177)$$

$$(178)$$

Using the functional forms defined above, the weak formulation given by Eq.(170) - (171) transforms into

$$a_{\Omega}(\phi,\psi) + \langle\frac{\alpha_{\Gamma}}{d_{\Gamma}}[\phi]_{\Gamma},[\psi]_{\Gamma}\rangle_{\Gamma} - \lambda_d^{-2}\langle\Delta_{\pm}\vartheta^{\pm},\psi\rangle_{\Omega_f} =$$
$$= \langle\tilde{\pi}_s,\psi\rangle_{\Omega_s} - \langle\tilde{\varrho},\frac{1}{2}(\psi|_s + \psi|_f)\rangle_{\Gamma} \quad \forall\psi \in \tilde{H}^1(\Omega_s,\Omega_f), \quad (179)$$

$$\langle\partial_t\vartheta^{\pm},\theta^{\pm}\rangle_{\Omega_f} + c_{\Omega_f}(\mathbf{w}_f,\nabla\vartheta^{\pm},\theta^{\pm}) + d_{\Omega_f}(\vartheta^{\pm},\theta^{\pm}) + b_{\Omega_f}(1,\phi,\theta^{\pm})b_{\Omega_f}(\vartheta^{\pm},\phi,\theta^{\pm}) +$$
$$+ = 0 \quad \forall\theta^{\pm} \in H^1_{\pm}(\Omega_f). \quad (180)$$

5.7.1 Linearized problem

In what follows we introduce some assumptions to linearize the problem above, [22]. We shall consider some scaling of the parameters which control the electric field in the thin (double) layer on Γ^ε.

The charge distribution in the whole domain Ω must be bounded, i.e. the $L^1(\Gamma^\varepsilon)$-norm of $\tilde{\varrho}$ must also be bounded

$$\|\tilde{\varrho}^\varepsilon\|_{L^1(\Gamma^\varepsilon)} = \int_\Omega \frac{1}{\varepsilon|Y|} \int_{\Gamma_Y} |\tilde{\varrho}^\varepsilon| \leq C. \tag{181}$$

Therefore, we consider the so-called moderate charges as $\tilde{\varrho}^\varepsilon = \varepsilon\bar{\varrho}$.

Further, we may consider the double-permitivity of the double-layer and introduce $\alpha_\Gamma^\varepsilon = \varepsilon^2\bar{\alpha}_\Gamma$.

Keeping a constant ratio between the size of the microstructure 1ε and the double-layer thickness results in $d_\Gamma^\varepsilon = \varepsilon\bar{d}$. Thus, we introduce $\bar{\alpha} = \bar{\alpha}_\Gamma/\bar{d}$, so that

$$\varepsilon\bar{\alpha} = \frac{\varepsilon^2\bar{\alpha}_\Gamma}{\varepsilon\bar{d}}. \tag{182}$$

With those simplifications, the weak form for the linearized problem is: find couple $(\phi, \vartheta^\pm) \in \tilde{H}^1(\Omega_s, \Omega_f) \times H^1_\pm(\Omega_f)$ such that

$$\begin{aligned} a_\Omega(\varphi,\psi) + \varepsilon\langle\alpha_\Gamma[\varphi]_\Gamma, [\psi]_\Gamma\rangle_\Gamma - \lambda_d^{-2}\langle\Delta_\pm\vartheta^\pm,\psi\rangle_{\Omega_f} \quad = \\ = \langle\tilde{\pi}_s,\psi\rangle_{\Omega_s} + \langle\varepsilon\tilde{\varrho}, \frac{1}{2}(\psi|_s + \psi|_f)\rangle_\Gamma \quad \forall\psi \in \tilde{H}^1(\Omega_s,\Omega_f), \end{aligned} \tag{183}$$

$$\begin{aligned} \langle\partial_t\vartheta^\pm,\theta^\pm\rangle_{\Omega_f} + c_{\Omega_f}(\mathbf{w}_f, \nabla\vartheta^\pm, \theta^\pm) + d_{\Omega_f}(\vartheta^\pm,\theta^\pm) + \\ + b_{\Omega_f}(1,\varphi,\theta^\pm) + b_{\Omega_f}(\vartheta^\pm,\varphi,\theta^\pm) = 0 \quad \forall\theta^\pm \in H^1_\pm(\Omega_f) \end{aligned} \tag{184}$$

where $c^\pm$ is given ionic concentration, $c^\pm \in L^\infty(0,T;\mathbf{L}^\infty(\Omega_f))$, and $\mathbf{w}_f$ is a given convection velocity,$\mathbf{w}_f \in L^\infty(0,T;\mathbf{L}^\infty(\Omega_f))$. Further, we assume "moderate jumps" so that $d_\Gamma = \varepsilon\bar{d}$ and introduce $\bar{\alpha} = \alpha_\Gamma/\bar{d}$.

5.7.2 Limit model

In the following text, we briefly introduce the steps leading to the limit model. Note that this approach follows the one introduced for the model of poroelasticity.

Let us consider the domain Ω generated by periodically repeating the RPC Y, which is de-

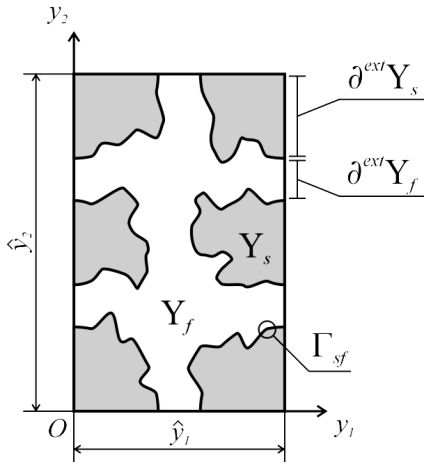

Figure 19: RPC Y decomposition, source [20]

composed into fluid and solid parts similarly to Ω decomposition

$$Y = Y_s \cup Y_f \cup \Gamma_Y, \quad Y_f = Y \setminus \bar{Y}_f, \quad \Gamma_Y = \bar{Y}_s \cap \bar{Y}_f. \tag{185}$$

and with the boundary,

$$\Gamma_Y = \partial Y_s \cap \partial Y_f. \tag{186}$$

The scale parameter between the dimension of the macroscopic domain Ω and RPC Y is denoted by ε. The fluid part Y_f generates a set obtained by the ε-periodicity as

$$\Omega_f = \varepsilon(\overline{Y}_f + k_i \hat{yb}_i) \cap \Omega, \quad k \in \mathbb{ZZ}^3 \tag{187}$$

where $\mathbb{ZZ}$ is a set of integers. The matrix part can be expressed as $\Omega_s = \Omega \setminus \overline{\Omega}_f$.

In order to obtain the limit model we use the unfolding method, whose main tool is the unfolding operator $\mathcal{T}_\varepsilon(\Omega)$ which is described in the section 4.2.7. We introduce the decomposition of the potential φ^ε and concentrations $\vartheta^{\pm,\varepsilon}$ into its "macroscopic" and "microscopic" parts, which should capture the fluctuations, as follows

$$\varphi^\varepsilon(\boldsymbol{x}) = \varphi^{\varepsilon,0}(\boldsymbol{x}, \frac{\boldsymbol{x}}{\varepsilon}) + \varepsilon\varphi^{1,\varepsilon}(\boldsymbol{x}, \frac{\boldsymbol{x}}{\varepsilon}) \tag{188}$$

$$\vartheta^{\pm\varepsilon}(\boldsymbol{x}) = \vartheta^{\pm 0}(\boldsymbol{x}, \frac{\boldsymbol{x}}{\varepsilon}) + \varepsilon\vartheta^{\pm 1}(\boldsymbol{x}, \frac{\boldsymbol{x}}{\varepsilon}). \tag{189}$$

Upon applying the unfolding operator, the potential and concentration decompositions and their gradients converge to the following limits

$$
\begin{aligned}
\mathcal{T}_\varepsilon(\vartheta^{\pm\varepsilon}) &\to \vartheta^{0\pm} \quad \text{s. in } L^\infty(0,T;\mathbf{L}^2(\Omega\times Y_f))\,,\\
\mathcal{T}_\varepsilon(\nabla\vartheta^{\pm\varepsilon}) &\rightharpoonup \nabla_x\vartheta^{0\pm}+\nabla_y\vartheta^{1\pm} \quad \text{w. in } L^2(0,T;\mathbf{L}^2(\Omega\times Y_f))\,,\\
\mathcal{T}_\varepsilon(\varphi^{\varepsilon}) &\to \varphi_f^0 \quad \text{s. in } L^2(0,T;\mathbf{L}^2(\Omega\times Y_f))\,,\\
\mathcal{T}_\varepsilon(\nabla\varphi^{\varepsilon}) &\rightharpoonup \nabla_x\varphi_f^0+\nabla_y\varphi_f^1 \quad \text{w. in } L^2(0,T;\mathbf{L}^2(\Omega\times Y_f))\,,\\
\mathcal{T}_\varepsilon(\varphi^{\varepsilon}) &\to \varphi_s^0 \quad \text{s. in } L^2(0,T;\mathbf{L}^2(\Omega\times Y_s))\,,\\
\mathcal{T}_\varepsilon(\nabla\varphi^{\varepsilon}) &\rightharpoonup \nabla_x\varphi_s^0+\nabla_y\varphi_s^1 \quad \text{w. in } L^2(0,T;\mathbf{L}^2(\Omega\times Y_s))\,,
\end{aligned}
\tag{190}
$$

Further, we consider the similar decomposition of the test function ψ^ε and $\theta^{\pm\varepsilon}$ also with the similar convergence upon applying the unfolding operator. By substituting φ^ε, $\vartheta^{\pm,\varepsilon}$, ψ^ε and $\theta^{\pm\varepsilon}$ into Eq.(183) and (184) and performing the unfolding, the system transforms into its limit form

$$
\begin{aligned}
&\int\limits_{\Omega\times Y_f}\alpha_f\left(\nabla_x\varphi_f^0+\nabla_y\varphi_f^1\right)\cdot\left(\nabla_x\psi_f^0+\nabla_y\psi_f^1\right)+\int\limits_{\Omega\times Y_s}\alpha_s\left(\nabla_x\varphi_s^0+\nabla_y\varphi_s^1\right)\cdot\left(\nabla_x\psi_s^0+\nabla_y\psi_s^1\right)\\
&+\int\limits_{\Omega\times\Gamma_Y}\bar\alpha(\varphi_f^0-\varphi_s^0)(\psi_f^0-\psi_s^0)\bar\rho\,\mathrm{dS}_y-\frac{1}{\lambda_D^2}\int\limits_{\Omega\times Y_f}\psi_f^0(\vartheta^{0+}-\vartheta^{0-})=\int\limits_{\Omega\times Y_s}\tilde\pi\psi_s^0+\int\limits_\Omega\frac{(\psi_f^0+\psi_s^0)}{2}\int\limits_{\Gamma_Y}\bar\rho\,\mathrm{dS}_y\,,
\end{aligned}
\tag{191}
$$

for all $\psi_f^0,\psi_s^0\in H^1(\Omega)$, $\psi_f^1\in L^2(\Omega;H^1_\#(Y_f))$, $\psi_s^1\in L^2(\Omega;H^1_\#(Y_s)$,

$$
\begin{aligned}
&\int\limits_{\Omega\times Y_f}\partial_t\vartheta^{0\pm}\,\theta^{0\pm}+\int\limits_{\Omega\times Y_f}\boldsymbol{w}\cdot\left(\nabla_x\vartheta^{0\pm}+\nabla_y\vartheta^{1\pm}\right)\theta^{0\pm}\\
&+\int\limits_{\Omega\times Y_f}(\mathbb{D}^\pm\cdot\left(\nabla_x\vartheta^{0\pm}+\nabla_y\vartheta^{1\pm}\right))\cdot\left(\nabla_x\theta^{0\pm}+\nabla_y\theta^{1\pm}\right)\\
&+\int\limits_{\Omega\times Y_f}\bar\beta(\pm c^\pm)\mathbb{D}^\pm\cdot\left(\nabla_x\varphi_f^0+\nabla_y\varphi_f^1\right)\cdot\left(\nabla_x\theta^{0\pm}+\nabla_y\theta^{1\pm}\right)=0
\end{aligned}
\tag{192}
$$

for all $\theta^{0\pm}\in H^1_\pm(\Omega)$, $\theta^{1\pm}\in L^2(\Omega;H^1_\#(Y_f))$, [22].

From the form of the limit problem we can see, that the potential φ and also its test function split under the effect of the unfolding operator into their fluid and solid part.

5.7.3 Local model

The local model, relevant to the microscopic scale, is derived from the limit problem above. We let all the components of the test functions, which are not relevant to the microscopic scale, vanish.

Thus, we choose the test functions only as $\theta^{1\pm}, \psi_f^1$ and ψ_s^1. The system of Eq.(191) and (192) then transforms into its local formulation: Find $(\varphi_f^1, \varphi_s^1, \vartheta^{1\pm})$ such that for $x \in \Omega$

$$\fint_{Y_f} \alpha_f \left(\nabla_x \varphi_f^0 + \nabla_y \varphi_f^1\right) \cdot \nabla_y \psi_f^1 = 0 \tag{193}$$

$$\fint_{Y_s} \alpha_s \left(\nabla_x \varphi_s^0 + \nabla_y \varphi_s^1\right) \cdot \nabla_y \psi_s^1 = 0 \ , \tag{194}$$

$\psi_f^1(x, \cdot) \in H^1_\#(Y_f)$ and

$$\fint_{\Omega \times Y_f} (\mathbb{D}^\pm \cdot \left(\nabla_x \vartheta^{0\pm} + \nabla_y \vartheta^{1\pm}\right)) \cdot \nabla_y \theta^{1\pm} + \fint_{\Omega \times Y_f} \bar{\beta}(\pm c^\pm) \mathbb{D}^\pm \cdot \left(\nabla_x \varphi_f^0 + \nabla_y \varphi_f^1\right) \cdot \nabla_y \theta^{1\pm} = 0 \ , \tag{195}$$

for all $\theta^{1\pm}(x, \cdot) \in H^1_\#(Y_f)$.

5.7.4 Homogenized coefficients

Similarly to the previous model, in order to obtain the effective coefficients describing the properties on the macro scale, we have to introduce a set of corrector basis functions. Due to the linearity of the local problem we can express local variables $\vartheta^{1\pm}, \varphi_f^1$ and φ_s^1 as linear combinations using quantities involved in Eq.(193) and (195) as follows.

$$\vartheta^{1\pm} = \sum_{z=+,-} \Theta_z^{k\pm} \partial_k^x \vartheta^{0z} + \Xi^{k\pm} \partial_k^x \varphi_f^0 \ , \tag{196}$$

$$\varphi_f^1 = \sum_{z=+,-} \Psi_z^k \partial_k^x \vartheta^{0z} + \Phi_f^k \partial_k^x \varphi_f^0 \ , \tag{197}$$

$$\varphi_s^1 = \Phi_s^k \partial_k^x \varphi_s^0 \ , \tag{198}$$

where the corrector basis functions $\Theta_z^{k\pm}, \Xi^{k\pm}, \Psi_z^k, \Phi_f^k, \Phi_s^k$ satisfy the problems defined below. In order to abbreviate the mathematical notation, we introduce the following bilinear forms

$$a_Y^f(\phi, \psi) = \fint_{Y_f} \alpha_f(y) \nabla_y \phi \cdot \nabla_y \psi \tag{199}$$

$$a_Y^s(\phi, \psi) = \fint_{Y_s} \alpha_f(y) \nabla_y \phi \cdot \nabla_y \psi \tag{200}$$

$$d_Y^{f^-}(\theta, \eta) = \fint_{Y_f} \left(\mathbb{D}^-(y) \cdot \nabla_y \theta\right) \cdot \nabla_y \eta \tag{201}$$

$$d_Y^{f+}(\theta,\,\eta) \;=\; \fint_{Y_f} \Big(\mathbb{D}^+(y)\cdot\nabla_y\theta\Big)\cdot\nabla_y\eta \tag{202}$$

$$d_Y^{f}(\theta,\,\eta) \;=\; d_Y^{f+}(\theta,\,\eta) + d_Y^{f-}(\theta,\,\eta)\;, \tag{203}$$

$$b_Y^{f-}(c^-;\,\phi,\,\eta) \;=\; \fint_{Y_f} c^-\Big(\mathbb{D}^-(y)\cdot\nabla_y\phi\Big)\cdot\nabla_y\eta \tag{204}$$

$$b_Y^{f+}(c^+;\,\phi,\,\eta) \;=\; \fint_{Y_f} c^+\Big(\mathbb{D}^+(y)\cdot\nabla_y\phi\Big)\cdot\nabla_y\eta \tag{205}$$

$$b_Y^{f}(\pm c^\pm;\,\phi,\,\eta) \;=\; b_Y^{f+}(c^+;\,\phi,\,\eta) + b_Y^{f-}(-c^-;\,\phi,\,\eta)\;, \tag{206}$$

$$c_Y^{f}(\boldsymbol{w};\,\theta,\,\eta) \;=\; \fint_{Y_f} \Big(\boldsymbol{w}\cdot\nabla_y\theta\Big)\eta \tag{207}$$

Now, with the use of those bilinear forms, we introduce a set of problems leading to the corrector basis functions, [22]

1. Find $(\Xi^{k\pm}, \Phi_f^k) \in H^1_\#(Y_f)\times H^1_\#(Y_f)$ for $k = 1, 2, 3$ such that

$$a_Y^f\Big(\Phi_f^k + y_k,\,\psi\Big) \;=\; 0\,,\quad \forall\psi\in H^1_\#(Y_f)\,, \tag{208}$$

$$d_Y^{f+}\Big(\Xi^{k+},\,\theta^+\Big) + b_Y^{f+}\Big(+c^+;\,\Phi_f^k + y_k,\,\theta^+\Big) \;=\; 0\,, \tag{209}$$

$$d_Y^{f-}\Big(\Xi^{k-},\,\theta^-\Big) + b_Y^{f-}\Big(-c^-;\,\Phi_f^k + y_k,\,\theta^-\Big) \;=\; 0\,,\quad \forall\theta^\pm\in H^1_\#(Y_f)\,, \tag{210}$$

   These three equations are decoupled: first we solve Eq.(208) and then we use the obtained solution for Φ_f^k for computing Ξ^{k+}, Ξ^{k-} from Eq.(209) and (210) which are also decoupled.

2. Find $(\Theta_z^{k\pm}, \Psi_z^k) \in H^1_\#(Y_f)\times H^1_\#(Y_f)$ for $k = 1, 2, 3$ and $z = +, -$ satisfying

$$a_Y^f\Big(\Psi_z^k,\,\psi\Big) \;=\; 0\,,\quad \forall\psi\in H^1_\#(Y_f)\,, \tag{211}$$

$$d_Y^{f+}\Big(\Theta_z^{k+} + y_k,\,\theta^+\Big) + b_Y^{f+}\Big(+c^+;\,\Psi_z^k,\,\theta^+\Big) \;=\; 0\,, \tag{212}$$

$$d_Y^{f-}\Big(\Theta_z^{k-} + y_k,\,\theta^-\Big) + b_Y^{f-}\Big(-c^+;\,\Psi_z^k,\,\theta^-\Big) \;=\; 0\,,\quad \forall\theta^\pm\in H^1_\#(Y_f)\,. \tag{213}$$

   Again, these three equations are decoupled. In [22] is stated, that by coercivity the Eq.(211) yields $\Psi_z^k \equiv 0$. Then the correctors $\Theta_z^{k\pm}$ are computed using Eq.(212) and (213). Moreover, it can bee seen that $\Theta^{k\pm} := \Theta_+^{k\pm} = \Theta_-^{k\pm}$. Thus, the corrector basis problem transforms into

$$d_Y^{f+}\Big(\Theta^{k+} + y_k,\,\theta^+\Big) \;=\; 0\,,\quad \forall\theta^+\in H^1_\#(Y_f)\,, \tag{214}$$

$$d_Y^{f-}\Big(\Theta^{k-} + y_k,\,\theta^-\Big) \;=\; 0\,,\quad \forall\theta^-\in H^1_\#(Y_f)\,. \tag{215}$$

   Moreover, it can be shown, that for $\mathbb{D}^+ \equiv \mathbb{D}^-$ solutions of Eq.(214) and (215) are equivalent,

$\Theta^{k+} = \Theta^{k-}$.

3. In the solid compartment, the following problem is posed: correctors $\Phi_s^k \in H^1_\#(Y_s)$ satisfy the following equations (for $k = 1, 2, 3$):

$$a_Y^s\left(\Phi_s^k + y_k,\, \psi\right) = 0\ , \quad \forall \psi \in H^1_\#(Y_s)\ , \tag{216}$$

Upon introducing the corrector basis function, we can compute the effective coefficients. Due to the structure of the micro-problem, the expression of the local variables $\vartheta^{1\pm}, \varphi_f^1$ and φ_s^1 can be rewritten in a simpler form.

$$\begin{aligned}
\vartheta^{1\pm} &= \Theta^{k\pm}\partial_k^x(\vartheta^{0+} + \vartheta^{0-}) + \Xi^{k\pm}\partial_k^x\varphi_f^0\ , && (217)\\
\varphi_f^1 &= \Phi_f^k\partial_k^x\varphi_f^0\ , && (218)\\
\varphi_s^1 &= \Phi_s^k\partial_k^x\varphi_s^0.\ . && (219)
\end{aligned}$$

We may finally introduce the components of the homogenized coefficients for $k, l, i = 1, 2, 3$ and $z = +, -$:

$$\begin{aligned}
D_{kl}^+ &= d_Y^{f+}\left(\Theta^{l+} + y_l,\, y_k\right) = d_Y^{f+}\left(\Theta^{l+} + y_l,\, \Theta^{k+} + y_k\right)\ , && (220)\\
D_{kl}^- &= d_Y^{f-}\left(\Theta^{l-} + y_l,\, y_k\right) = d_Y^{f-}\left(\Theta^{l-} + y_l,\, \Theta^{k-} + y_k\right)\ , && (221)\\
B_{kl}^+(c^+) &= d_Y^{f+}\left(\Xi^{l+},\, y_k\right) + b_Y^{f+}\left(c^+;\, \Phi_f^l + y_l,\, y_k\right)\ , && (222)\\
B_{kl}^-(c^-) &= d_Y^{f-}\left(\Xi^{l-},\, y_k\right) + b_Y^{f-}\left(-c^-;\, \Phi_f^l + y_l,\, y_k\right)\ , && (223)\\
C_k^\pm(\boldsymbol{w}) &= c_Y^f\left(\boldsymbol{w};\, \Theta^{k\pm} + y_k,\, 1\right)\ , && (224)\\
S_k^\pm(\boldsymbol{w}) &= c_Y^f\left(\boldsymbol{w};\, \Xi^{k\pm} + y_k,\, 1\right)\ , && (225)\\
A_{lk}^f &= a_Y^f\left(\Phi_f^k + y_k,\, \Phi_f^k + y_l\right)\ , && (226)\\
A_{kl}^s &= a_Y^s\left(\Phi_s^k + y_k,\, \Phi_s^l + y_l\right)\ , && (227)
\end{aligned}$$

.

Note, that the expressions of $D_{kl}^\pm$ and $A_{kl}^{f,s}$ are symmetric, which is a simple consequence of the microscopic problem.

5.7.5 Homogenized model

With the help of the effective coefficients, which are an approximation of characteristics of the macroscopic level, we may finally introduce the macroscopic problem of electro-osmosis in a porous structure. The macroscopic form of the electrostatic equation for the potential φ_f^0, φ_s^0 in the solid and the fluid yields

$$\sum_{d=f,s}\int_\Omega \nabla\psi_d^0\cdot\mathbb{A}^d\cdot\nabla\varphi_d^0+\int_\Omega \mathcal{M}_{\Gamma_Y}(\bar{\alpha})(\varphi_f^0-\varphi_s^0)(\psi_f^0-\psi_s^0)-\frac{|Y_f|}{\lambda_D^2|Y|}\int_\Omega \psi_f^0(\vartheta^{0+}-\vartheta^{0-})=$$
$$=\int_\Omega \mathcal{M}_Y(\bar{\pi}_s)\psi_s^0+\int_\Omega \frac{\psi_f^0+\psi_s^0}{2}\mathcal{M}_{\Gamma_Y}(\tilde{\varrho}) \qquad (228)$$

for all $\psi_s^0,\psi_f^0\in H^1(\Omega)$. Note, that $\mathcal{M}$ is an operator of a mean value of a variable over domain.

The electro-diffusion on the macroscopic scale is described by two equations for concentrations $\vartheta^{0+/-}$)

$$\frac{|Y_f|}{|Y|}\int_\Omega \partial_t\vartheta^{0\pm}\theta^{0\pm}+\int_\Omega \boldsymbol{C}^{\pm}(\boldsymbol{w})\cdot\nabla(\vartheta^{0+}+\vartheta^{0-})\theta^{0\pm}+\int_\Omega \boldsymbol{S}^{\pm}(\boldsymbol{w})\cdot(\nabla\varphi_f^0)\theta^{0\pm}+$$
$$+\sum_{z=+,-}\int_\Omega \nabla\theta^{0\pm}\cdot\mathbb{D}^{\pm}\cdot\nabla(\vartheta^{0+}+\vartheta^{0-})+\int_\Omega \nabla\theta^{0\pm}\cdot\mathbb{B}^{\pm}\cdot\nabla\varphi_f^0 \quad =0\,, \qquad (229)$$

for all $\theta^{0\pm}\in H^1_{\pm}(\Omega)$.

5.7.6 Relation between the microscopic model and the macroscopic solution

By solving the macroscopic problem defined in the previous section, we obtain the macroscopic solutions $\vartheta^{0\pm},\varphi_s^0$ and φ_f^0. The relation between the local variables $\vartheta^{1\pm},\varphi_s^1$ and φ_f^1 is described by Eqs.(217)-(219). The local variables can be computed by substituting the macroscopic solutions and computed corrector basis functions into the Eqs.(217)-(219). We may express the local problem with the help of the macroscopic solution $\vartheta^{0\pm},\varphi_s^0$ and φ_f^0 only. For illustration of the expression of the local problem with macroscopic solution, let us substitute into the diffusion velocity term from the Nerst-Planc equation while considering $q^{0\pm}=q^0=\vartheta^0+1$

$$\mathbb{D}\left[\nabla_x q^0+\nabla_y q^1+\beta q^0(\nabla_x\phi_f^0+\nabla_y\phi_f^1)\right]= \qquad (230)$$
$$=\mathbb{D}\left[\nabla_x^k(\vartheta^0+1)+\nabla_y(\theta^k\nabla_x^k 2(\vartheta^0+1)+\Xi^k\nabla^k\phi_f^0)+\beta q^0(\nabla_x\phi_f^0+\nabla_y(\Phi_f^k\nabla_x^k\phi_f^0))\right] \qquad (231)$$

5.8 Semi-discretized microscopic local problem

Following the approach published in [24], we consider a finite element partition of Y with N number of all nodes. Further, we use the notation $\boldsymbol{\varphi}_d$ for the vectors of potential $\varphi_d, d=f,s$ and the notation $\boldsymbol{\vartheta}^{\pm}$ for the vectors of concentration $\vartheta^{\pm}$. By $N^d, d=f,s$ we denote the number of all free degrees of freedom of the vectors of potential $\boldsymbol{\varphi}_d$. By $N^{\pm}$ we denote the number of all free degrees of freedom of the vectors $\boldsymbol{\vartheta}^{\pm}$. By the capital bold letters we denote the matrices corresponding to the bilinear forms employed in the section 5.7.4. We introduce the matrix notation of used bilinear

forms in Tab.10

Bilinear form	Matrix	Size	Bilinear form	Matrix	Size
$a_Y^f(.,.)$	$\mathbf{A_f}$	$N^f \times N^f$	$a_Y^s(.,.)$	$\mathbf{A_s}$	$N^s \times N^s$
$d_Y^{f-}(.,.)$	$\mathbf{D_{f-}}$	$N^- \times N^-$	$d_Y^{f+}(.,.)$	$\mathbf{D_{f+}}$	$N^+ \times N^+$
$c_Y^f(.;.,.)$	$\mathbf{C_f}$	$N^\pm \times N^\pm$	$b_Y^{f-}(.;.,.)$	$\mathbf{B_{f-}}$	$N^f \times N^f$
$b_Y^{f+}(.;.,.)$	$\mathbf{B_{f+}}$	$N^f \times N^f$	$b_Y^f(.;.,.)$	$\mathbf{B_f}$	$N^f \times N^f$

Table 10: Matrix notation of used bilinear forms

Using the notation above, we can introduce a discretized form of the microscopic corrector problems Eqs.(208)-(216).

1. Approximation to correctors $(\Phi_f^k, \Xi^{k\pm})$ is denoted by $(\hat{\boldsymbol{\varphi}}_f^k, \hat{\boldsymbol{\vartheta}}^{k\pm})$:

$$\mathbf{A_f}\hat{\boldsymbol{\varphi}}_f^k + \mathbf{A_f}\mathbf{y}^k = 0, \tag{232}$$

$$\mathbf{D_{f+}}\hat{\boldsymbol{\vartheta}}^{k+} + \mathbf{B_{f+}}\hat{\boldsymbol{\varphi}}_f^k + \mathbf{B_{f+}}\mathbf{y}^k = 0, \tag{233}$$

$$\mathbf{D_{f-}}\hat{\boldsymbol{\vartheta}}^{k-} + \mathbf{B_{f-}}\hat{\boldsymbol{\varphi}}_f^k - \mathbf{B_{f-}}\mathbf{y}^k = 0. \tag{234}$$

2. Approximation to correctors $\Theta^{k\pm}$is denoted by $\tilde{\boldsymbol{\vartheta}}^{k\pm}$:

$$\mathbf{D_{f+}}\tilde{\boldsymbol{\vartheta}}^{k+} + \mathbf{D_{f+}}\mathbf{y}^k = 0, \tag{235}$$

$$\mathbf{D_{f-}}\tilde{\boldsymbol{\vartheta}}^{k-} + \mathbf{D_{f-}}\mathbf{y}^k = 0. \tag{236}$$

3. Approximation to corrector Φ_s^k is denoted by $\tilde{\boldsymbol{\varphi}}_s^k$:

$$\mathbf{A_s}\tilde{\boldsymbol{\varphi}}_s^k + \mathbf{A_s}\mathbf{y}^k = 0. \tag{237}$$

Using the vectors of the corrector basis functions we can evaluate the homogenized coefficients. Eqs.(220)-(227) have the following matrix form

$$D_{kl}^+ \approx (\mathbf{y}^k + \tilde{\boldsymbol{\vartheta}}^{k+})^T \mathbf{D_{f+}} (\mathbf{y}^k + \tilde{\boldsymbol{\vartheta}}^{k+}) , \tag{238}$$

$$D_{kl}^- \approx (\mathbf{y}^k + \tilde{\boldsymbol{\vartheta}}^{k-})^T \mathbf{D_{f-}} (\mathbf{y}^k + \tilde{\boldsymbol{\vartheta}}^{k-}) , \tag{239}$$

$$B_{kl}^+ \approx (\mathbf{y}^k)^T \mathbf{D_{f+}} \hat{\boldsymbol{\vartheta}}^{k+} + (\mathbf{y}^k)^T \mathbf{B_{f+}} (\hat{\boldsymbol{\varphi}}_f^k + \mathbf{y}^k) , \tag{240}$$

$$B_{kl}^- \approx (\mathbf{y}^k)^T \mathbf{D_{f-}} \hat{\boldsymbol{\vartheta}}^{k-} + (\mathbf{y}^k)^T \mathbf{B_{f-}} (\hat{\boldsymbol{\varphi}}_f^k + \mathbf{y}^k) , \tag{241}$$

$$C_k^\pm \approx \mathbf{C_f} (\mathbf{y}^k + \tilde{\boldsymbol{\vartheta}}^{k\pm}) , \tag{242}$$

$$S_k^{\pm} \approx \mathbf{C_f}(\mathbf{y}^k + \hat{\boldsymbol{\vartheta}}^{k\pm}) , \tag{243}$$
$$A_{lk}^f \approx (\hat{\boldsymbol{\varphi}}_f^k + \mathbf{y}^k)^T \mathbf{A_f} (\hat{\boldsymbol{\varphi}}_f^k + \mathbf{y}^k) , \tag{244}$$
$$A_{kl}^s \approx (\tilde{\boldsymbol{\varphi}}_s^k + \mathbf{y}^k)^T \mathbf{A_s} (\tilde{\boldsymbol{\varphi}}_s^k + \mathbf{y}^k) , \tag{245}$$

.

5.9 Discretized macroscopic problem

In this section we introduce the discretized form of the macroscopic problem, which can be used in the finite element (FE) model. By $\boldsymbol{\varphi}_d, d = f, s$ and $\boldsymbol{\vartheta}^{\pm}$ we refer to the column vector incorporating all degrees of freedom (DOF) of FE mesh nodes associated with the macroscopic domain Ω. We need the FE counterparts of the bilinear forms involved in the macroscopic problem Eqs.(228) and (229):

$$\begin{aligned}
(\boldsymbol{\theta}^+)^T \mathbf{T}^+ \boldsymbol{\vartheta}^+ &\approx \tfrac{|Y_f|}{|Y|} \textstyle\int_\Omega \partial_t \vartheta^+ \theta^+, & (\boldsymbol{\theta}^-)^T \mathbf{T}^- \boldsymbol{\vartheta}^- &\approx \tfrac{|Y_f|}{|Y|} \textstyle\int_\Omega \partial_t \vartheta^- \theta^-,\\
(\boldsymbol{\theta}^+)^T \mathbf{C}^+ \boldsymbol{\vartheta}^+ &\approx \textstyle\int_\Omega \boldsymbol{C}^+(\boldsymbol{w}) \cdot \nabla \vartheta^{0+} \theta^{0+}, & (\boldsymbol{\theta}^+)^T \mathbf{C}^+ \boldsymbol{\vartheta}^- &\approx \textstyle\int_\Omega \boldsymbol{C}^+(\boldsymbol{w}) \cdot \nabla \vartheta^{0-} \theta^{0+}\\
(\boldsymbol{\theta}^+)^T \mathbf{C}^- \boldsymbol{\vartheta}^+ &\approx \textstyle\int_\Omega \boldsymbol{C}^-(\boldsymbol{w}) \cdot \nabla \vartheta^{0+} \theta^{0-}, & (\boldsymbol{\theta}^+)^T \mathbf{C}^- \boldsymbol{\vartheta}^- &\approx \textstyle\int_\Omega \boldsymbol{C}^-(\boldsymbol{w}) \cdot \nabla \vartheta^{0-} \theta^{0-},\\
(\boldsymbol{\theta}^+)^T \mathbf{D}^+ \boldsymbol{\vartheta}^+ &\approx \textstyle\int_\Omega \nabla \theta^{0+} \cdot \mathbb{D}^+ \cdot \nabla \vartheta^{0+}, & (\boldsymbol{\theta}^+)^T \mathbf{D}^+ \boldsymbol{\vartheta}^- &\approx \textstyle\int_\Omega \nabla \theta^{0+} \cdot \mathbb{D}^+ \cdot \nabla \vartheta^{0-}\\
(\boldsymbol{\theta}^-)^T \mathbf{D}^- \boldsymbol{\vartheta}^+ &\approx \textstyle\int_\Omega \nabla \theta^{0-} \cdot \mathbb{D}^- \cdot \nabla \vartheta^{0+}, & (\boldsymbol{\theta}^-)^T \mathbf{D}^- \boldsymbol{\vartheta}^- &\approx \textstyle\int_\Omega \nabla \theta^{0-} \cdot \mathbb{D}^- \cdot \nabla \vartheta^{0-},\\
(\boldsymbol{\theta}^+)^T \mathbf{S}^+ \boldsymbol{\varphi}_f &\approx \textstyle\int_\Omega \boldsymbol{S}^+(\boldsymbol{w}) \cdot (\nabla \varphi_f^0) \theta^{0+}, & (\boldsymbol{\theta}^-)^T \mathbf{S}^- \boldsymbol{\varphi}_f &\approx \textstyle\int_\Omega \boldsymbol{S}^-(\boldsymbol{w}) \cdot (\nabla \varphi_f^0) \theta^{0-},\\
(\boldsymbol{\theta}^+)^T \mathbf{B}^+ \boldsymbol{\varphi}_f &\approx \textstyle\int_\Omega \nabla \theta^{0+} \cdot \mathbb{B}^+ \cdot \nabla \varphi_f^0, & (\boldsymbol{\theta}^-)^T \mathbf{B}^- \boldsymbol{\varphi}_f &\approx \textstyle\int_\Omega \nabla \theta^{0-} \cdot \mathbb{B}^- \cdot \nabla \varphi_f^0,\\
(\boldsymbol{\psi}_s)^T \mathbf{Z_s} \boldsymbol{\varphi}_s &\approx \textstyle\int_\Omega \nabla \psi_s^0 \cdot \mathbb{A}^s \cdot \nabla \varphi_s^0, & (\boldsymbol{\psi}_f)^T \mathbf{Z_s} \boldsymbol{\varphi}_f &\approx \textstyle\int_\Omega \nabla \psi_f^0 \cdot \mathbb{A}^f \cdot \nabla \varphi_f^0,\\
(\boldsymbol{\psi}_f)^T \mathbf{M} \boldsymbol{\varphi}_f &\approx \textstyle\int_\Omega \mathcal{M}_{\Gamma_Y}(\bar{\alpha}) \varphi_f^0 \psi_f^0, & (\boldsymbol{\psi}_s)^T \mathbf{M} \boldsymbol{\varphi}_f &\approx \textstyle\int_\Omega \mathcal{M}_{\Gamma_Y}(\bar{\alpha}) \varphi_f^0 \psi_s^0,\\
(\boldsymbol{\psi}_f)^T \mathbf{M} \boldsymbol{\varphi}_s &\approx \textstyle\int_\Omega \mathcal{M}_{\Gamma_Y}(\bar{\alpha}) \varphi_s^0 \psi_f^0, & (\boldsymbol{\psi}_s)^T \mathbf{M} \boldsymbol{\varphi}_s &\approx \textstyle\int_\Omega \mathcal{M}_{\Gamma_Y}(\bar{\alpha}) \varphi_s^0 \psi_s^0,\\
(\boldsymbol{\psi}_f)^T \mathbf{N} \boldsymbol{\vartheta}^+ &\approx \tfrac{|Y_f|}{\lambda_D^2 |Y|} \textstyle\int_\Omega \psi_f^0 \vartheta^{0+}, & (\boldsymbol{\psi}_f)^T \mathbf{N} \boldsymbol{\vartheta}^- &\approx \tfrac{|Y_f|}{\lambda_D^2 |Y|} \textstyle\int_\Omega \psi_f^0 \vartheta^{0-},\\
(\boldsymbol{\psi}_f)^T \mathbf{P_f} &\approx \textstyle\int_\Omega \tfrac{\psi_f^0}{2} \mathcal{M}_{\Gamma_Y}(\bar{\varrho}), & (\boldsymbol{\psi}_s)^T \mathbf{P_s} &\approx \textstyle\int_\Omega \psi_s^0 (\mathcal{M}_Y(\bar{\pi}_s) + \tfrac{1}{2} \mathcal{M}_{\Gamma_Y}(\bar{\varrho})).
\end{aligned}$$

The terms $\mathbf{T}^{\pm}$ are time dependent and continuous in time. For the purpose of computation we need to discretize them also in time. According to [24], we can introduce time discretization using so-called time increment Δt. Δt is defined as the difference between two following time steps, $\Delta t = t_{n+1} - t_n$. Let us assume that we know $\mathbf{T}^{\pm}{}_0$ in initial time t_0. We can compute any other time level t_n of $\mathbf{T}_{\mathbf{n}}^{\pm}$ by approximation

$$\mathbf{T}_{\mathbf{n}}^{\pm} \approx \Delta t \mathbf{T}_{\mathbf{n-1}}^{\pm}. \tag{246}$$

For small Δt, the approximation formula transforms into

$$\mathbf{T}_{\mathbf{n}}^{\pm} \approx \Delta t \mathbf{T}_{\mathbf{0}}^{\pm}. \tag{247}$$

For more detailed information about time discretization we recommend to look into [24].

Using the FE counterpart defined above, we can display the linear subproblems of the macro-

scopic problem in the matrix form

$$\begin{bmatrix} \Delta t\mathbf{T}_\mathbf{0}^{+} + \mathbf{C}^{+} + 2\mathbf{D}^{+} & \mathbf{C}^{+} + 2\mathbf{D}^{+} & 0 & \mathbf{S}^{+} + \mathbf{B}^{+} \\ \mathbf{C}^{-} + 2\mathbf{D}^{-} & \Delta t\mathbf{T}_\mathbf{0}^{-} + \mathbf{C}^{-} + 2\mathbf{D}^{-} & 0 & \mathbf{S}^{-} + \mathbf{B}^{-} \\ 0 & 0 & \mathbf{Z_s} + \mathbf{M} & -\mathbf{M} \\ -\mathbf{N} & \mathbf{N} & -\mathbf{M} & \mathbf{Z_s} + \mathbf{M} \end{bmatrix} \begin{bmatrix} \boldsymbol{\vartheta}^{+} \\ \boldsymbol{\vartheta}^{-} \\ \boldsymbol{\varphi}_s \\ \boldsymbol{\varphi}_f \end{bmatrix} = \begin{bmatrix} \mathbf{0} \\ \mathbf{0} \\ \mathbf{P_s} \\ \mathbf{P_f} \end{bmatrix}. \tag{248}$$

From the matrix form Eq.(248) is evident, that all equations describing the problem are coupled. The matrix of the problem is not singular, which means that the sub-matrices on the diagonal are regular. This is accomplished by a suitable choice of the boundary conditions. The matrix form is more suitable for implementation in the FE software, for example in *SfePy*.

5.10 Model parameters

In what follows, we introduce material parameters found by the literature survey which are relevant to the solid and the fluid part on the microscopic level. Later, we introduce the geometry used for describing the porosities in the microstructure.

5.10.1 Material parameters

In this section we introduce the parameters used for the numerical evaluation of the electro-osmosis model represented in the chapter 5.

First, let us focus on the diffusion coefficients $\mathbb{D}^{\pm}$. We consider the matrix on the microscopic level to be isotropic. The diffusion coefficients in a three-dimensional space have the form of a square 3×3 matrix. According to [11], the diffusion coefficient for the isotropic medium is a diagonal matrix with $D_{ii} = D_{jj}, i, j = x, y, z$. Thus, for the determination of the diffusion coefficient in the matrix form, we need just one scalar value D, which is multiplied by a unit matrix $\mathbb{I}$. The matrix form of the diffusion coefficient is computed as $\mathbb{D} = D\mathbb{I}$ The values of the scalar diffusion coefficients for Na^+ and Cl^- were estimated as values computed by [28], see Tab.11.

The relative permitivity α_s of the bone tissue was estimated in [19] as 111.5. For the relative permitivity α_f of the bone fluid, which is considered to be salt water, we use the value from [2]. Note, that all parameters can be found in Tab.11. Other parameters were chosen after consultation with Dr. Thibauld Lemaire.

5.10.2 Geometry for the model of electro-osmosis

The homogenization of the problem of electro-osmosis in the cortical bone structure is modeled with one level of porosity. We want to study the convection-diffusion of ions in the canalicular network. For this purpose we consider the domain Ω generated by periodically repeated "cross" geometry, i.e. geometry with three orthogonal channels, each in the direction of one axis. In other

Parameter	Value	Unit	Source
α_s	111.5	-	[19]
α_f	4.23	-	[2]
D^+	1.334×10^{-9}	$m^2 s^{-1}$	[28]
D^-	2.032×10^{-9}	$m^2 s^{-1}$	[28]
c^+	150	mol/m^3	-
c^-	250	mol/m^3	-
$\boldsymbol{w}$	$\left[0, 0, 10^{-4}\right]$	m/s	-

Table 11: Parameters of the electro-osmosis model

words, for the homogenization problem is used the same geometry, as for $\alpha-$level homogenization of the problem of poroelasticity, see Fig.8a. The geometrical parameters are also the same, so they can be found in Tab.7.

5.11 Numerical results

In this section the results of the numerical computation of the electro-osmosis problem, defined in sections above, are presented. First, we introduce the results of upscaling from the microscopic level to macroscopic, while obtaining the effective coefficients and then we use them for the macroscopic problem computation. Later, we perform the parameter study of coefficient dependence on the porosity change and also solve the problem on the microscopic scale.

5.11.1 Problem implementation

First, we implement the microscopic model for one level homogenization in the software *SfePy*. Obtained homogenized coefficient are used for the computation on the macroscopic level, which is implemented in the same software. Then, using the macroscopic solution, we can compute the problem on the microscopic scale. The numerical solutions are visualized in the parallel visualization application *ParaView Viewer* and, in part, by the module *matplotlib* in the *Python* programing language.

5.11.2 Numerical solution of microscopic problem

The geometry of RPC Y, used for describing the structure of porosities on the microscopic scale, is the same as in the Fig.8a. Note that because the macroscopic domain Ω is generated by periodic repeating of RPC Y, the used mesh must be periodical. On this geometry we compute the corrector basis function defined by Eqs.(208)-(216), which are completed by conditions. There are two types of conditions in the microscopic level.

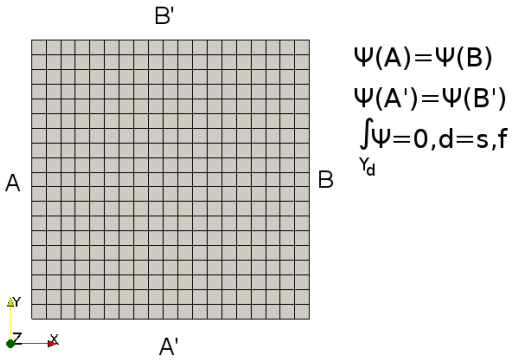

Figure 20: Boundary and integral conditions of microscopic problem, cases I and II

- First, the periodicity must be preserved, so we prescribe the periodic boundary condition. Thus, any corrector basis function Ψ has the following periodic boundary conditions

$$\Psi(A) = \Psi(B), \tag{249}$$

where A and B are the opposing faces of cubic RPC Y, see Fig.20.

- The second type of conditions are the zero conditions of the mean integral of the corrector over the domain on which it is defined: for any corrector Ψ

$$\int_{Y_d} \Psi = 0, \tag{250}$$

where $d = f, s$.

In what follows, we consider two following cases.

- **Case I:** We consider that the ion concentrations of positively and negatively charged particles differ from each other. This case approximates the bone fluid better, because we can't precisely say, that there is the same amount of anions and cations in the same time.

- **Case II:** We consider that the ion concentrations of positively and negatively charged particles are the same. We can imagine that this case refers to salt dissolved in water, where the molar concentration of Na^+ and Cl^- is the same. Note that this case is more approximative but it is better for the numerical solution of the macroscopic problem. Considering $\vartheta^{0-} = \vartheta^{0+} = \vartheta^0$ Eqs.(229) become independent on ion concentration and can be solved first in order to obtain the potentials $\varphi^0_d, d = f, s$. Than using φ^0_f we compute concentration from Eqs.(228), which are reduced to only one equation for variable ϑ^0.

  In the following text we introduce the effective coefficients computed form both cases and their comparison. For simplicity, macroscopic model will be solved only for case B.

	Case I			Case II		
A_f	4.754e-01,	2.338e-20,	2.812e-19;	4.754e-01,	2.338e-20,	2.812e-19;
$[-]$	5.146e-20,	1.385e-02,	2.569e-20;	5.146e-20,	1.385e-02,	2.569e-20;
	5.718e-20,	2.544e-20,	1.127e-01	5.718e-20,	2.544e-20,	1.127e-01
A_s	9.534e+01	1.878e-17	2.711e-17	9.534e+01,	1.878e-17,	2.711e-17;
$[-]$	4.175e-17	8.313e+01	6.510e-17	4.175e-17,	8.313e+01,	6.510e-17;
	3.094e-17	5.046e-17	8.656e+01	3.094e-17,	5.046e-17,	8.656e+01
B_m	5.709e+01,	-6.484e-16,	-4.918e-17;	2.249e+01,	-2.534e-16,	-1.419e-17;
$\left[m^2/s\right]$	1.473e-16,	1.664e+00,	-5.103e-18;	5.830e-17,	6.553e-01,	-5.666e-19;
	5.287e-17,	-2.408e-16,	1.354e+01	6.080e-18,	-9.454e-17,	5.332e+00
B_p	2.998e+01,	-3.413e-16,	-2.726e-17;	2.249e+01,	-2.534e-16,	-1.419e-17;
$\left[m^2/s\right]$	7.768e-17,	8.738e-01,	-2.330e-18;	5.830e-17,	6.553e-01,	-5.666e-19;
	2.736e-17,	-1.167e-16,	7.110e+00	6.080e-18,	-9.454e-17,	5.332e+00
C_m	1.124e-05,	5.609e-23,	7.189e-24	1.124e-05,	-1.044e-23,	-1.844e-22
$[m/s]$						
C_p	1.124e-05,	-1.044e-23,	-1.844e-22	1.124e-05,	-1.044e-23,	-1.844e-22
$[m/s]$						
D_m	2.284e-01,	1.440e-20,	-6.695e-20;	1.499e-01,	7.468e-21,	4.087e-20;
$\left[m^2/s\right]$	9.168e-21,	6.655e-03,	1.474e-20;	6.771e-21,	4.369e-03,	6.251e-21;
	-4.541e-21,	1.355e-20,	5.415e-02	2.241e-20,	4.233e-21,	3.555e-02
D_p	1.499e-01,	7.468e-21,	4.087e-20;	1.499e-01,	7.468e-21,	4.087e-20;
$\left[m^2/s\right]$	6.771e-21,	4.369e-03,	6.251e-21;	6.771e-21,	4.369e-03,	6.251e-21;
	2.241e-20,	4.233e-21,	3.555e-02	2.241e-20,	4.233e-21,	3.555e-02
S_m	1.262e-05,	0.000e+00,	0.000e+00	1.262e-05,	0.000e+00,	0.000e+00
$[m/s]$						
S_p	1.262e-05,	0.000e+00,	0.000e+00	1.262e-05,	0.000e+00,	0.000e+00
$[m/s]$						

Table 12: Comparison of effective coefficients of case I and II

5.11.3 Effective coefficients

We compute the effective coefficients by upscaling from the microscopic to the macroscopic problem. The effective coefficients are computed by substituting the correctors into Eqs.(220)-(227). For the case I, we use the input values from Tab. 11. In case II, we use the same input values as for case I, excluding anion concentration c^- and its diffusion coefficient D^-. For both of those quantities we use the same values as for cations. In Tab12 we see the resulting coefficients for both cases.

We consider that components $< 10^{-6}$ can be omitted. It is evident, that all coefficients $A_s, A_f, D_p, D_m, B_p, B_m$ have form of diagonal 3×3 matrix. The interesting fact is that coefficients S_p and S_m when omitting small components are nearly the same.

When comparing the case I and II, the coefficients $A_s, A_f, D_p, B_p, C_p, S_p$ remain the same for both cases, while D_m, B_m, have the same components as their "positive" counterpart, which is effect of using only "positive" input values.

Solution	Conditions
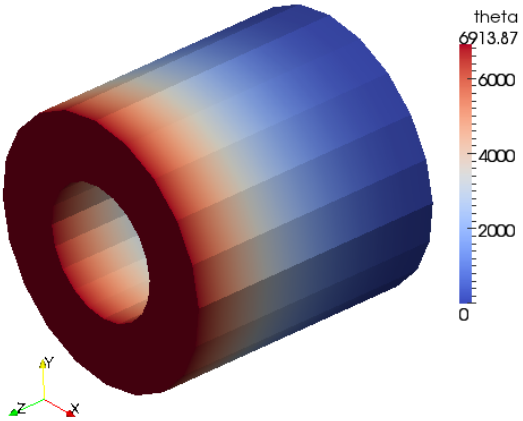 (a) Solution of ϑ^0	• $\phi_f^0(x,y,l) = \sin(\frac{t^i}{(T-3\Delta t)\pi})\ V$ for $t^i < (T-3\Delta t)$ • $\phi_s^0(x,y,0) = 300\ V$ • $\vartheta^0(x,y,0,t) = 0\ mol/m^3$ • $\vartheta^0(x,y,z,0) = 0\ mol/m^3$
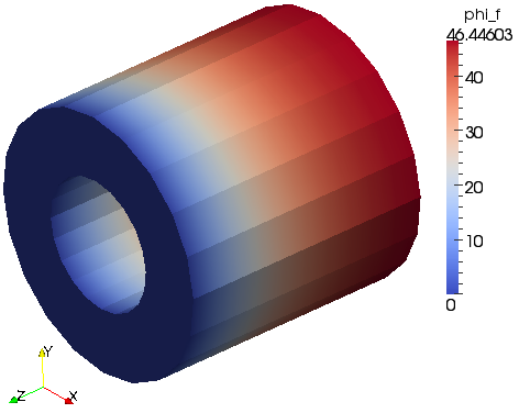 (b) Solution of ϕ_f^0	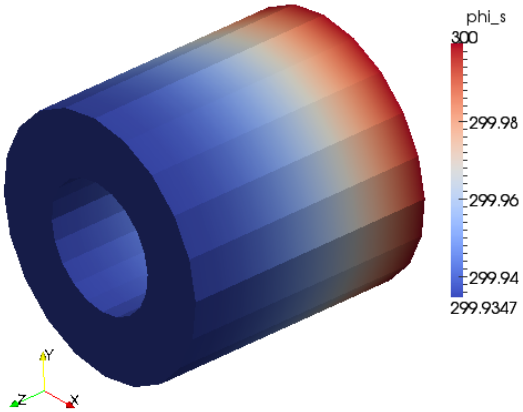 (c) Solution of ϕ_s^0

Table 13: Numeric solution of macroscopic test problem, case II

5.11.4 Numerical solutions of the macroscopic problem

In this section we introduce the numerical solution of the macroscopic problem defined by Eqs.(228) and (229). We consider the case II from the previous section. While considering $\vartheta^{0-} = \vartheta^{0+} = \vartheta^0$ Eqs.(229) become independent on ion concentration. The system transforms into two equations for computation of potentials $\varphi_d^0, d = f, s$, which can be solved first, and one equation for concentration of ion particles ϑ^0.

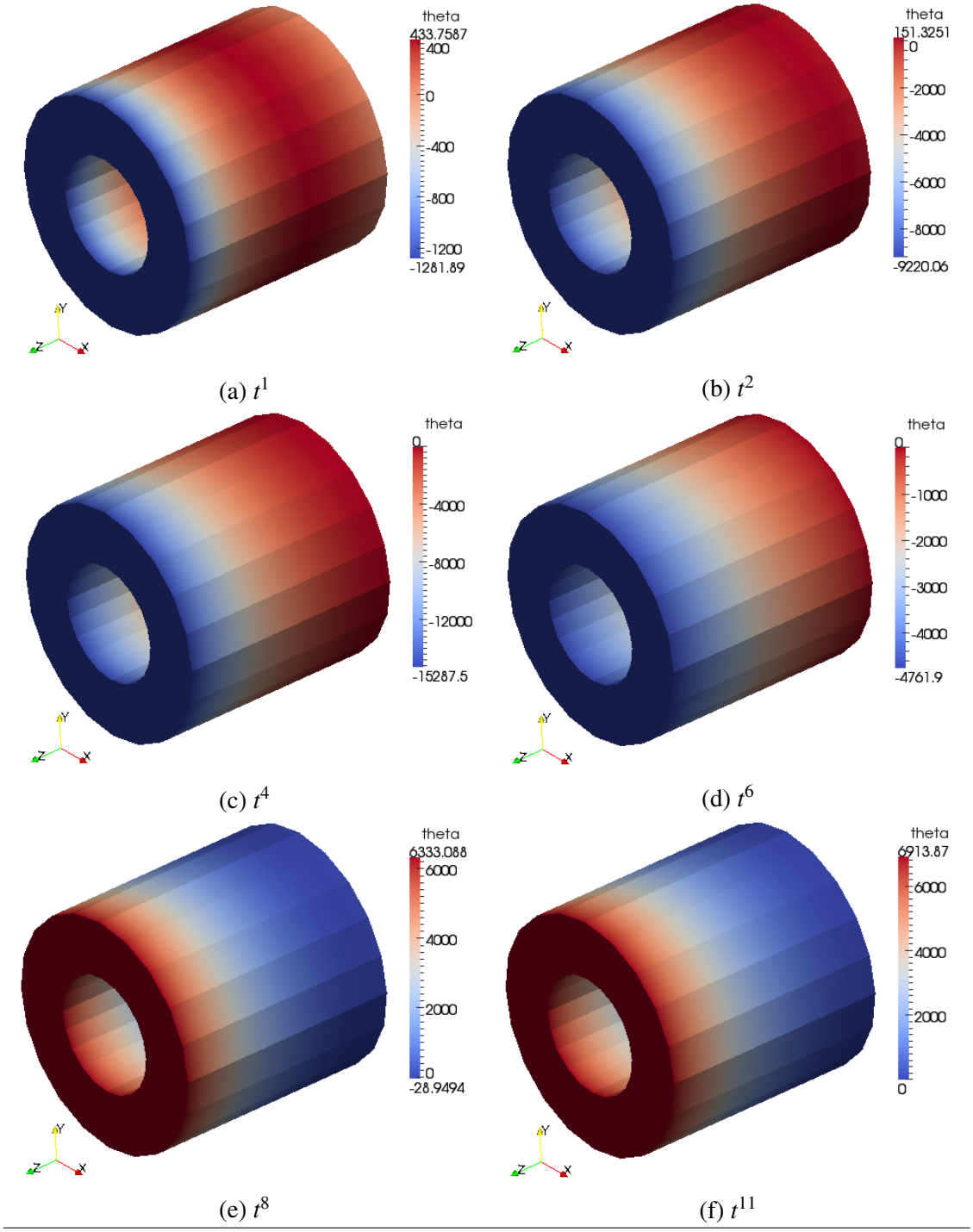

(a) t^1

(b) t^2

(c) t^4

(d) t^6

(e) t^8

(f) t^{11}

Table 14: Numeric solution of ϑ^0 in different time steps, case II

We compute the numerical solution of the macroscopic problem on a simple geometry, see Fig.9, which z-coordinate $z \in < 0, l >$. For the computation were used the effective coefficients belonging to case II solution.

Because the solution of ϑ^0 is time dependent due to time term in Eq.(229), we chose computational time T, which is discretized into n_t number of time steps. The computation starts on $t^0 = 0$ and every other time step can be computed from incremental formula $t^i = t^{i-1} + \Delta t$ where $\Delta t = T/n_t$ is a time increment. For the following numerical solution of the macroscopic problem the computational time was set to $T = 0.1$ and number of time steps $n_t = 11$.

In Tab.13 we present the solutions of the macroscopic test problem in time $t = T$. The concrete boundary and initial condition are stated by each macroscopic solution visualization.

The solution ϕ_s^0 diffuses from its boundary condition on $z = 0$ into the whole body. On the contrary, the solution ϑ^0 has the zero boundary condition on $z = 0$, but it gradually rises to its maximum in $z = l$. This is the effect of the solution ϕ_f^0 which takes part in the computation of ϑ^0. The ϕ_s^0 is mostly effected by solution ϕ_s^0 and then also by the sinus boundary condition.

The previous results were obtained in the time $t = T$. The solutions ϕ_f^0 and ϕ_s^0 are time independent, so they remain the same at all time steps. But this is not true for the concentration solution ϑ^0. In Tab.14 we show the results of ϑ^0 in time steps t^1, t^2, t^4, t^6, t^8 and $t^{11} = T$.

From the results of ϑ^0 at different time steps can be seen that the values are highly variable. But from t^8 the fluctuation in values decreases and the macroscopic solution starts to improve accuracy and finally stops in $t^{11} = T$.

5.11.5 Influence of change in porosity

For the model of poroelasticity we performed a parameter study, when we changed cross-section area of one of the canals and studied the influence on the effective coefficients. For the model of electro-osmosis we performed a similar study while using the same microscopic level geometries, see Fig.12. For illustration we introduce the visualization of ϕ_f^0 solution, where the changes are clearly visible. From figures in Tab.15 can be seen that the maximum value of ϕ_f^0, which is placed in the $z = 0$, decreases as the porosity ϕ_γ rises.

5.11.6 Recovery of the diffusion term

In the previous section we visualized the macroscopic solutions $\phi_s^0, \phi_f^0, \vartheta^0$ of the test problem. Those solutions can be substituted together with computed corrector basis functions into the relations for local variables $\phi_s^1, \phi_f^1, \vartheta^1$,Eqs.(217)-(219). Note, that Eqs.(217) transform into one equation for ϑ^1 only. Thus, we have local variables expressed by the macroscopic solutions. In what follows we focus on the recovery of diffusion velocity term from Nerst-Planc equation, which is expressed by Eq.(230). We chose two recovery elements on different sides of the macroscopic geometry, as can be seen on Fig.21. We chose one element on the left ($z = 0$) side and one on the right ($z = l$) side.

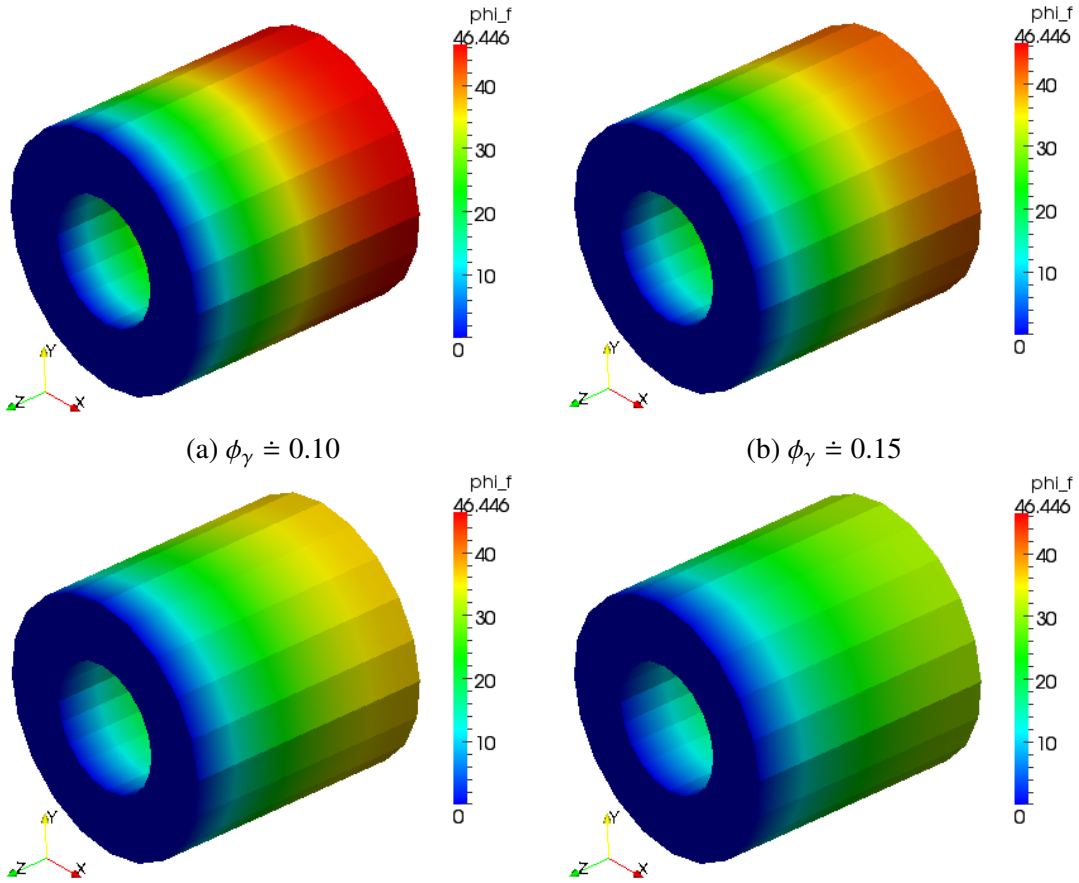

(a) $\phi_\gamma \doteq 0.10$ (b) $\phi_\gamma \doteq 0.15$

(c) $\phi_\gamma \doteq 0.25$ (d) $\phi_\gamma \doteq 0.35$

Table 15: Influence of porosity change on ϕ_f solution

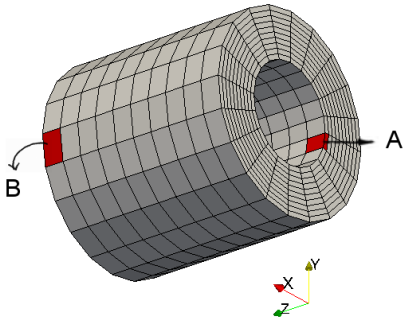

Figure 21: Recovery regions on the macroscopic body

Note, that for better visibility of both elements we have to turn the geometry so that the $z = 0$ is on

the right side on the Fig.21. To prevent confusion we denote the region in $z = 0$ by A and on $z = l$ by B. The recovery of the diffusion velocity of each region is visualized in the figures in Tabs.17.

On the Tabs.17b and 17a, we can notice that the vectors of the diffusion velocity on entrance to the intersection of canals are closing to each other. On the exit from the intersection the vectors are moving away from each other. This seems to be in contrary with general knowledge about the velocity, but don't forget that we are talking about diffusion velocity. The concentration of ions is higher in the canals in x and y direction, thus there is a stronger diffusion effect. But why is concentration of ions in those canals higher? In our model, we consider the fluid flow just in the z-direction. On the figures in Tabs.16 and 17 the z-canal is almost completely blue, with the lowest diffusion velocity. It is possible, that the fluid velocity is stronger than the diffusion and the ions are being washed away. In further research we recommend to choose a smaller fluid velocity.

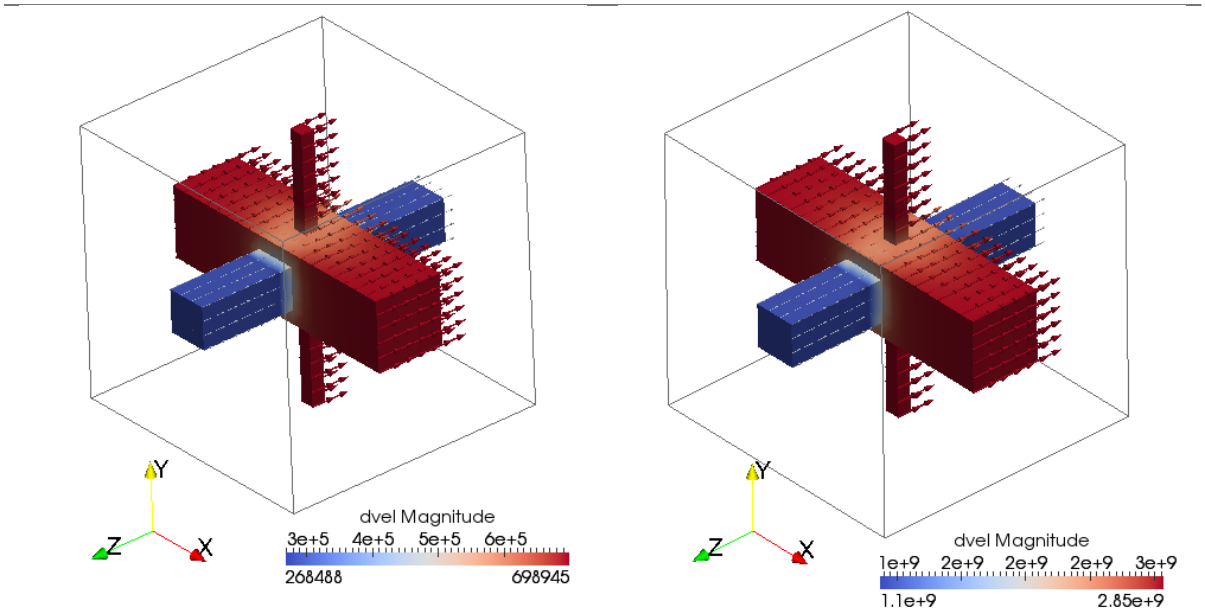

(a) The magnitude of diffusion velocity and its vector field for the recovery element A

(b) The magnitude of diffusion velocity and its vector field for the recovery element B

Table 16: Recovery of the diffusion velocity

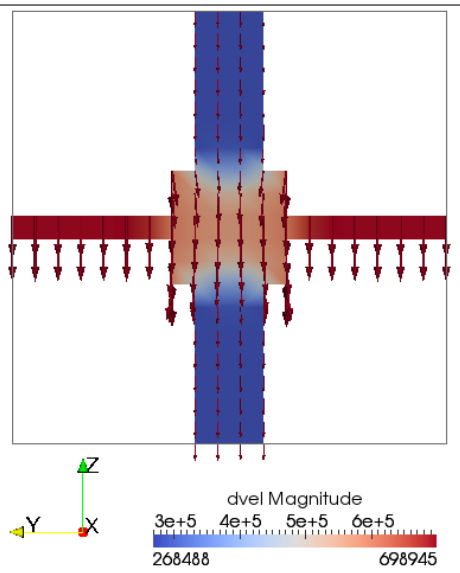

(a) Recovery element A - cross-section through YZ-plane

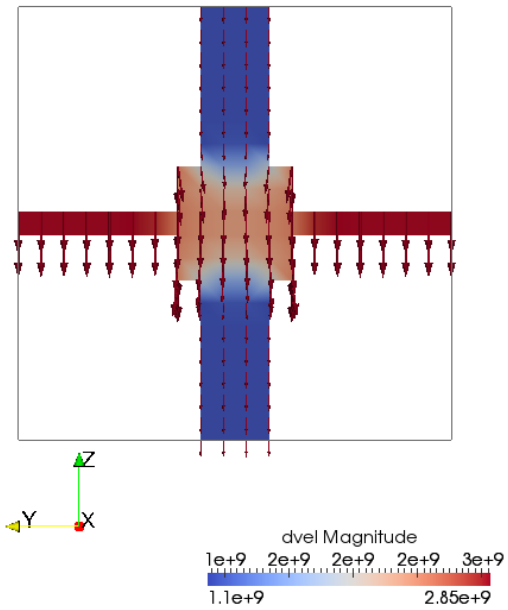

(b) Recovery element B - cross-section through YZ-plane

Table 17: Recovery of the diffusion velocity

6 Conclusion

The aim of this diploma thesis was to discuss the electromechanical coupling in the porous structure of the cortical bone tissue. To achieve this aim we introduced the mathematical model of the double-porous medium and focused on the description of pure mechanical poroelastic behavior. We explained the homogenization method and its application to the microscopic model in order to derive the homogenized model and relations for effective poroelastic coefficients. We discussed the similarity between our model and the Biot model of poroelasticity.

We computed the effective coefficients of poroelastic model and studied their dependency on the porosity change. The results of our study correspond with our assumption, i.e. we showed that with rising porosity the values of effective coefficients decrease. Further we perform the computation of the macroscopic model in FE software *SfePy*.

In the second part of this thesis we explained the origin of double-layer and main principles of electro-osmosis. In this part we also discussed the connection of electro-osmosis to the mechanical displacement, which may be realized by the piezo-electric term. Further we introduced the microscopic model of electro-osmosis in a medium with one porosity level. On this model we performed upscaling while introducing all necessary parts of the mathematical model. Finally we obtained relations for effective coefficients and then the macroscopic homogenized model. This model was also implemented in software *SfePy* for two cases; The first for different concentrations of anions and cations and the second assuming their concentrations to be the same. We introduced the numerical solution of the macroscopic problem for the case with the same concentrations. Using computed macroscopic quantities, we recovered the electro-diffusion term on the microscopic level. On the recovered regions we were able to visualize the directions and magnitudes of the diffusion in the microstructure.

The main references for the poroelasticity model were works of authors [20], [25] and [26]. As the main references for the model of electro-osmosis served works and manuscripts [10], [22] and [14]. The application of unfolding method was performed accordingly to [26].

This diploma thesis deals with a comprehensive theme and attempts to explain some main principles and problems, but we must admit, that this field of study deserves more detailed and complex insight. In a future work on a resembling theme we recommend to connect both models with piezo-electricity and the fluid velocity caused by pore deformation. It is also possible to focus on the role of bone fluid on mechano-sensing.

List of symbols

V	Volume
V_{pore}	Sum of volumes of all pores in the porous body
ϕ_i	Porosity, subscript i refers to porosity level
α	Subscript/superscript referring to microscopic porosity level
β	Subscript/superscript referring to mesoscopic porosity level
ϕ_γ	Total porosity
L	Characteristic length of RPC
$\boldsymbol{e} = (e_{ij})$	Cauchy's strain tensor
$\boldsymbol{u}(\boldsymbol{x}) = (u_i)$	Displacement tensor
$\boldsymbol{x} = (x_i)$	Coordinates in macroscopic domain
$\boldsymbol{\sigma} = \sigma_{ij}$	Stress tensor
$\mathbb{D} = D_{ijkl}$	Fourth-order stiffness tensor
μ, λ	Lamme's coefficients
δ_{ij}	Kronecker's symbol
E_i	Young's modulus
ν_{ij}	Poisson's ratio
$\mathbb{C}$	Compliance tensor
G_{ij}	Shear modulus
γ	Fluid compressibility
p	Pressure
Ω	Macroscopic domain
m	Subscript referring to matrix part of a domain
c	Subscript referring to a part of domain belonging to canals
Γ_d	Intersection between domains,$d = mc, s, f$
ε	Scale parameter
$micro$	Subscript referring to microscopic level
$macro$	Subscript referring to macroscopic level
Y	Representative periodic cell (RPC)
$\boldsymbol{y} = (y_i)$	Coordinates in RPC Y
$\hat{y}_i$	Side length of RPC Y
$\partial_{ext}Z$	Outer boundary of general domain Z
ξ_i	Macroscopic coordination of i-th RPC Y_i
$\mathbb{A} = (A_{ijkl})$	Effective stiffness tensor
$\mathcal{T}_\varepsilon(\psi(\boldsymbol{x}))$	Unfolding operator applied on the general function $\psi(\boldsymbol{x})$
∇_d	Gradient operator with respect to $d = \boldsymbol{x}, \boldsymbol{y}$
$\boldsymbol{f}$	Volume force field
$\boldsymbol{n}^d$	Normal vector of bounding domain $d = m, c, f, s$
J	Fluid volume injected from outside space
$\boldsymbol{v}$	Test function
χ_d	Characteristic function of domain $\Omega_d, d = m, c$

k_0	The macroscopic part of variable k
k_1	The fluctuation of variable k
$\mathbf{\Phi}^{ij} = (\Phi_k^{ij})$	Transformation vector
$\boldsymbol{\omega}^{ij}(\boldsymbol{y}), \boldsymbol{\omega}^{p}(\boldsymbol{y})$	Corrector basis functions
$a_y^m(\boldsymbol{w}, \boldsymbol{v})$	Bilinear form
$\hat{\mathbf{B}} = (\hat{B}_{ij})$	Effective tensor of Biot coefficients
$\hat{M}$	Effective Biot modulus of compressibility
ζ	Fluid content per unit volume increase
a_0, b_0, c_0	Semi-axes of ellipsoidal lacunae
r_x, r_y, r_z	Radius of canaliculi in x,y,z direction
$N.Ca$	Number of canaliculi per lacunae
n_i	Number of canaliculi in i-direction
PSA_{ij}	Surface of projection of lacuna into $ij-$plane
T_{PSA}	Sum of surfaces of all three planar projection of lacunae
$\hat{\phi}$	Electrical potential for in one dimension space
Φ	Electrical potential for in three dimension space
s	Superscript referring to solid part of domain
f	Superscript referring to fluid part of domain
s	Superscript referring to solid part of domain
ψ	Potential difference
z_i	Valence of ion particles of type $i = +, -$
e	Elemental charge
w_i	Electric work of ions of type $i = +, -$
Q_i	Concentration of ions of type $i = +, -$
ϵ_0	Permitivity of the void space
ϵ	Permitivity
α_d	Relative permitivity, $d = f, s$
k_b	Boltzmann constant
T	Temperature
R	Ideal gas constant
F	Farraday constant
λ_D	Debye length
N_A	Avogadro constant
$\mathbf{G} = (G_{ijk})$	Piezo-electric coupling
π	Volume electric charge density
ρ, ϱ	Surface elestric charge density
φ	Dimensionless potential
q^i	Dimensionless ion concentrations of particles of type $i = +, -$
μ^i	electro-chemical potencials of particles of type $i = +, -$

D^i	Diffusion coefficient of particles of type $i = +, -$
c^i	Molar concentration of particles of type $i = +, -$
$\Theta_z^{k\pm}, \Xi^{k\pm}, \Psi_z^k,$ Φ_f^k, Φ_s^k	Corrector basis functions of electro-osmosis model
$\mathbb{A}^{f,s} = (A_{kl}^{f,s}),$ $\mathbb{B}^{\pm} = (B_{kl}^{+,-})$ $\mathbb{D}^{\pm} = (D_{kl}^{+,-})$ $\boldsymbol{S}^{\pm} = (S_k^{+,-})$ $\boldsymbol{C}^{\pm} = (C_k^{+,-})$	Effective coefficients of electro-osmosis model
$\mathcal{M}_Z(s)$	Operator of a mean value of a variable s over domain Z

References

[1] BENO, T., YOON, Y.-J., COWIN, S. C., et al. Estimation of bone permeability using accurate microstructural measurements. *Journal of biomechanics*, 2006, vol. 39, no 13, p. 2378-2387.

[2] CARCIONE, J. M., SERIANI, G., et GEI, D. Acoustic and electromagnetic properties of soils saturated with salt water and NAPL. Journal of Applied Geophysics, 2003, vol. 52, no 4, p. 177-191.

[3] CARTER, Y., at al.: Variation in Osteocyte Lacunar Morpholigy and Density in the Human Femur - a Synchrotron Radiation Micro-CT Study. *Bone*, 2013, vol. 52, p. 126-132.

[4] CIORANESCU, D. at al.: The periodic unfolding method for perforated domains and Neumann sieve models.*J. Math. Pures Appl.* 2008, Vol. 89, pp. 248–277.

[5] CIMRMAN, R. et ROHAN, E. HIERARCHICAL MULTISCALE MODELLING OF POROUS MEDIA WITH APPLICATIONS IN BIOMECHANICS. *Engineering Mechanics*, 2012, vol. 1000, p. 18thInternational.

[6] COWIN, S. C. Bone poroelasticity. *Journal of Biomechanics*, 1999, vol. 32, no 3, p. 217-238.

[7] HAMED, E., LEE, Y., et JASIUK, I. Multiscale modeling of elastic properties of cortical bone. *Acta mechanica*, 2010, vol. 213, no 1-2, p. 131-154.

[8] HANNAH, K. M., THOMAS, C. D. L., CLEMENT, J. G., et al. Bimodal distribution of osteocyte lacunar size in the human femoral cortex as revealed by micro-CT. *Bone*, 2010, vol. 47, no 5, p. 866-871.

[9] HELLMICH, C., BARTHÉLÉMY, J.-F., et DORMIEUX, L. Mineral–collagen interactions in elasticity of bone ultrastructure–a continuum micromechanics approach. *European Journal of Mechanics-A/Solids*, 2004, vol. 23, no 5, p. 783-810.

[10] HUNTER, R. J.: Foundations of colloid science. *Oxford University Press*. 2001.

[11] KIM, J. H., OCHOA, J. A., et WHITAKER, S. Diffusion in anisotropic porous media. Transport in porous media, 1987, vol. 2, no 4, p. 327-356.

[12] MÍKA, S., PŘIKRYL, P., et BRANDNER, M. Speciální numerické metody. Vydavatelský servis, 2006, Plzeň.

[13] MORRISON, F. A.: Compressible Fluids. *Michigan Technological University*. 2004. *http://www.chem.mtu.edu/f̃morriso/cm310/compressible_flow.pdf, (22.05.2013).*

[14] MOYNE, C. et MURAD, M. A. Electro-chemo-mechanical couplings in swelling clays derived from a micro/macro-homogenization procedure. *International Journal of Solids and Structures*, 2002, vol. 39, no 25, p. 6159-6190.

[15] LEMAIRE, T., NAILI, S., et SANSALONE, V. Multiphysical modelling of fluid transport through osteo-articular media. *Anais da Academia Brasileira de Ciências*, 2010, vol. 82, no 1, p. 127-144.

[16] LEMAIRE, T., CAPIEZ-LERNOUT, E., KAISER, J., et al. A multiscale theoretical investigation of electric measurements in living bone. Bulletin of mathematical biology, 2011, vol. 73, no 11, p. 2649-2677.

[17] LI, D. Electro-viscous effects on pressure-driven liquid flow in microchannels. *Colloids and Surfaces A: Physicochemical and Engineering Aspects*, 2001, vol. 195, no 1, p. 35-57.

[18] PINHO-DA-CRUZ, J., OLIVEIRA, J. A., et TEIXEIRA-DIAS, F. Asymptotic homogenisation in linear elasticity. Part I: Mathematical formulation and finite element modelling. *Computational Materials Science*, 2009, vol. 45, no 4, p. 1073-1080.

[19] QIN, Q. H. et YE, J.-Q. Thermoelectroelastic solutions for internal bone remodeling under axial and transverse loads. International journal of solids and structures, 2004, vol. 41, no 9, p. 2447-2460.

[20] Rezek, M. Mikrostrukturálně orientovaný model perfuze v játrech . *Diploma thesis at Department of Mechanics of University of West Bohemia in Pilsen*. 2012.

[21] RHO, J. Y., KUHN-SPEARING, L., et ZIOUPOS, P. Mechanical properties and the hierarchical structure of bone. *Medical engineering & physics*, 1998, vol. 20, no 2, p. 92-102.

[22] ROHAN, E., et al. Homogenization of electro-osmosis in porous solid saturated by ionized fluid. *Raport.*

[23] ROHAN, E. Homogenization of strongly heterogeneous porous media. *Thesis of the dissertation submitted to the Czech Academy of Sciences* . 2011.

[24] ROHAN, E. et CIMRMAN, R. Multiscale FE simulation of diffusion-deformation processes in homogenized dual-porous media. Mathematics and Computers in Simulation, 2011.

[25] ROHAN, E, NAILI, S., CIMRMAN, R., et al. Hierarchical homogenization of fluid saturated porous solid with multiple porosity scales. *Comptes Rendus Mecanique*, 2012.

[26] ROHAN, E., NAILI, S., CIMRMAN, R., et al. Multiscale modeling of a fluid saturated medium with double porosity: Relevance to the compact bone. *Journal of the Mechanics and Physics of Solids*, 2012, vol. 60, no 5, p. 857-881

[27] ROHAN, E. et al. Double porosity in fluid-saturated elastic media by hierarchical homogenization . *In press*. 2012

[28] SAMSON, E., MARCHAND, J., et SNYDER, K. A. Calculation of ionic diffusion coefficients on the basis of migration test results. Materials and Structures, 2003, vol. 36, no 3, p. 156-165.

[29] SHARMA, D., CIANI, C., et al. Alterations in the osteocyte lacunar-canalicular microenvironment due to estrogen deficiency. *Bone*, 2012.

[30] TURNER, C. H., RHO, J., TAKANO, Y., et al. The elastic properties of trabecular and cortical bone tissues are similar: results from two microscopic measurement techniques. *Journal of biomechanics*, 1999, vol. 32, no 4, p. 437-441.

[31] VATSA, A., BREULS, R. G., SEMEINS, C. M., et al. *Osteocyte morphology in fibula and calvaria—Is there a role for mechanosensing?*. Bone, 2008, vol. 43, no 3, p. 452-458.

[32] YOON, Y. J. et COWIN, S. C. An estimate of anisotropic poroelastic constants of an osteon. *Biomechanics and modeling in mechanobiology*, 2008, vol. 7, no 1, p. 13-26.

[33] YOU, L. D., et al. Ultrastructure of the osteocyte process and its pericellular matrix. *The Anatomical Record Part A: Discoveries in Molecular, Cellular, and Evolutionary Biology*, 2004, vol. 278, no 2, p. 505-513.